

# **The current interruption process in vacuum**

analysis of the currents and voltages of  
current-zero measurements



# The current interruption process in vacuum

analysis of the currents and voltages of  
current-zero measurements

PROEFSCHRIFT

ter verkrijging van de graad van doctor  
aan de Technische Universiteit Delft,  
op gezag van de Rector Magnificus prof. dr. ir. J. T. Fokkema,  
voorzitter van het College voor Promoties,  
in het openbaar te verdedigen op maandag 28 januari 2008 om 10:00 uur  
door

**Ezra Petrus Antonius VAN LANEN**

elektrotechnisch ingenieur

geboren te Eindhoven

Dit proefschrift is goedgekeurd door de promotoren:

Prof. ir. L. van der Sluis

Prof. dr. ir. R.P.P. Smeets

Samenstelling promotiecommissie:

Rector Magnificus                      voorzitter

Prof. ir. L. van der Sluis              Technische Universiteit Delft, promotor

Prof. dr. ir. R.P.P. Smeets            Technische Universiteit Eindhoven, promotor

Dr. ir. M. Popov                        Technische Universiteit Delft

Prof. dr. J.J. Smit                      Technische Universiteit Delft

Dr. ir. M.D. Verweij                  Technische Universiteit Delft

Prof. dr. V. Kertész                  Budapest University of Technology

Prof. dr. S. Yanabu                    Tokyo Denki University

This work was supported by the Technology Foundation (STW) under Grant DCS.5975

Copyright © 2008 by E.P.A. van Lanen

ISBN 978-90-5335-152-9

Printing and cover design by:

Ridderprint Offset drukkerij BV, Ridderkerk, the Netherlands

Photo on cover:

© Ewerdt Hilgemann, Implosion c/o Beeldrecht Amsterdam 2007

# Summary

The circuit breaker helps protecting vulnerable equipment in a power network from hazardous short-circuit currents by isolating a fault, when it occurs. They perform this task by extinguishing a plasma arc that appears as soon as the breaker's contacts separate, and through which the short-circuit current flows. In an AC network, the current's value runs periodically through zero, and each current zero provides the breaker with an opportunity to quench the arc, because here, its energy input is temporarily zero. Due to the inductive nature of most short-circuit networks, the voltage tends to rise immediately to its maximum value after the current interruption. This complicates the current interruption process for breakers, because just after they have been loaded with the arc, they have to cope with this recovery voltage as well.

To ensure their reliability, new circuit breakers are subjected to tests with artificially generated short-circuit currents and recovery voltages, with values that are appropriate for the network in which they are intended to use. These tests follow strict rules, recorded in standards such as the IEC 62271-100, about the size and shape of the current and voltage waveforms. Specialised institutes, such as the High Power Laboratory at KEMA, perform such tests and hand out certificates to breakers that pass all tests. The certification process usually provides little more information than that the breaker passed a test, or not, and it would be beneficial for both the certification institute, and the breaker's manufacturer, to obtain more information from the tests. Such analysis on SF<sub>6</sub> breakers has already taken place with success in the past, and this work applies it to vacuum circuit breakers.

Vacuum circuit breakers are the most widely used type of breakers to protect distribution level networks, with operating voltages of up to 72.5 kV. This thesis analyses the electrical signals from short-circuit interruptions in vacuum, to detect trends and indicators on the breaker's performance. For this purpose, it describes the test circuits and the measuring techniques, used to obtain the electrical behaviour of the vacuum circuit breaker just after current zero. This includes the efforts to reduce the distortion from the strong electric and magnetic fields that inevitably involve a short-circuit test.

After its extinction, the vacuum arc leaves residual plasma behind, which provides a conducting path through which a post-arc current can flow. Since the post-arc current is the most distinctive electrical signal in a vacuum current interruption, the analysis mainly focusses on this phenomenon. The residual plasma decays within microseconds, thereby finishing the breaker's transition from a near perfect conductor to a near perfect insulator. The thesis pays special attention to the measuring equipment that was used to track these fast changes in the signals (sub-microsecond), and its large dynamic ranges (from kilo ampères to tenths of ampères, and from volts to kilo volts).

In addition to the post-arc current research, the thesis analyses the VCBs re-ignition behaviour. Since VCBs are created to prevent re-ignition, they had to be subjected to much higher currents and voltages than their rated values, to force them to reignite. These results, and the results from the post-arc current research, provide new insight in the current quenching mechanism in vacuum.

Finally, this thesis also pays attention to the interaction between the electrical circuit and the VCB after current zero. To this end, it describes how existing models are extended with theories and insights that emerged from this research. The result has been implemented as a function block in Matlab's SimPowerSystems, which facilitates the incorporation of the model in different electrical circuits.

# Samenvatting

Een vermogensschakelaar beschermt kwetsbare systemen in een elektriciteit netwerk van gevaarlijke kortsluitstromen. Dit doen zij door middel van het blussen van een plasma boog, die ontstaat zodra de contacten van de schakelaar zich van elkaar scheiden, en waardoor de kortsluitstroom loopt. In een AC netwerk gaat de stroom periodiek door nul, en dit is voor de schakelaar het geschikte moment om de boog te blussen, aangezien er dan momenteel geen energie aan de boog wordt toegevoegd. Aangezien de meeste kortsluit circuits inductief van aard zijn, nijgt de spanning direct na het doven van de boog naar zijn maximale waarde te stijgen. Dit maakt het onderbrekingsproces voor schakelaars lastiger, aangezien ze direct nadat zij belast zijn met de boog, deze wederkerende spanning moeten weerstaan.

Om hun betrouwbaarheid te garanderen worden nieuwe schakelaars uitvoerig getest met behulp van kunstmatig gegenereerde kortsluitstromen en wederkerende spanningen, die waarden en vormen hebben die overeenkomen met wat te verwachten is in het netwerk waarvoor ze gebruikt zullen worden. Deze beproevingen zijn aan strikte regels gebonden, zoals geponeerd in standaarden, zoals de IEC 62271-100. Speciale test instituten, zoals het KEMA High Power Laboratory voeren zulke beproevingen uit, en kennen certificaten toe aan een schakelaar, in het geval hij aan de vereisten voldoet. Uit het certificeringsproces volgt doorgaans niet meer informatie over de schakelaar dan dat hij aan de beproevingen voldoet of niet, en zowel het certificeringsinstituut, als de schakelaarfabrikant zouden baat hebben bij meer informatie over de test. Dergelijke analyse op SF<sub>6</sub> schakelaars heeft in het verleden al met succes plaatsgevonden, en dit werk past het toe op vacuum schakelaars.

De vacuumschakelaar is het meest gebruikte type schakelaar in distributie netwerken, met spanningsniveau's tot 72.5 kV. Dit proefschrift beschrijft de analyse van elektrische signalen van stroomonderbrekingen in vacuum, die onderzocht zijn op trends en indicatoren die betrekking hebben op het gedrag van de schakelaar. Hiertoe wordt uitgebreid stil gestaan bij de circuits en de meettechnieken die gebruikt zijn om de signalen rondom de stroomnuldoorgang te verkrijgen. Dit omvat tevens de methoden die gebruikt zijn om storing te onderdrukken die wordt opgewekt door de sterke elektrische en magnetische velden die gepaard gaan met kortsluit beproevingen.

Na het doven van de vacuumboog blijft er een plasma achter die een zekere elektrische geleiding heeft en een na-nulstroom mogelijk maakt. Aangezien de na-nulstroom het meest kenmerkende signaal van stroomonderbreking in vacuum is, wordt dit het meest onderzocht. Binnen enkele microseconden vervalt het plasma, waarna de overgang van een bijna ideale geleider naar een bijna ideale isolator volledig is. Speciale aandacht wordt er besteed aan de meet apparatuur waarmee het meten van deze snelle veranderingen (sub-microseconden), en hun grote dynamische bereik (stroomwaarden van tienden ampere tot vele tientallen kilo ampere, en spanningswaarden van enkele volts tot tientallen kilo volts) mogelijk was.

In aanvulling op het na-nulstroomonderzoek staat dit proefschrift tevens stil bij het herontstekingsgedrag in vacuum. Aangezien vacuumschakelaars ontworpen zijn om herontsteking te voorkomen, werden ze in dit onderzoek onderworpen aan stromen en spanningen die ver boven hun genormeerde waarden, om zo doorslag te forceren. Dit heeft geleid tot nieuw inzicht in het stroom onderbrekingsgedrag in vacuum

Tot slot besteedt dit proefschrift aandacht aan het modelleren van de interactie tussen het elektrische circuit, en de vacuumschakelaar na stroomnul. Als uitgangspunt hiervoor worden bestaande modellen uitgebreid met nieuwe inzichten die ontstaan zijn in de loop van dit onderzoek. Het resultaat is geïmplementeerd als een functieblok in SimPowerSystems van Matlab, wat de simulatie in verschillende elektrische circuits vergemakkelijkt.



# Contents

<b>Summary</b>	<b>i</b>
<b>Samenvatting</b>	<b>iii</b>
<b>1 Introduction</b>	<b>1</b>
1.1 The application of vacuum circuit breakers in the power grid . . . . .	1
1.2 Duties and concerns . . . . .	2
1.3 Aim of this work . . . . .	4
1.4 Outline of this thesis . . . . .	6
<b>2 The mechanism of vacuum arc extinction</b>	<b>7</b>
2.1 Introduction . . . . .	7
2.2 The vacuum arc . . . . .	7
2.2.1 Cathode spots . . . . .	9
2.2.2 Inter-electrode plasma . . . . .	10
2.2.3 Anode sheath . . . . .	11
2.3 Arc control . . . . .	12
2.3.1 Contact diameter . . . . .	12
2.3.2 Magnetic field . . . . .	13
2.3.3 Vapour shield . . . . .	13
2.4 The post-arc current and the recovery voltage . . . . .	14
2.5 Failure mechanisms . . . . .	16
2.5.1 Dielectric re-strike . . . . .	18
2.5.2 Reignition . . . . .	20
<b>3 Laboratory measurement and testing</b>	<b>23</b>
3.1 Introduction . . . . .	23
3.2 Test circuits . . . . .	23
3.2.1 KEMA short-line fault test circuit . . . . .	23
3.2.2 Synthetic test circuit . . . . .	26
3.3 Current and voltage measurements . . . . .	36

3.3.1	Current measurement with a Rogowski coil . . . . .	36
3.3.2	Voltage measurement . . . . .	39
3.3.3	Data acquisition with transient recorders . . . . .	42
3.4	Numerically processing the data . . . . .	45
3.5	Conclusions . . . . .	50
<b>4</b>	<b>Post-arc current research</b>	<b>53</b>
4.1	Introduction . . . . .	53
4.2	The arcing properties compared with post-arc properties . . . . .	54
4.3	Post-arc properties compared with each other . . . . .	65
4.4	Voltage-zero period during current commutation . . . . .	68
4.5	Conclusions . . . . .	72
<b>5</b>	<b>Reignition analysis</b>	<b>75</b>
5.1	Introduction . . . . .	75
5.2	Thermal reignitions . . . . .	76
5.3	Dielectric reignitions . . . . .	82
5.4	Continuing post-arc current . . . . .	86
5.5	Amendment 2 of the IEC standard 62271-100 . . . . .	87
5.6	Conclusions . . . . .	89
<b>6</b>	<b>Post-zero arc plasma decay modelling</b>	<b>91</b>
6.1	Introduction . . . . .	91
6.2	Residual plasma estimation . . . . .	92
6.2.1	Anode temperature . . . . .	92
6.2.2	Plasma development . . . . .	96
6.3	Black-box modelling . . . . .	98
6.3.1	Sheath model . . . . .	98
6.3.2	Langmuir probe model . . . . .	100
6.4	Alternative post-arc current models . . . . .	104
6.5	Discussion and conclusions . . . . .	106
<b>7</b>	<b>General conclusions and recommendations</b>	<b>109</b>
7.1	Conclusions . . . . .	109
7.2	Suggestions for future work . . . . .	112
<b>A</b>	<b>Eindhoven's parallel current-injection circuit</b>	<b>115</b>
<b>B</b>	<b>Eindhoven's parallel voltage-injection circuit</b>	<b>119</b>
<b>C</b>	<b>A simplified post-arc conductance model</b>	<b>123</b>
<b>D</b>	<b>Anode temperature model evaluation</b>	<b>125</b>

---

<b>E</b>	<b>Implementation of the post-arc current model</b>	<b>129</b>
<b>F</b>	<b>Sheath capacitance model</b>	<b>135</b>
	<b>Bibliography</b>	<b>137</b>
	<b>Acknowledgements</b>	<b>145</b>
	<b>Curriculum Vitae</b>	<b>147</b>



# Chapter 1

## Introduction

### 1.1 The application of vacuum circuit breakers in the power grid

Circuit breakers are devices in electrical power systems made for interrupting short-circuit currents. By isolating a fault, a circuit breaker is the last resort to prevent a calamity, such as a blackout, from happening. For a good performance of this task, they are placed at strategic locations throughout the grid. Over time, several breaker types have been developed, each of which meeting the demands of the specific circuit in which it is applied.

In the early days of electrical networks, oil and air breakers mainly performed the task of breaking a circuit. Although they performed this duty well and are still in use today, these types have significant drawbacks. A flammable extinguishing medium, such as oil, causes potential explosion hazard in the case of a failure of the breaker to interrupt a current. Air breakers, on the other hand, cause a lot of noise when breaking a current, which is a serious drawback when this equipment is placed near a residential area.

In the early 1900s, scientists discovered  $\text{SF}_6$ -gas, and its superior dielectric properties were soon recognised by the electrical industry. With circuit breakers based on  $\text{SF}_6$  gas, the size of switchgear could be reduced, while improving its reliability. Nowadays,  $\text{SF}_6$  switchgear still dominates in high-power networks.

The advantages of vacuum as a current interrupting medium were already noticed in the 1920s. However, its commercial application has been delayed until the 1950s, because the industry had been unable to create the required ultra-high vacuum and properly degassed metals. After solving these problems, the complicated manufacturing techniques were the reason why Vacuum Circuit Breakers (VCBs) were still not profitable for using them in the power grid.

VCBs continued to evolve gradually, but it was not until the 1980s, after a series of improvements, that vacuum switchgear has been applied on a large scale in electrical networks [1, 2]. Since then, the vast majority of switchgear in networks with voltages of up to 72.5 kV are based on vacuum technology, but for several reasons, it is still not profitable to produce vacuum circuit breakers for high-voltage applications, since higher voltages require larger breakers with corresponding manufacturing difficulties.

## 1.2 Duties and concerns

The main task of any circuit breaker is to conduct current under closed condition, without dissipating energy, while creating isolation in the circuit, and withstand a recovery voltage when it is open. The transition from a perfect conductor to a perfect insulator has to be fast, in order to limit the potential damage from the short-circuit current to other objects in the grid.

The basic configuration of an interrupter consists of one fixed and one movable contact. They are placed inside a bottle containing an extinguishing medium, such as oil or gas, or inside a vacuum bottle. Under normal operation, the contacts are closed, but when the command to break a current is given, an external mechanism separates them. At that point, the current flows through an electrical arc between the contacts. This arc continues to exist until its energy input is removed by external means. In an AC network, the current's value runs periodically through zero, and each current zero provides the breaker with an opportunity to quench the arc, because here, its energy input is temporarily zero. Due to the inductive nature of the grid during a short-circuit fault, a transient recovery voltage starts to rise immediately after current zero, with a peak value that can reach as much as twice the nominal voltage. The fast rising of the recovery voltage across the contact gap of a breaker puts a lot of strain on the cooling post-arc plasma, and it is the challenge of the breaker's manufacturer to prevent it from reigniting, i.e. from failing to interrupt the current.

While most types of circuit breakers contain an extinguishing medium to cool the arc, the arc of a VCB (called a *vacuum arc*) is quenched in a completely different way. The lack of an extinguishing medium prohibits external interventions of the quenching operation. Here, the arc's plasma just diffuses in the vacuum ambient after current zero.

In oil or gas type circuit breakers, the arc imposes its thermal stress mainly on its cooling medium, but a significant part of the thermal stress imposed by the vacuum arc is transmitted to its contacts. As a result, the main configuration of a vacuum interrupter distinguishes itself from other types of breakers by its large electrodes, on which this thermal stress is distributed (see Figure 1.1).

This works well for low currents, but as the current increases, the vacuum arc tends to constrict, and most of the thermal stress is focused on a large spot on the anode. This is disadvantageous for the breaker and could seriously limit its

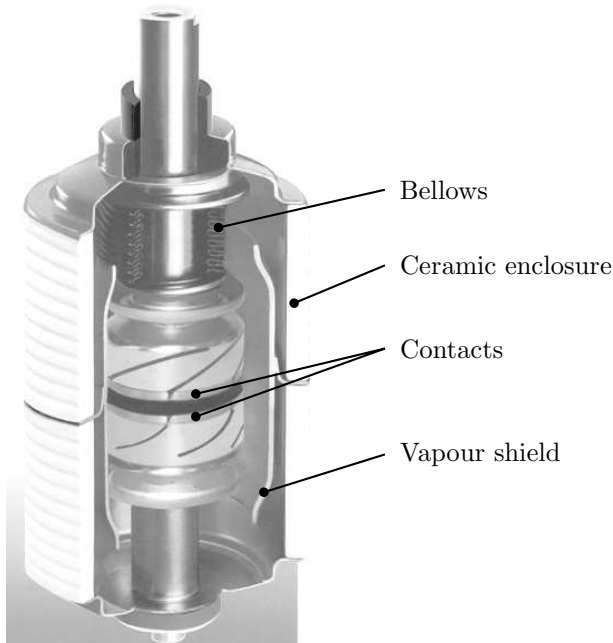


**Figure 1.1:** The inside of a vacuum interrupter.

operational lifetime. It is one of the reasons why the earlier versions of vacuum switchgear could only be applied to lower voltage applications.

Over the years, manufacturers searched for ways to increase the operating current. A major breakthrough was accomplished with the discovery that the arc can be controlled by means of magnetic fields. Since then, two types of VCBs could be distinguished, each with a differently applied type of magnetic field. One applies a magnetic field parallel to the current, which tries to oppose arc constriction, and hence, it increases the rated short-circuit current. In the other type, the current limit is increased by allowing the constriction to happen, but force it to move across the anode. In this way the thermal stress is still focussed into one point, but in time it is distributed across the contact.

Another point of concern was, and still is, the withstand voltage. Its value is more or less linearly proportional to the distance between the contacts at small gaps. However, increasing the contact distance does not automatically lead to a better performance at higher voltages. The main reason for this is that the effect of the earlier mentioned magnetic field strength drops drastically when moving away from the electrodes, and as a result, the magnetic control of the arc would suffer from such an intervention.

A great deal of investigation has been focussed on the contact material. Since the vacuum arc consists of material that arises from the contacts, the choice of contact material has a great influence on the breaker's performance. For example, a contact material with a low melting point results, in general, to a low arc voltage and low current chopping levels, contrary to refractory materials. The material also has influence on the withstand voltage capacity, and nowadays, an alloy of Cu and Cr is the most commonly used contact material.

Although nowadays, VCBs are high-tech pieces of equipment that dominate the distribution switchgear, manufacturers continue to search for simplifying the production and hence reducing their production costs.

An important part of the development of new vacuum switchgear involves testing. The physical mechanisms of the vacuum arc, and its quenching, take place on a very small temporal and spatial scale. When a commercial VCB is produced, it is sealed for life, which makes direct measurements on the vacuum arc impossible. Information about the arc is therefore only obtained from its electrical behaviour.

The verification of the current function of VCBs is extremely costly, due to the need of high-power equipment, which often has to exceed 1000 MVA of short-circuit power, installed in special high-power laboratories. In order to obtain as much information as possible on the interruption performance, degradation and operating limits of the circuit breaker from the cost-intensive tests, operators of such laboratories (both independent and those related to manufacturing industry) have a great interest in a scientific method to assess the results of tests.

### 1.3 Aim of this work

The goal of this work is to improve the understanding of current-zero measurements on short-circuit current interruption test with vacuum circuit breakers. This comprises basically three things, namely test circuits, measuring techniques and data analysis.

Testing a real circuit breaker requires a test circuit that manages both tens of kilo amperes and kilo volts. For research purposes, short-circuit tests are often performed in a 'synthetic test circuit'. Such a circuit relies on the principle that the high values for the current and voltage are required separately from each other; first a short-circuit current and then a recovery voltage. Most of the data analysed in this work has been acquired with synthetic test circuits.

The high currents and voltages entail strong magnetic and electric fields in a wide frequency spectrum, which have the potential of distorting the measurements, especially when measuring the low values of currents and voltages in the current-interruption region. Therefore, this work pays special attention to the shielding of distortion from the measurements. To this end, it compares different measuring systems.



The large collection of data gathered from the measurements is then analysed for trends and indicators that might reveal special information about the tests. The analysis focusses in particular on the events in the first microseconds after current zero, because here, the vacuum circuit breaker shows the most distinctive electrical signal, called the post-arc current. It also concentrates on measurements in which the test object failed to interrupt the current, because this information might also contribute to a better understanding of the current quenching mechanism in vacuum.

In addition to the data analysis, the breaker's interaction with the test circuit is also simulated in this work. The model developed for this purpose comprises existing models and the results from the data analysis, and its configuration is such that it can easily be adapted in different circuits.

The work has been carried out within the framework of a project from the Dutch Technology Foundation (STW), called *Digital Testing of Vacuum Circuit Breakers*. Most of the practical work has been performed at the High Currents Laboratory of the Eindhoven University of Technology, whereas the theoretical work, such as the data analysis and the model development, has been carried out at the Delft University of Technology. The project further involved the industrial participants *Eaton-Holec*, *Tavrída Electric* and *Siemens* that delivered the test objects, and the High Power Laboratory of KEMA, which provided laboratory time and measuring expertise.

## 1.4 Outline of this thesis

Chapter 2 describes the mechanisms and underlying principles concerning the current interruption in vacuum. It presents the nature of the vacuum arc and its quenching mechanisms as is currently known. Since part of the research in the next chapters is dedicated to the analysis of failure mechanism this chapter describes also the known theory on this subject.

In Chapter 3, the techniques that were used for the acquisition of measured data are described. It lists not only the different types of test circuits, but also the different measuring techniques. The combination of high currents and high voltages involves special treatment with regard to the accuracy of the measurements. For this reason, part of this chapter concerns the measures that were taken to limit the disturbance from electromagnetic interference. Finally, the chapter describes the principles behind special software that were used to recover the currents and voltages of the vacuum arc.

Chapter 4 discusses analysis that were performed on the measured data. It investigates the influence of the test settings on the post-arc current, such as changing the test-circuit, or the short-circuit current's amplitude, and it compares these results with existing results from the literature. It also searches for relationships between different post-arc current properties. One particular event that is observed frequently in the measurement due to the high resolution of the voltage measurement, is the voltage-zero period. This chapter gives examples, and searches for an explanation for this event.

Chapter 5 deals with the measurements of failures to interrupt current. According to Chapter 2, these failures can be classified into three types, which are thermal reignition, dielectric reignition and re-strikes. This chapter researches these types separately, and searches for indicators in the post-arc current that might relate post-arc current properties to the performance of the breaker. This chapter also analyses the relevance of the recently approved Amendment 2 of IEC standard 62271-100.

Chapter 6 describes the development and implementation of a post-arc current black-box model for VCBs. The experiences with other types of models, and the experience with measured data from this research are used for the model's development.

Chapter 7 collects the conclusions from this research.

## Chapter 2

# The mechanism of vacuum arc extinction

### 2.1 Introduction

The current-interruption process in a Vacuum Circuit Breaker (VCB) is done by a metal-vapour arc, which is more commonly known as a *vacuum arc* [3]. This arc appears as soon as the breaker's contacts separate, and it continues to exist until its energy input ceases. In an AC network, the current's value runs periodically through zero, and each current zero provides the breaker with an opportunity to quench the arc, because here, its energy input is temporarily zero. The breaker's resistance changes rapidly from almost zero to almost infinity, and as a result, a Transient Recovery Voltage (TRV) builds up across the breaker after current zero.

Explaining the phenomena observed in electrical measurements, and modelling a VCB's electrical behaviour, requires knowledge of the physics behind the vacuum arc's extinction. This chapter summarises the results of this research, as found in literature. It starts with describing the aspects of the vacuum arc, and the events after its extinction. After that, it describes the control of the arc, which is required to extend a breaker's technical life-time and to improve the interruption process. Finally, it explains the mechanisms that sometimes lead to a failure to withstand the recovery voltage, and reignite the vacuum arc, hence being unsuccessful to interrupt the current.

### 2.2 The vacuum arc

The vacuum arc that exists between the contacts of a VCB can generally be divided into three regions [4]. These are the *cathode spot region*, being the main source

that provides material to the vacuum arc, the *inter-electrode region*, and the *space-charge sheath* in front of the anode (see Figure 2.1). Contrary to the schematic representation of the vacuum arc in Figure 2.1a, the cathode spot region and the anode sheath region are very small in relation to the length of the inter-electrode space. These regions have typically a constant thickness of several micrometers, whereas the rest of the arc is inter-electrode plasma.

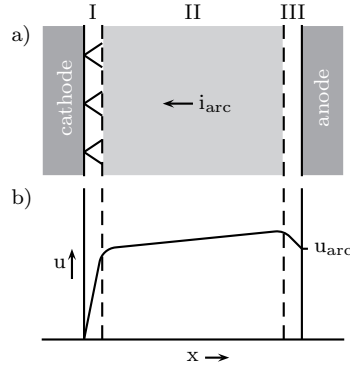


**Figure 2.1:** Schematic representation of the vacuum arc. a) Separation of the arc into separate regions: I cathode spot region, II inter-electrode plasma and III the anodic space-charge region, b) Voltage distribution across the vacuum arc.

Despite its small size, the cathode spot region covers most of the arc's voltage  $u_{arc}$  (see Figure 2.1b), and it is a typical feature of the vacuum arc that the voltage across this region remains practically constant, independent from the value of the current. This voltage depends predominantly on the type of material that is used for the breaker's contacts. For example, for copper-based contacts, which is the main component in all commercial VCBs, the voltage is about 16 V.

The slightly increasing voltage across the inter-electrode region is mainly due to Ohmic losses, but the voltage drop in front of the anode region is characteristic for the interaction between a plasma and a metal surface. It occurs not only at the anode, but it is also observed at other metal surface, such as the metal vapour shields. Therefore, instead of describing the anodic voltage drop in particular, Section 2.2.3 describes the plasma-wall interaction in general.

The vacuum arc ceases to exist when its sources, the cathode spots, have disappeared. However, it takes time for the residual plasma to disappear, and the metal vapour that is still present between the contacts after the arc's extinction. The remaining charge has still some conductance, which leads to a *post-arc current* when a TRV starts to build up across the gap. Although the actual arc has vanished, in addition to the vacuum arc properties, this section describes the post-arc current phenomena as well.

### 2.2.1 Cathode spots

Cathode spots are observed as tiny bright spots moving across the surface. The observed light arises actually from an ionisation zone in front of the cathode, see Figure 2.2. Between this ionisation zone and the cathode, an ionic space-charge sheath is present, in which electrons from the cathode are accelerated to collide with metal vapour, and ionise it. Both the distance between the spot and the cathode, as well as the diameter of the ionisation zone measure just several micrometers. Although the dimensions involved with the cathode spot region are small compared to the total vacuum arc, it takes up almost all of the arc voltage. A consequence of the small dimensions of a cathode spot is that other physical quantities, such as the current density and the electric field, are high. This turns out to be not only a consequence, but also a necessity for the spot's survival [5, 6, 7].

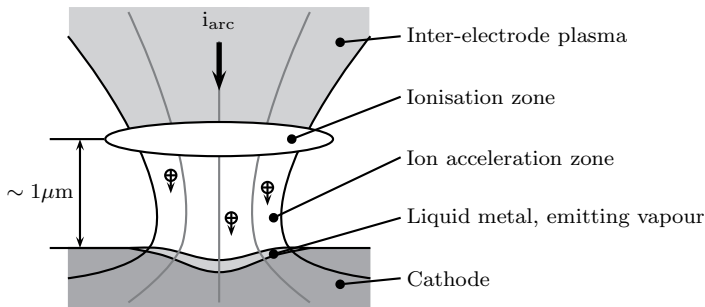


**Figure 2.2:** Schematic representation of a cathode spot.

A number of different processes control the electron emission from the cathode. First, there is *thermal emission*. When a metal is heated, an increasing amount of electrons is able to escape spontaneously from the metal's conduction band into the ambient. The current density for a metal with the temperature of a cathode spot (about 4000 K), lies in the range of  $10^7$  A/m<sup>2</sup>.

Another method for extracting electrons from a metal is by *field emission*, also known as Fowler-Nordheim tunneling. When an electric field is applied to a metal in vacuum, some electrons inside the metal are able to tunnel from their conduction band through the potential barrier in front of the cathode, into the surrounding space. According to this theory, the current density that results from the electric field near a cathode spot reaches a value of up to  $10^8$  A/m<sup>2</sup> [8].

The individual contribution of these two processes is insufficient to account for the measured cathode spot current density, with values as high as  $10^{13}$  A/m<sup>2</sup> [9]. However, when the processes are combined, the total current density is not just the sum, but a product of the separate processes. The result of this mechanism, which is appropriately called *Thermal-Field* (TF) emission, corresponds well to the measured cathode spot current density.

The rise of the surface-temperature required for TF emission under a cathode spot is mainly caused by ohmic heating by the electrical current, and by ion bombardment. The latter process is the result of ions, accelerated in the electric field inside the sheath towards the cathode. These processes generate much more heat than the metal can conduct, and hence it evaporates in an explosive way, ejecting metal vapour and droplets of liquid metal into the gap.

The surface-temperature rise at this scale can only be reached with a high current density for Joule heating, and a high electric field for the accelerations of ions inside the sheath. For a constant current and voltage, the current density and electric field are simply increased by decreasing the spatial dimensions of the cathode spot to zero. However, if the spot becomes too small in diameter, the crater produces too little vapour to ionise, and destabilises the equilibrium. This is an argument for an increasing spot size, and as a result, the cathode spot reaches a size that optimally satisfies all the requirements

Cathode spots move across the contact's surface. This movement is strongly related to the presence of surface irregularities, such as micro-protrusions or crater rims. These irregularities enhance the electric field, resulting in an improved location for TF emission. The random distribution of irregularities across the surface is the main reason for the cathode spot's erratic motion. However, when a cathode spot is subjected to a magnetic field  $\vec{B}$ , it moves in the direction of  $-(\vec{I} \times \vec{B})$ , i.e. in the opposite direction of the Lorenz force. Apparently, this force is small in relation to other processes, and although many models have been proposed in the past to explain this phenomenon (which is called *retrograde motion*), a final theory for this has not yet been found.

The retrograde motion determines the movement of multiple cathode spots with respect to each other as well. When the current increases, a cathode spot does not simply continue to increase its size, but it separates into two or more spots over which the total current is distributed. The current at which this happens depends mostly on the contact material, and for copper contacts, cathode spots have a maximum current in the range of 50-100 A.

The great number of models and theories on cathode spots that have been proposed in the past, and continue to be published nowadays, are an indication that a conclusive model has not yet been found. Finding an improved model for cathode spots is beyond the scope of this research, however basic knowledge about it might help to understand, for example, how the vacuum arc ignites, in the case of a breakdown.

### 2.2.2 Inter-electrode plasma

The majority of the ions created in the ionisation zone in front of the cathode (see Figure 2.2) return to the cathode to bombard its surface. However, a fraction of ions is launched towards the anode, thus moving in an opposite direction of the electric current. They do this with a kinetic energy that even exceeds the corresponding arc

voltage. For lower currents, their energy reaches values as high as 120 eV, while the arc voltage normally does not exceed 16 V. This effect is believed to be caused by a combination of three mechanisms [10, 11].

The first is related to a 'potential hump' in front of the cathode. The space-charge causes the potential to rise locally to a much higher value than  $u_{arc}$ , and in the resulting electric field, ions are accelerated towards the opposite direction of the electrical current.

Another force that drives ions in the opposite direction of the current is caused by a pressure gradient. The pressure near cathode spots can rise to atmospheric values, only to decrease to a low value a little further away from the cathode. The resulting pressure gradient is strong enough to force ions to move towards the anode.

The third mechanism, which is believed to deliver the greatest contribution, is electron-ion friction. In the constricted space of the ionisation zone, the kinetic energy of electrons is not only used to ionise metal vapour, but also to exchange momentum with the ions.

The density inside the inter-electrode plasma is low, which gives the charge a high mobility. Electrons cross the gap without losing much energy from colliding with ions or neutrals, and hence the plasma's conductivity is high. As a result, the electric field remains low, and ions move towards the anode without experiencing much resistance from it. In vacuum arcs of copper-based contacts, about eight percent of the electrical current consists of ion current, which is fully compensated by the electron current.

### 2.2.3 Anode sheath

Particles in a vapour move with a random velocity determined by their temperature. This creates a pressure that exhibits a force to the walls of the vapour's container. Most of the particles that collide with a metal object, such as the contacts or the vapour shield of a vacuum tube, are removed from the plasma, as they are either absorbed by the metal (electrons), or neutralised by electrons from the metal (ions). In that way, the metal acts as a sink for plasma.

Since their thermal energy is higher and their mass is lower, electrons have a higher thermal velocity than ions. Because of this, the flux of electrons at a metal boundary would be larger than the flux of ions, which results in an electrical current. An electric field in front of the electrodes repels the surplus of electrons to maintain a net charge flux of zero. This explains the electric potential difference between the plasma and the anode, which is mainly distributed across the small ionic space-charge sheath in front of the anode (see Figure 2.1).

The electric field of a singly charged particle in space stretches to infinity, but in the presence of particles with charge of opposite polarity, the spatial influence of its electric field is finite. The distance of the electric field's influence is expressed as the *Debye length*, and is slightly longer than the average distance between particles. In general, a plasma is called neutral when its size is several orders larger than its

Debye length. The neutralising effect of the space charge on the electric field also affects the size of the sheath in front of a metal object, and the anodic space-charge sheath thickness is therefore only several Debye lengths.

## 2.3 Arc control

When the arc current surpasses a certain threshold, the arc constricts towards the anode because of the electromagnetic forces. As a result, the current density at the anode's surface concentrates in a single spot, which is called the *anode spot*. The energy involved can cause this spot to melt and produce metal vapour, which in turn is partly ionised by incident electrons. At that point, the anode has changed from a passive charge collector to a new source of charge.

An anode spot differs from a cathode spot in a sense that all the current is concentrated in this single, stationary spot, and that it takes more time to cool down after arc extinction. After current zero, the former anode is bombarded by ions from the residual plasma, which are accelerated in the electric field of the TRV. The former anode becomes the new cathode, and with its increased surface temperature and an increased amount of vapour in front of it, the conditions for cathode spot formation, and hence the creation of a new vacuum arc, are severely improved. Therefore, the anode spot is not only destructive for the contacts, thereby limiting the breaker's technical life-time, but it also increases the probability of a reignition.

Eventually, the TRV causes the reignition of a VCB, but anode spots enhance the conditions for it, and they mainly determine the current interruption limit of a breaker. The most useful techniques that are used by manufacturers to increase the current interruption limit are described below.

### 2.3.1 Contact diameter

As a result of their retrograde motion, described in Section 2.2.1, cathode spots move towards the edge of the cathode, thereby maximising the area of charge production. The charge has to travel towards the centre of the anode for arc constriction. By increasing the contact's size, the distance between the cathode's edge and the anode's centre increases, and hence, arc constriction takes place at a higher current level.

Increasing the contact diameter to obtain higher rated short-circuit current ratings for VCBs is favourable. However, there are some disadvantages that limit the use of larger contacts. One of them is that it requires larger ceramic envelopes, which makes them more expensive, and another disadvantage is that larger contacts increase the probability of having a surface irregularity that enhances the electric field when a voltage is applied, which can lead to a re-strike. The latter effect is called the *surface effect*, and it is explained in more detail in Section 2.5.1.



### 2.3.2 Magnetic field

Nowadays, almost all the vacuum interrupters have a mechanism that generates a special magnetic field between their contacts. The short-circuit current itself generates this field, as the contacts are constructed in a way that the current spirals through them. Depending on the contact configuration, the current generates a magnetic field that is either parallel to the interrupter's axis (Axial Magnetic Field, or AMF [12, 13]) or radial to it (Radial Magnetic Field, or RMF [14]). Figure 2.3 depicts two examples of such contact types.

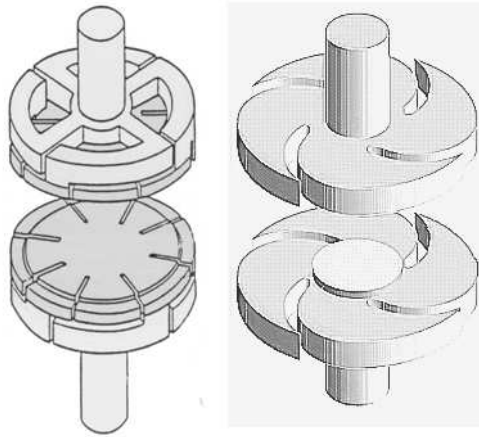


**Figure 2.3:** The contact geometry for AMF (left) and RMF (right) type interrupters.

Both types of magnetic fields are intended to relieve the thermal stress on the anode. In an AMF, the arc maintains its diffuse state at higher currents, while an RMF allows the formation of an anode spot, but forces it to rotate quickly across the anode, thereby limiting the average thermal stress on it.

In general, breakers with AMF type contacts allow for higher currents than breakers with RMF type contacts, since the absence of an anode spot results in less vapour release. However, AMF type contacts are more complicated to manufacture than RMF type contacts, which as a consequence makes their production more expensive.

### 2.3.3 Vapour shield

Vapour shields do not actually control the arc, but they increase the technical life-time of vacuum interrupters. They envelope the contacts to prevent metal vapour, released during arcing to attach to the ceramic envelope. In this way, it prevents the formation of a conducting path along the inner side of the ceramic enclosure that

eventually may short out the breaker, which would render the interrupting device useless.

As explained in Section 2.2.3, the metal vapour shield acts also as a sink for charge. As a result, the shield's configuration has an influence on the breaker's electrical behaviour. This is most clearly seen in the post-arc current. Shields with a small diameter allow less charge to be present, and drain it more quickly than shields with a larger diameter. As a result, the post-arc current's magnitude and duration are proportional to the shield's diameter [15, 16]. Therefore, it is beneficial for the breaker's recovery to have shields with a small diameter, but a minimum value is also required to prevent a breakdown via the shield.

Shields are also applied to protect other vulnerable parts of the breaker, such as the metal bellows, but their influence on the breaker's electrical behaviour is negligible.

## 2.4 The post-arc current and the recovery voltage

When the arc current approaches zero, the number of cathode spots reduces until only one is left. This spot continues to supply charge to the plasma, until finally, the current reaches zero. At current zero, the inter-electrode space still contains a certain amount of conductive charge. As the current reverses polarity, the old anode becomes the new cathode, but in the absence of cathode spots, the overall breaker's conductance has dropped, which allows the rise of a TRV across the VCB.

The combination of the residual plasma's conductance and the TRV gives rise to a *post-arc current*, which, depending on the arcing conditions and on the TRV, can reach a peak value of several milli amperes to several tens of amperes. The post-arc current has been subject to investigation for many years, since it is one of the most distinctive electrical features of short-circuit current interruption with VCBs [14, 17, 18, 19, 20, 21]. Because the post-arc current shows a clear dependence on the arcing conditions, it is a reasonable assumption that it reflects the conditions inside the breaker immediately after current zero. This would provide researchers with a tool to investigate the interruption performance without having to damage the VCB to look inside. However, the post-arc current unfortunately contains a considerable scatter that disturbs the relationship between the arcing conditions and the post-arc current. This has to do with the final position of the last cathode spot which, till now, can only be determined by looking inside the breaker.

When the final position of the last cathode spot is near the edge of the cathode, a significant amount of charge is ejected away from the contacts, and disappears, e.g. by recombination at the breaker's vapour shield. If this is the case, less charge is returned to the external electrical circuit by means of a post-arc current, compared to the situation in which the final cathode spot's position is close to the centre of the cathode (see Figure 2.4). Since a cathode spot moves randomly across the cathode surface (but is biased by an external magnetic field), its final position is unknown.

As a result, the post-arc plasma conditions are different for each measurement, which gives the post-arc current its random nature.

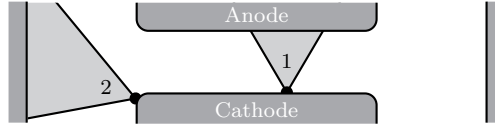


**Figure 2.4:** If the final cathode spot extinguishes at position 1, more charge returns to the electric circuit than when it extinguishes at position 2.

Nevertheless, some general conclusions about the shape and intensity of the post-arc current can be drawn. For instance, that its peak value and duration increase with an increasing value of the short-circuit current and with an increasing arcing time.

With regard to its mechanism, the generally accepted theory divides the post-arc current into three phases, which are described below.

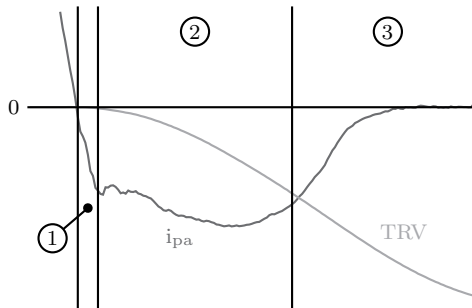


**Figure 2.5:** The post-arc current in a VCB. The numbers refer to the phases that are explained in the text.

During arcing (before current zero), ions are launched from the cathode towards the anode. At current zero, the ions that have just been produced continue to move towards the anode as a result of their inertia. Electrons are much lighter than ions, and it can be readily assumed that they adapt their speed immediately to a change of the electric field. As a result, the electrons match their velocity with the ion velocity to compensate for the ion current, and this makes the total electrical current zero.

We now enter phase 1. Immediately after current zero, the electrons reduce their velocity, and a net flux of positive charge arrives at the post-arc cathode. This process continues until the electrons reverse their direction, and until this moment, the net charge inside the gap is zero. With no charge and a high conductivity of the neutral plasma, the voltage across the gap remains zero in this phase.

As soon as the electrons reverse their direction, the post-arc current enters its

second phase. In this phase, the electrons move away from the cathode, leaving an ionic space charge *sheath* behind, see Figure 2.6. Now, the gap between the electrodes is not neutral any more, and the circuit forces a TRV across it. This potential difference stands almost completely across the sheath, which, contrary to the plasma, is not (charge) neutral.

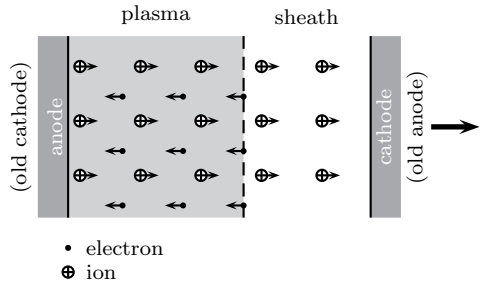


**Figure 2.6:** Schematic representation of the post-arc sheath growth.

Initially, the plasma connects the vapour shield surrounding the contacts electrically to the cathode, as in Figure 2.7a [19, 22]. As a result, the distribution of the electric field in the sheath does not change much as the sheath continues to grow, since the vapour shield maintains the cathode's potential, see Figure 2.7b. However, after a while, the metal vapour shield becomes disconnected from the electrical circuit as the sheath progresses towards the anode (see Figure 2.7c). This process changes the electrical configuration of the vacuum chamber drastically, and it is frequently observed that at this moment, the post-arc current shows a distinctive drop towards zero. Measurements performed by others on the vapour shield's potential in the post-arc phase confirm this theory [23].

The sheath continues to expand into the inter-electrode gap until it reaches the new anode. At that moment, the post-arc current reaches its third phase. The electrical current drops, since all electrons have been removed from the gap. The electric field between the contacts moves the remaining ions towards the cathode, but the current that results from this process is negligible.

## 2.5 Failure mechanisms

A failure occurs when a breaker is unable to withstand a voltage after current interruption, and a new arc is formed, through which the short-circuit current continues to flow. Knowing the nature of a failure makes it easier for developers to prevent it from happening, and nowadays, commercially available VCB's are well capable of reliably interrupting currents according to their current and voltage rating.

If nevertheless the breaker does not interrupt the current at the first current zero

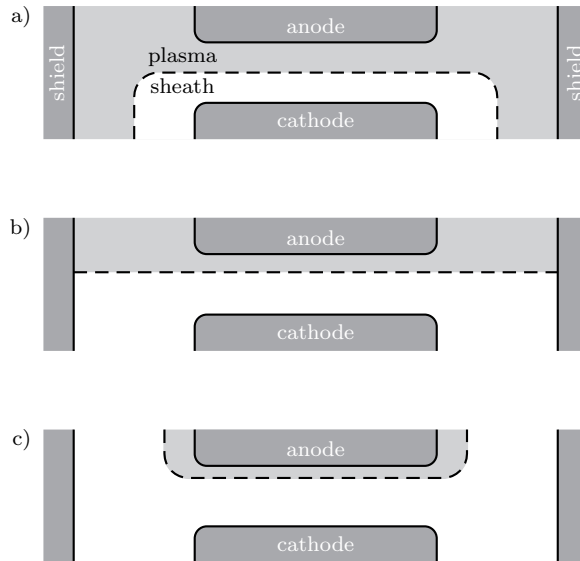


**Figure 2.7:** The sheath growth eventually isolates the metal vapour shield.

after contact separation, it most likely interrupts the current at the next current zero. The reason for this is that the conditions for a successful current interruption at the following current zero have improved. Although it is difficult to investigate the conditions in an hermetically sealed breaker, two examples can be given that make this assumption probable.

The first has to do with the arcing time. The average contact separation speed of a VCB is about 1 m/s. This means that when the contacts start to separate just an instant before the first current zero, the contacts have not reached their maximum separation at current zero. Since the breakdown voltage increases proportionally with the contact separation, a breakdown at a voltage below the breaker's rated voltage can occur. In the next current loop, the contacts continue to separate to reach its maximum at the following current zero and interrupt the current correctly.

Another example has to do with the electrical properties of the external circuit. A short-circuit network has a dominant inductive nature. That means that when the short-circuit occurs at an instant other than the instant of a maximum voltage, a DC component adds to the short-circuit current. This DC component decays due to resistive elements in the circuit, and as a result, the short-circuit current can be divided in successive major and minor loops (see Figure 2.8). The breaker's current-interruption conditions after a major loop are worse than after a minor loop. Hence, it is likely that if a breaker fails to interrupt the current after a major loop, it can

still break the current at the next current zero, after the minor loop.

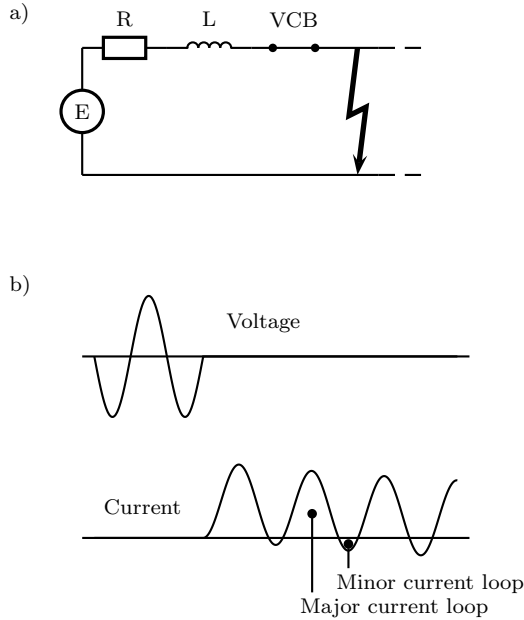


**Figure 2.8:** Example of an asymmetric short-circuit current. a) the inductive circuit and b) the voltage and current trace of the VCB.

In general, events of continuation of arcing after initially successful interruption are divided into two different types, depending on the time after current zero at which they occur. One is called *dielectric breakdown*, which happens some time after current zero, and the other is called *thermal breakdown*, which is the breakdown type that occurs almost immediately after current zero, when residual charge and vapour are still present in abundance between the contacts [24, 25].

### 2.5.1 Dielectric re-strike

Section 2.2.1 introduced the principle of Fowler Nordheim tunneling, which is the mechanism that draws electrons from a metal surface by means of an electric field. The resulting current density causes locally Joule heating of a contact, increasing its temperature locally, which may eventually lead to the formation of a cathode spot, and subsequently to a re-strike. Since such a failure is initiated by an electric field, it is called (*dielectric*) *re-strike*. This term is used for describing the failure a VCB, at an instant when the presence of residual vapour from a vacuum arc is unlikely. Such a failure occurs, for example, several milliseconds after current zero.

For perfectly smooth contact surfaces, the electric field in a VCB under normal operating conditions is generally too low to cause dielectric re-strike. However, irregularities are widely present on the contact surface, which locally enhance the electric field (see Figure 2.9a). This concentrates the current density to smaller surface areas, which increases the ohmic heating locally, and thus creates the conditions for a re-strike.

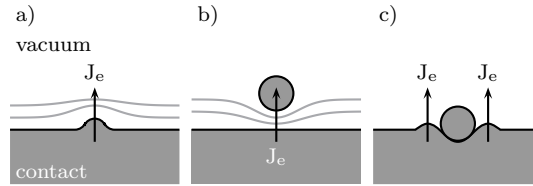


**Figure 2.9:** Examples of mechanisms that enhance the electric field at the contact surface, and amplify the field emission by: a) microprotrusions, b) micro particles moving across the contact surface and c) transfer of kinetic energy to charge release from the impact of charged micro particles on the contact.

Each time that a protrusion melts due to Joule heating, surface tensions of the liquid metal smooths this protrusion out, thereby improving the contact's dielectric property. Because of the great number of microscopic protrusions on new contacts, a VCB initially starts with a lower breakdown voltage, which increases to an asymptotic maximum value after a series of re-ignitions, because with each breakdown, one or more protrusions are removed. Manufacturers make use of this principle, and increase a VCB's breakdown strength by applying an AC low-current arc for some time to new VCB's. This technique is known as *surface conditioning*.

The re-strike is not only enhanced by irregularities on the contact's surface, but also by microscopic particles in the vacuum [26, 27]. Although manufacturers spend much effort on cleaning the interior of a VCB, the presence of these particles is inevitable. They originate, for example, from protrusions on the contact surface, which are drawn from it under the influence of an electric field, but they can also be left-overs from a vacuum arc, which are not properly fused to the contacts or the shield after the arc's extinction.

There are several ways how a micro particle can contribute to a re-strike. For example, when in the vicinity of a contact, it enhances the electric field as indicated in Figure 2.9b, which may lead to a similar current-density concentration as described earlier for a surface irregularity. Another way is that the incident electron current on the particle increases its temperature, and eventually vaporises it, causing an improved scenario for a re-strike.

If a particle is charged, it accelerates in the electric field and collides with a contact. The transfer of kinetic energy can cause the release of vapour, or even charge. With the surface deformation from the impact, new protrusions are formed that enhance the electric field (see Figure 2.9c). All these mechanisms contribute to

a higher probability for a re-strike.

Field emission of electrons, the release of vapour and charge and other processes are enhanced when the temperature of the contacts increases. After current zero, the residual charge and vapour decays within microseconds and milliseconds, respectively, but cooling of the contacts takes a considerable longer time. Especially in the case that an anode spot has been active during arcing, a pool of liquid metal on the (former) anode is likely to remain present for a considerable time after current zero, and it thereby enhances the conditions for a dielectric re-strike.

### 2.5.2 Reignition

A *thermal* reignition occurs when a VCB fails in the period immediately following current zero. This term is originally used for gas circuit breakers, where the probability of having a breakdown depends on the balance between forced cooling and Joule heating of the residual charge in the hot gas between the contacts. This process differs strongly from thermal reignition in vacuum, where charge and vapour densities are much lower than in gas breakers.

As described before, immediately after current zero, the gap contains charge and vapour from the arc, and the contacts are still hot, and can also have pools of hot liquid metal on their surface. It takes several microseconds for the charge to remove (by diffusion and by the post-arc current), but it takes several milliseconds for the vapour to diffuse, and the pools to cool down [25, 28]. When a failure occurs when vapour is still present, but charge has already decayed, this is called *dielectric* reignition. With the increased contact temperature, the conditions for a failure of the type as described in Section 2.5.1 are improved, but the increased pressure might also cause another process, called *Townsend breakdown* [29, 30, 31].

When an electron, accelerated in the electric field, hits a neutral vapour particle with sufficient momentum, it knocks out an electron from the neutral. This process reduces the kinetic energy of the first electron, but from here, both electrons accelerate in the electric field, hit other neutral particles and cause an avalanche of electrons in the gap, which eventually causes reignition.

This process of charge multiplication enhances when the probability of an electron hitting a vapour particle increases. This can be achieved by either increasing the vapour pressure, or by increasing the gap length. Both methods reduce the reignition voltage, but at some point, electrons collide with particles before reaching the appropriate ionisation energy. As a result, after reaching a minimum value, the reignition voltage eventually rises with increasing vapour pressure or gap length. Figure 2.10 depicts the relation between the vapour pressure and the breakdown voltage at constant gap length. Such a graph is called a *Paschen Curve*.

The Townsend breakdown theory is based on a stationary vapour, in which the electric field is more or less equally distributed. This differs strongly with the situation between VCB contacts immediately after current zero. Here, the charge distribution is definitely not equal, and in some regions of the gap, ions still have a con-



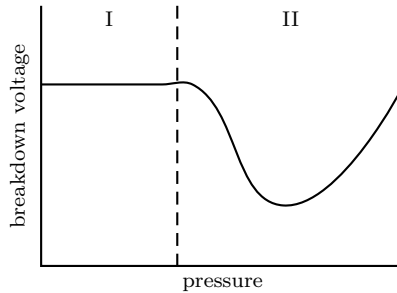


**Figure 2.10:** Illustration of the Paschen curve for an arbitrary gas at a fixed gap length. I Pressure independent dielectric reignition region, II Townsend reignition region.

siderable drift velocity. This makes the determination whether or not the observed reignition of the VCB resulted from Townsend breakdown particularly difficult.

In addition to Townsend breakdown, the increased anode temperature improves the conditions for extracting electrons from it. Moreover, the TRV not only extracts electrons from the anode, it also launches ions towards it, a process which further increases the anode's temperature [32]. This might eventually lead to a failure that is similar to dielectric re-strike, but since it occurs during the post-arc current, it is still called thermal reignition.



## Chapter 3

# Laboratory measurement and testing

### 3.1 Introduction

In an electrical test of vacuum circuit breakers, the post-arc current is the most informative component of the measurement. However, accurately measuring the post-arc current in vacuum circuit breakers requires special measuring techniques. The measuring equipment has to measure the small values of currents and voltages in the current-zero period, while coping with the high arcing current and the high recovery voltage. Besides the need for a wide dynamical range, the measuring equipment also has to be shielded from effects that disturb the results, such as the strong magnetic fields that occur during the high-current phase [33, 34].

This chapter describes the techniques that were used to accurately recover the electrical processes of the vacuum arc near current zero. Appropriate application of equipment reduced most of the disturbing influences, but the inevitable distortion from stray components nearest to the breaker is reduced with special software.

### 3.2 Test circuits

#### 3.2.1 KEMA short-line fault test circuit

A short-circuit that occurs on an overhead line some distance from the breaker terminals (see Figure 3.1), causes electromagnetic waves to travel between the fault and the terminals. This results in a particularly steep rise of the Transient Recovery Voltage (TRV) across the breaker, immediately following current zero. As a result, the (cooling) medium between the breaker's contact experiences an increased amount of strain. In fact, the Short Line Fault (SLF) is considered to be one of the most severe

fault for breakers to interrupt, and therefore, analysing the breaker's arc quenching behaviour under SLF conditions is favourable.

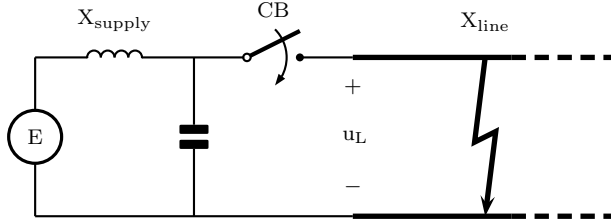


**Figure 3.1:** Typical short-line fault situation.

As the name already suggests, the length of the line in an SLF determines the magnitude of the short-circuit current. It affects the type of interruption in several ways [35, 36]. First, the line inductance  $L_{line}$  increases with increasing line length. As a result, longer lines reduce the short-circuit current, since it depends linearly on the inductance, and hence, the breaker's extinguishing medium experiences less strain from it (see Figure 3.2). The line length is normally expressed as a percentage, which indicates the reduction of the short-circuit current, compared to when a line is absent. For example, a 90% SLF indicates that the line reduces the maximum short-circuit current with 10 percent. The percentage of short-line fault can therefore easily be calculated with

$$SLF \text{ percentage} = \frac{X_{supply}}{X_{supply} + X_{line}}, \quad (3.1)$$

where  $X_{supply}$  and  $X_{line}$  are the impedances of the supply and the line, respectively (see Figure 3.1).

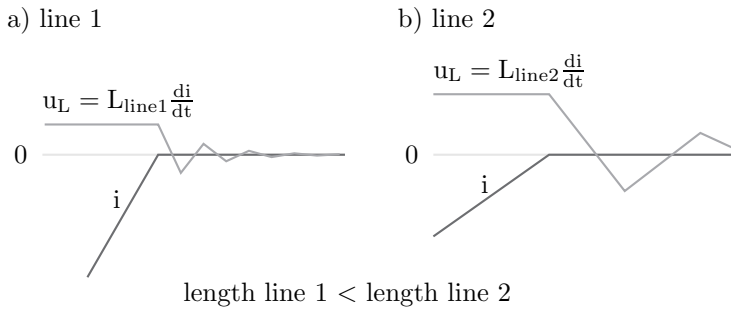


**Figure 3.2:** The effect of the line length on the short-circuit current and the line-TRV.

The line length also influences the behaviour of the travelling waves. It takes more time for electromagnetic waves to travel on a long line than on a short one,

thereby boosting the initial TRV to higher levels and thus increasing the strain on the breaker. On the other hand, longer lines reduce the short-circuit current, and hence, the breaker experiences less strain during the arcing period.

These opposite working effects implicate that breakers experience a maximum strain for a specific line length. The short-circuit current on an extremely long line would be close to zero, whereas the line TRV would be absent in the case of zero line length. It has been analysed that for  $\text{SF}_6$  circuit breakers, the critical line length is around 93 percent, while for air blast breakers, this is between 75 and 85 percent. The critical line length for VCB's has not been determined yet, possibly because so far, the ability of breakers to break an SLF is only tested on breakers with voltage ratings of 52 kV and above [37]. In 2006, the IEC agreed upon Amendment 2 to standard IEC 62271-100 [38], which states that breakers with voltage ratings of 15.5 kV and above should also be subjected to SLF tests.

At the source side of the breaker, which is the circuit on the left side of the circuit breaker in Figure 3.2, the trapped magnetic energy in the source circuit's inductance generates an additional component of the TRV. Although this component has a lower frequency than the lowest harmonic of the line TRV, its amplitude can reach twice the system's peak voltage. Figure 3.3 shows the simulation of an SLF TRV across the breaker.

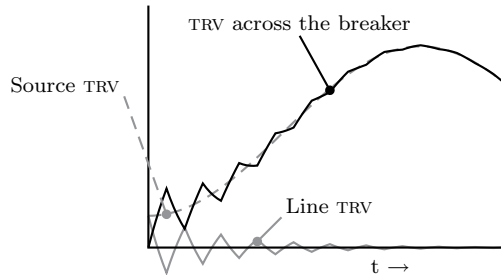


**Figure 3.3:** TRV resulting from the difference between the line-TRV and the source-side TRV.

It is not practical to use a real overhead line for short-circuit test purposes, because this entails rather voluminous and expensive equipment. For this reason, test facilities, such as KEMA's High Power Laboratory, use artificial lines as an alternative, constructed with lumped elements.

Figure 3.4 depicts a simplified version of the SLF simulation circuit used by KEMA [39, 40]. An elaborate version of it is described in [36]. The inductance  $L$  reduces the short-circuit current, whereas  $R$  ensures the desired initial TRV slope. For this purpose, its value is taken equal to the line's surge impedance (normally 450  $\Omega$ ). The values for the components  $C$  and  $L_r$  are such, that the ratio between the voltage induced by the line ( $u_L$ , see Figure 3.2), and the first peak of the line TRV remains fixed. The capacitance  $C_{dL}$  is an optional component, used to delay the start

of the line TRV with a certain time. Such a delay facilitates the current-interruption, because it allows the gap to recover before the TRV starts to rise.

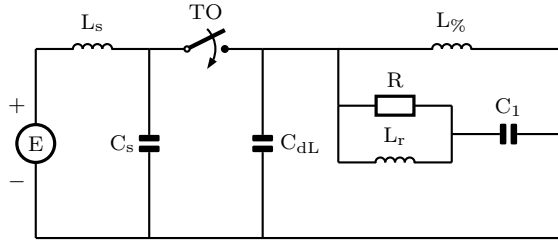


**Figure 3.4:** Simplified scheme of KEMA's SLF simulation circuit.

Figure 3.5 shows the results of experiments with different line lengths on a VCB. It demonstrates the influence of the TRV on the post-arc current. Chapter 4 further discusses these results.

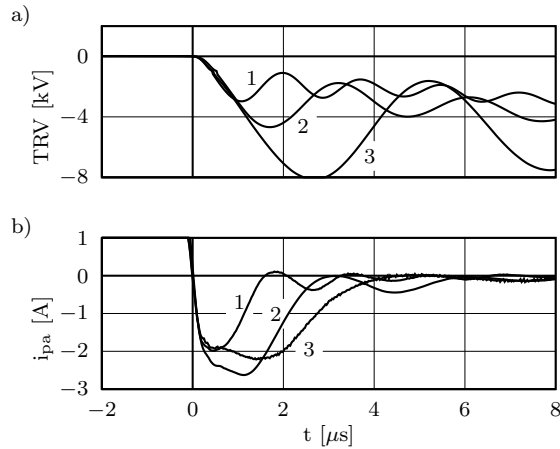


**Figure 3.5:** Results from three different measurements, performed under the same conditions (same arcing time and current, and same rate of rise of recovery voltage), but with different line parameters. 1:  $L_{\%} = 105 \mu\text{H}$ , 2:  $L_{\%} = 225 \mu\text{H}$  and 3:  $L_{\%} = 453 \mu\text{H}$  [40].

### 3.2.2 Synthetic test circuit

The simulation of a short-circuit involves currents of several tens of kilo amperes, and voltages of several tens of kilo volts. Most laboratories do not have a generator capable of generating these currents and voltages, but because the high current and the high voltage appear separately, the short-circuit interruption simulation is often

performed in a *synthetic circuit* [41]. Such a circuit consists of two separate circuits, one that generates the short-circuit current, and another that supplies the TRV.

### *Parallel current-injection circuit*

There are different types of synthetic circuits, and Figure 3.6 depicts the simplified parallel current-injection, or Weil-Dobke circuit that was used for this research in the High Current Laboratory at the Eindhoven University of Technology [42].

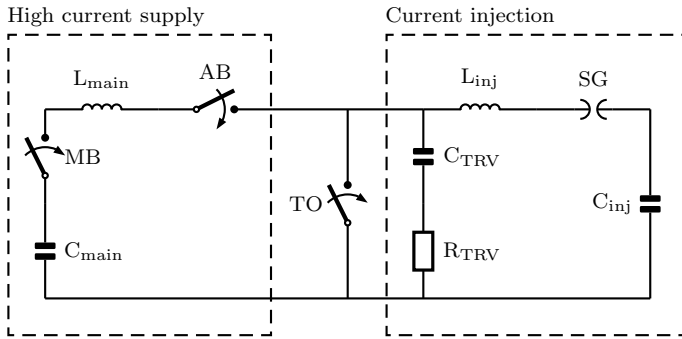


**Figure 3.6:** Synthetic test circuit used at the Eindhoven University of Technology.

Before the start of an interruption test, the Test Object (TO) and the Auxiliary Breaker (AB) are both closed, while the Master Breaker (MB) is open, and the capacitor banks  $C_{main}$  and  $C_{inj}$  are charged to a pre-determined voltage level. Operating the breakers and the spark-gap in the appropriate sequence results in the reproduction of one half loop of short-circuit current. If the TO opens its contacts, it interrupts the short-circuit current at current zero, and the circuit immediately generates a TRV across it. Figure 3.7 shows the order of the described events.

The AB separates the current injection circuit from the voltage-injection circuit. It is usually the same type of breaker as the TO, and hence it can also re-ignite. However, it is more likely that the TO re-ignites earlier than the AB, because the current zero in the AB takes place a few moments before the TRV starts to rise. This gives the AB a better opportunity to recover from the arc than the TO, and this practically eliminates the risk that the AB fails.

For a correct simulation, the time derivative of the current  $di/dt$  through the TO at current zero should be equal to the situation in a real short-circuit in the system. This is arranged by presetting the values of the components  $L_{inj}$  and  $C_{inj}$ , and the charge voltage of  $C_{inj}$ . Furthermore,  $L_{inj}$  and the TRV components (in this case  $C_{TRV}$  and  $R_{TRV}$ ), determine the shape of the TRV (see Figure 3.6).

Appendix A describes the Eindhoven circuit in more detail. It has been designed to generate short-circuit currents of approximately 50 Hz. The purpose of

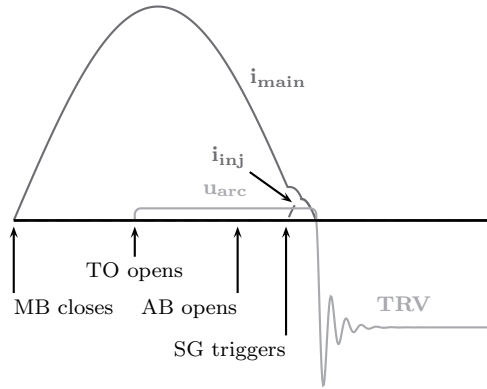


**Figure 3.7:** Sequence of events that invoke the simulation of a short-circuit current interruption with the Weil-Dobke circuit. The displayed currents and voltages apply to the TO.

the transformer in this circuit is twofold. It increases the short-circuit current at its secondary side, and it serves as the inductance for the  $LC$  resonance circuit. With the fixed, and known value for the transformer inductance, which is considered to be short-circuited at its secondary side, the capacitor bank has been designed such that the  $LC$  circuit meets the required resonance frequency of about 50 Hz [43]. The theoretical peak value of short-circuit current is 100 kA, but in practice, it does not exceed 50 kA, because the circuit has losses, and also the non-zero impedance at the transformer's secondary side plays a role.

The current-injection circuit is designed to generate a short-circuit current with a frequency of about 500 Hz. With its frequency ten times higher than the main current's frequency, the injection current's peak value has to be only one tenth that of the main current's peak value to obtain the correct  $di/dt$  at current zero. When properly tuned, the spark-gap triggers the voltage-injection current 0.5 ms before the main current reaches zero, and the current from the voltage-injection circuit continues to flow until it reaches its own current zero, which is 0.5 ms after the main current has been interrupted. This process reverses the voltage across  $C_{inj}$ , which allows the generation of a negative TRV immediately after current zero.

Following the TO's current zero, the breaker quickly changes from a nearly perfect conductor to a nearly perfect isolator. During this transition,  $C_{inj}$  releases its energy across the TRV branch. The value of  $C_{TRV}$  is several orders of magnitude smaller than the value of  $C_{inj}$ , and therefore, the shape of the TRV is mainly determined by  $L_{inj}$  and the components of the TRV branch. In the Eindhoven circuit,  $L_{inj}$  is constructed with three reactors, specially designed for use in a test laboratory (see Figure A.4. Each coil has a number of windings, each of which can carry a current of up to 500 A. The total current capacity can be increased by connecting the coils in



parallel, whereas its total inductance is increased by connecting the coils in series. A combination of this results in the desired current capacity and inductance. In spite of the relative ease with which the value  $L_{inj}$  can be changed, the TRV parameters were in general only altered with  $C_{TRV}$  and  $R_{TRV}$ , to maintain the short-circuit current's time-derivative requirements at current zero. Figure 3.8 shows the results of three different measurements, performed with different TRV's. Chapter 4 discusses the results.

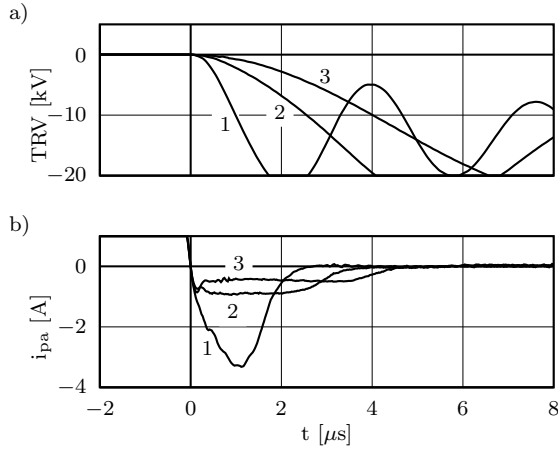


**Figure 3.8:** Results of three different measurements, performed under the same conditions (same arcing time and current), but with different TRV parameters. 1:  $C_{TRV} = 250$  pF, 2:  $C_{TRV} = 2$  nF and 3:  $C_{TRV} = 20$  nF.

The Weil-Dobke synthetic circuit is a reliable short-circuit interruption simulator, in that the strain on the AB is such that it hardly ever fails, and that the TRV always starts to rise at the desired instant after current zero. However, the shape of the short-circuit current generated by the Eindhoven circuit differs slightly from a real short-circuit, and as a result, the similarity with a real situation is quite arguable. Moreover, experiments with this circuit show that it is quite difficult to force a reignition in a VCB. The main short-circuit current's shape differs from an ideal sine-wave as a result of several of effects. First, its oscillation is damped by the inherent resistance of the circuit's components and conductors. The arc voltages of the TO and the AB further contribute to the deformation of the short-circuit current. The effect of the arc voltage on the current is observed most clearly in the time-derivative of the current, because this is approximately given by (see Figure 3.6)

$$\frac{di_{main}}{dt} \approx L_{main}^{-1} (u_{main} - u_{arc}). \quad (3.2)$$

The maximum voltage at the secondary side of the transformer is approximately 600 V. Although the voltage of vacuum arcs is relatively low (typically 20 V at low currents, and moderately increasing with increasing current), it is a significant fraction of the maximum source voltage. For lower short-circuit currents, the effect of the arc voltage on the current is even more severe, since the source voltage reduces, while the arcing voltage remains practically constant. Figure 3.9 demonstrates this.

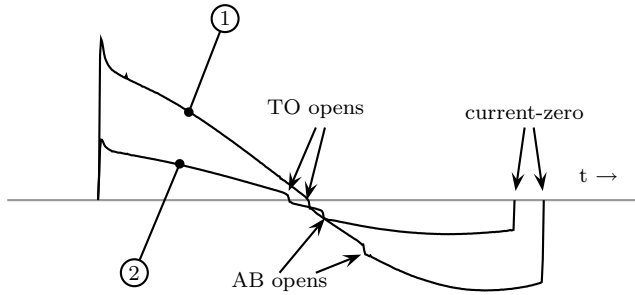


**Figure 3.9:** The main current's derivative of two different measurements. A low short-circuit current (trace 1) suffers more from the arcing voltages of TO and AB than a high short-circuit current (trace 2). One of the consequences is that trace 1 reaches current zero earlier than trace 2.

It has been experimentally determined that as a result the earlier mentioned effects, the current slope  $di/dt$  deviates between 25% lower, to 15% higher than the value that would have been expected from the measured arc's peak current. The damping effect that the circuit's inherent resistance imposes on the oscillating short-circuit current causes the  $di/dt$  to be smaller at current zero, whereas the effects from the arc voltages increase its value. As a result, lower short-circuit currents tend to have a higher  $di/dt$  at current zero, because here the arc voltage effect dominates (see Figure 3.9), but higher short-circuit currents have a lower  $di/dt$ . Figure 3.10 demonstrates this.

Since the latter effect has a pronounced influence on measurements with a relative small short-circuit current (see Figure 3.9),  $di/dt$  at current zero for these measurements is generally higher than it should be.

Although the current section has its limitations, the maximum short-circuit current that it generates lies well above the rated short-circuit current of the TO's used in this research. The highest rated short-circuit current of these breakers was 25 kA<sub>rms</sub> (35 kA<sub>peak</sub>).

The limitations of the voltage section proved to be more problematic, because the capacitors used for  $C_{inj}$  could only be charged to a maximum voltage of 15 kV. According to IEC standard 62271-100, with a supply voltage of 15 kV, this circuit is capable for performing Terminal Fault tests on breakers with voltage ratings of

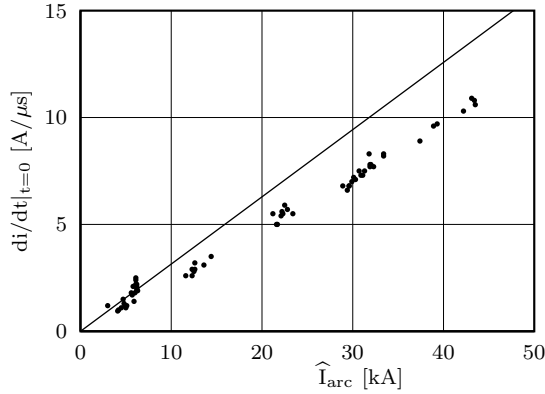


**Figure 3.10:** The current slope at current zero plotted against the peak arcing current. The dots are measured data and the solid line follows the theoretical values for 50 Hz short-circuit currents.

17.3 kV and higher. Such a rating is not used in power systems, but most of the test objects used in this project had a voltage rating of 24 kV. As a consequence, the Eindhoven current-injection circuit lacks the required voltage for properly testing these breakers.

Section 2.5 explained that the dielectric strength of a VCB increases rapidly after current zero, so apart from increasing the injection voltage, increasing the Rate of Rise of Recovery Voltage (RRRV) might also force reignition. However, like the injection voltage, the RRRV in the Eindhoven circuit was bound to an upper limit as well. Theoretically, the voltage across the TO could jump from 0 to 15 kV instantly when the TRV components are removed from the circuit (see Figure 3.6). However, a stray capacitance is always present, and experimental research revealed that the stray capacitance in the Eindhoven circuit is as low as 250 pF, whereas the stray capacitance from the TO alone is usually between 20 and 40 pF. The maximum RRRV measured in our circuit is 14 kV/ $\mu$ s, which is very high; for a 24 kV breaker intended for use in a line system, the RRRV required by the IEC in a 100% terminal fault is 1.05 kV/ $\mu$ s. Figure 3.11 demonstrates the difference.

The circuit suffers not only from stray capacitances, but also from inevitable stray inductances. Despite the low values of these inductances (several  $\mu$ H), their presence is well visible in the measurements. For example, the first excursion of the TRV in Figure 3.12 reveals an SLF-type signal superimposed on it, which results from the presence of both stray capacitances and stray inductances. Although this parasitic signal increases the RRRV, it proves to be neither an advantage nor a disadvantage for the measurements, because either its peak value was too low to be significant, or it disappears due to the post-arc conductance of the TO.

The kind of problems with stray capacitances and inductances is inherent to this

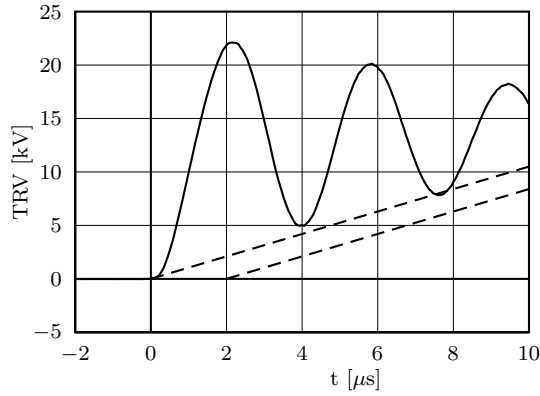


**Figure 3.11:** Solid line: the steepest TRV generated in the Eindhoven circuit, dashed lines: IEC TRV requirements for a 24 kV breaker

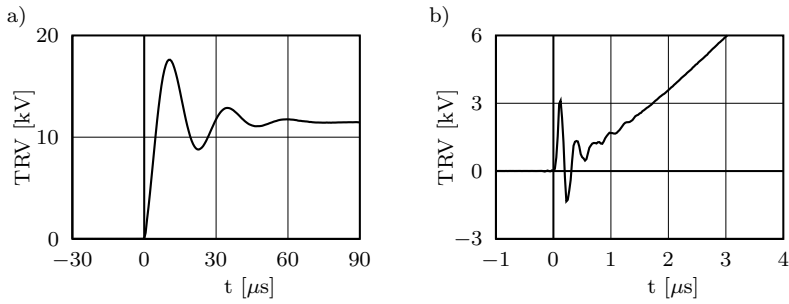


**Figure 3.12:** Parasitic components cause a high-frequency oscillation at the start of the TRV.

type of circuit. The voltage injection circuit has to be able to manage a lot of energy, because it has to deliver part of the arcing current, and a high voltage after current zero. As a result, the components are quite bulky, and consequently, they entail large stray components.

### Parallel voltage-injection circuit

The components used for the voltage injection section of Eindhoven's parallel current-injection circuit are designed to operate at a maximum voltage of 15 kV, which is generally too low for re-igniting the TO's. Increasing the TRV of this circuit implies replacing the entire voltage injection section with components that are capable of managing higher voltages. However, such components should also be able to manage a high current, which makes them large and expensive. An alternative way of achieving a short-circuit current simulation with a high TRV is by using a *parallel voltage-injection* circuit.

The basic difference of this circuit with the parallel current-injection circuit is that the voltage injection circuit is triggered *after* current zero. Hence, this section does not contribute to the arcing current, which means that the energy required for this section has become only a fraction of the former circuit. As a result, the physical size as well as the values of their components can be reduced. This not only facilitates the use of components with higher voltage ratings, but it also greatly increases the RRRV, because the stray components of the more compact circuit are much smaller. Figure 3.13 depicts the simplified parallel-voltage circuit used in this research, Appendix B describes the circuit built in Eindhoven in more detail.

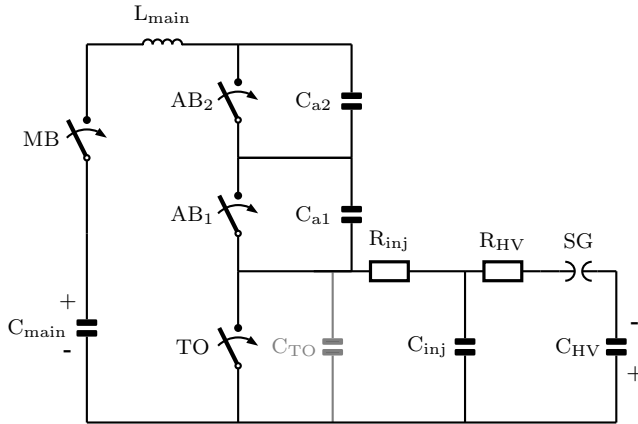


**Figure 3.13:** The parallel voltage injection circuit used in this research.

Instead of using an inductor  $L_{inj}$  for generating an oscillating TRV, this circuit uses a resistor  $R_{inj}$  of approximately 100 k $\Omega$ . The reason for this is that if the TO re-strikes, the current through the TO would be too low for a stable arc, and it would immediately interrupt again, allowing a new TRV to form instantly. In that way, it might be possible to observe the breaker's recovery curve such as the simulation in Figure 3.14 [44].

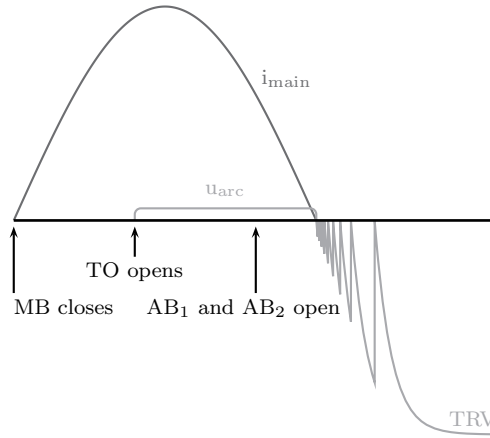


**Figure 3.14:** Simulated result from the voltage injection circuit. The arc recovery of the TO after current zero is assumed to increase linearly with time.

The current involved with the generation of the TRV in this circuit is too low for the spark-gap to operate well, and may lead to erroneous test results. To solve this problem, an additional low-impedance  $RC$  network has been added to the circuit, which is connected immediately 'behind' the spark-gap. As a result, a high current flows through the spark-gap after triggering it, which quickly charges capacitor  $C_{inj}$ . The voltage of this capacitor is then used to charge  $C_{TO}$  at a much slower rate. Because the charge from  $C_{HV}$  distributes across  $C_{HV}$ ,  $C_{inj}$  and  $C_{TO}$  during the test (the latter being all the additional capacitors surrounding the TO in the circuit as well), the voltage across the TO will be lower than the charging voltage of  $C_{HV}$ . To minimise the loss of voltage, the values for the capacitors are chosen such that

$$C_{HV} \gg C_{inj} \gg C_{TO} \quad (3.3)$$

A drawback of this circuit compared to the parallel current-injection circuit, is that this circuit requires a much more accurate triggering of the TRV. Triggering the TRV section in the parallel current-injection circuit resulted first in an arcing current, and it automatically generated a TRV after current zero. Therefore, a delay of several microseconds in the triggering of the TRV section was acceptable. Contrary to this, if the spark-gap triggers too early in this circuit, the TRV section loses charge in the TO's arc, thereby lowering, or even eliminating the TRV after current zero, whereas if it triggers too late, the TO might have already recovered from its arc.

Another drawback is that the AB in this circuit experiences more strain, since both the TO and the AB extinguish the arc (nearly) at the same time. Hence, the TRV strains the AB at the same time as the TO, but with opposite polarity. To reduce the possibility that the AB re-ignites sooner than the TO, the AB consists

of two breakers connected in series. Grading capacitances equally distribute the TRV across the breakers, but unfortunately, they reduce the RRRV as well, which complicates the choice for their value.

Connecting the ABs in series to reduce the probability that one of them re-ignites adds also in an additional arcing voltage to the secondary side of the transformer, which further reduces the arcing current due to the effect described earlier (see Figure 3.9). However, this is a rather small disadvantage compared to the risk of re-igniting an AB.

As in the Current-Injection circuit, the  $di/dt$  at current zero in this circuit is also about 15% lower than its theoretical value. However, contrary to the Current-Injection circuit, this circuit lacks the means to compensate for this.

Basically, the components  $R_{inj}$  and  $C_{TO}$ , and the charging voltage of  $C_{HV}$  determine the RRRV. This circuit has been specifically developed to generate a high RRRV, because this would increase the probability of re-igniting the TO in a test. To accomplish this, both  $R_{inj}$  and  $C_{TO}$  should be low, while the charging voltage should be high.  $C_{TO}$  has a fixed value, determined by the stray capacitances at the TO, which implies that the only way to influence the RRRV is by altering  $R_{inj}$ , or the  $C_{HV}$  charging voltage. The grading capacitances used to distribute the TRV across the AB's seriously increase the  $C_{TO}$ , thereby reducing the RRRV. As a result, by the time the TRV reaches a value at which the TO might re-ignite, a large part of the arc's residue has disappeared, which makes the experiment less interesting.

The maximum voltage that this circuit can manage is 50 kV, and  $C_{TO}$  is fixed, hence the only way to further increase the RRRV is by lowering  $R_{inj}$ . This component was kept high for the reason that if the TO re-ignites, its current will be too low to maintain a stable vacuum arc, so that it will immediately interrupt again to allow the formation of a new TRV. This new TRV enables the construction of a voltage recovery curve, such as in Figure 3.14. However, because a steep RRRV has a higher priority in this research than the correct shape of the voltage recovery voltage,  $R_{inj}$  has been reduced to 1 k $\Omega$ . With a maximum charging voltage of 50 kV, the maximum current through the TO in the case of a reignition will be 50 A. This current is just enough for a vacuum arc to remain stable for several milliseconds, and to fully discharge the capacitors in the TRV section, thereby eliminating the possibility to form a new TRV after a new current-interruption by the TO.

These two processes are clearly depicted in Figure 3.15, which shows a measured reignition with a small  $R_{inj}$ , and one with a high  $R_{inj}$ .

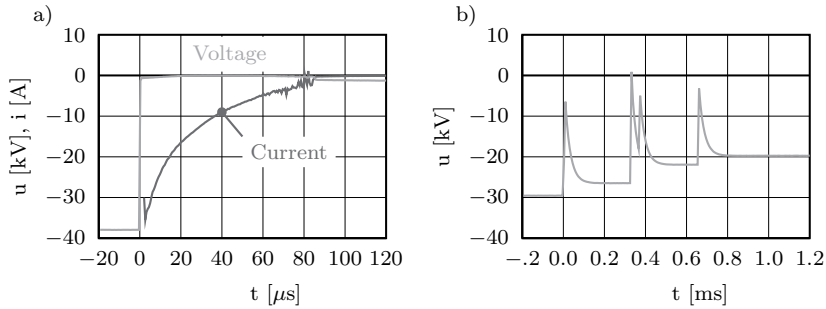


**Figure 3.15:** Reignitions measured in the voltage-injection circuit with  $R_{inj}$  equal to a) 1 k $\Omega$  and b) 100 k $\Omega$ .

### 3.3 Current and voltage measurements

#### 3.3.1 Current measurement with a Rogowski coil

This analysis focusses on observing the electrical signals of the fast short-circuit current interruption processes in a vacuum circuit breaker. Therefore, the current-measuring device should at least meet the following requirements:

1. It should produce a strong signal near the current-interruption;
2. It should be capable of managing high short-circuit currents;
3. It should have a large bandwidth to follow the fast processes during current-interruption;
4. It should suppress the distortion from ground-loop interference and electric and magnetic fields, which are particularly strong in short-circuit experiments.

One way of measuring currents is by connecting a low Ohmic shunt in series with the TO, and measuring the voltage across it, which is proportional to the current. However, for this research, a shunt fails to meet practically all of the requirements above. First, its signal near current zero is weak, compared with its signal near the maximum current. Second, despite its low impedance, it dissipates a large amount of energy from the short-circuit current. A device that is capable of managing such high currents is naturally quite voluminous. Using such a current-measuring device is not only impractical, but its inherent large stray components make it also undesirable. Finally, since it is electrically connected to the testing circuit, it takes some effort to reduce the interference from ground-loops.

Compared to a shunt, a Rogowski coil is much more advantageous for measuring the short-circuit current interruption. Such a coil is wrapped around the current-carrying conductor, and actually measures the time-derivative of the current. The short-circuit current is sine-shaped, and hence it changes slowly at its maximum value, but changes rapidly near current zero. Hence the coil's signal is



strong near current zero and weak near the high current phase, thereby satisfying the first requirement. The Rogowski coil is not part of the test circuit, and hence, its construction can be small, which automatically fulfils the second and third requirements. The absence of a connection between the coil and the circuit further implies a separation from the ground loop, which almost eliminates ground loop interference.

The drawback of using a Rogowski coil is that its signal has to be processed (which includes a time-integration) to retrieve the current, and that the absolute value of the current is unknown. Nevertheless, this is a small disadvantage compared to its advantages mentioned above, and therefore, all current measurements carried out in this research were performed with a Rogowski coil. Special software reconstructs the current numerically. Section 3.4 elaborates on this reconstruction.

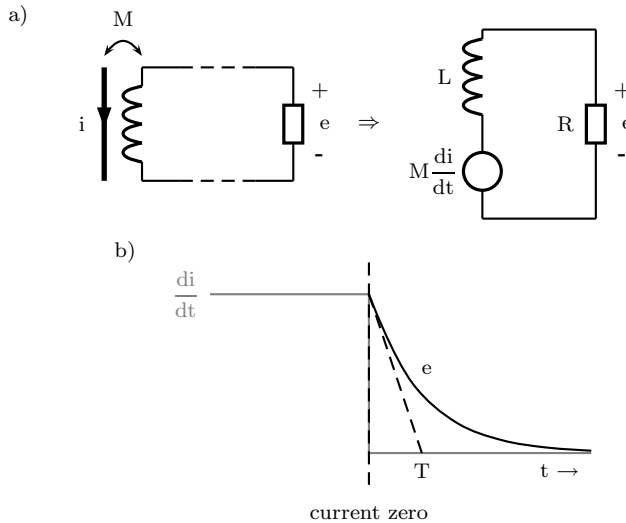


**Figure 3.16:** a) Simplified current measuring circuit with the M coil, b) the output  $e$  of the Rogowski coil in the case of an ideal current interruption.

The Rogowski coil is based on a mutual inductance between the coil and a test circuit's conductor, through which the current flows that is analysed [45, 46]. KEMA developed its own Rogowski coil (the M-coil) for specific use in short-circuit current-zero tests. Its mutual inductance is  $0.34 \mu\text{H}$  to get output voltages between 1 and 10 V with current slopes of  $10\text{--}50 \text{ A}/\mu\text{s}$ . When connected to a measuring device with a  $50 \Omega$  cable, its electrical circuit can be represented as Figure 3.16a. This circuit clarifies the relation between the current  $i$  and the coil's output voltage  $e$ , which is given by

$$M \frac{di_m}{dt} = T \frac{de}{dt} + e, \quad (3.4)$$

where  $T$  is  $L/R$ . That means that in the case of an ideal interruption at current zero, instead of dropping to zero instantly, the voltage of the M-coil decays to zero with time constant  $T$  (see Figure 3.16b). It also implies that for low frequencies, the M-coil acts as a differentiator, while for high frequencies it acts as a current transformer with ration  $1 : n$ , where  $n$  is the number of secondary turns. The time constant  $T$  of KEMA's M-coil is 440 ns.



**Figure 3.17:** Left: the KEMA Rogowski coil as it is used in the measurements, right: the Rogowski coil outside its shielding box.

Generally, a Rogowski coil has a small cross-section, a large number of turns and a large diameter, measuring the flux variation relatively far from the inducing primary conductor. In contrast, KEMA's M-coil has a large rectangular cross-section, a small diameter and a relatively small number of secondary turns (see Figure 3.17). This coil is placed in a shielding box to eliminate interference by capacitive coupling with the circuit. Such a system has a number of undesirable resonant frequencies above 10 MHz, due to the stray capacitance of the coil. This distortion is suppressed by placing damping resistors parallel to sections of the windings (see Figure 3.18).

Figure 3.19 shows the M-coil voltage signal of a short-circuit test on a VCB with the parallel current-injection circuit of Figure A.1.

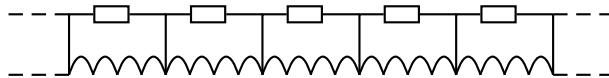


**Figure 3.18:** Arrangement of the damping resistors for suppressing resonant frequencies in KEMA's M-coil.

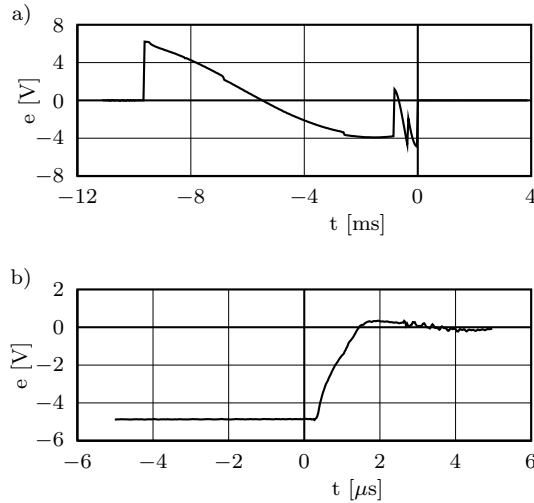


**Figure 3.19:** KEMA's M-coil voltage signal of a short-circuit test, performed in a parallel current-injection circuit. a) the complete test, b) the signal zoomed in to current zero.

### 3.3.2 Voltage measurement

A single channel voltage measurement makes it difficult to measure both the TRV and the arc voltage at the same time at a high resolution. When, for example, a recorder measures a TRV with a peak value of 15 kV at 12 bits resolution, and a dynamic range of  $\pm 20$  kV, the smallest voltage step is about 10 V. This is too inaccurate for measuring the vacuum arc voltage in the same measurement, and therefore, two voltage measurements are performed at the same time, but with a different dynamic range.

While the current measurement suffers from a stray capacitive current, the voltage measurement suffers from a stray inductive voltage. This effect is particularly prominent in the region of interest, i.e. the current-zero region, since here, the time change of the current and voltage is largest. Like the stray capacitive component in the current measurement, numerical processing reduces the inductive component from the voltage measurement. However, the software does not remove distortion from a ground loop, and due to its electrical connection with the test circuit, the voltage measuring system is more vulnerable to this kind of distortion than the current measuring system. As a result, reducing ground loop interference in the voltage measuring system requires more attention than in the current measuring system.

Eventually, the voltage signal is also used to suppress the stray-capacitance distortion in the current signal. This requires the time-derivative of the voltage, but by time-deriving a measured signal, its inherent high-frequency thermal noise becomes more pronounced. It is possible to filter this distortion out of the signal numerically,

but it is more convenient to measure the signal with a high signal-to-noise ratio straight away.

To summarise, the requirements for the voltage measuring system are:

- 1. The signal-to-noise ratio should be high;
- 2. The voltage should be measured at two different resolutions;
- 3. It should adequately suppress ground loop interference.

The TRV reaches values that are too high for most recording devices, and therefore, the voltage probes attenuate the voltage first. In this research, high-Ohmic voltage probes, with 100 M $\Omega$  impedance and a bandwidth of up to 100 MHz measure the voltage at a ratio 1:1000. Details of the probes used in this research are listed in Table 3.1.

**Table 3.1:** Voltage probe details

Circuit	Rating	Manufacturer	Series	Figure
Current-Injection	20 kV	PMK	PHV 4002	3.20 left
Voltage-Injection	40 kV	Northstart	PMV-1	3.20 right



**Figure 3.20:** Left: the PMK voltage probe, right: the Northstar voltage probe.

The low-voltage (high resolution) part of the test requires also a high voltage probe, since it also has to cope with the high TRV. This introduces a practical lower limit to the RMS value of the noise level of a test. The typical RMS noise level on a probe lead is about 0.1 mV. Multiplied by the attenuation factor, this value becomes 0.1 V, and hence, measuring the low voltage signal at a higher resolution than 0.1 V is useless.

One way of reducing the interference from the ground loop is by measuring the voltage across the TO with two probes, connected to a differential amplifier, as de-

picted in Figure 3.21. In this way, the electrical path from the test-circuit to the recording device is high Ohmic, thus obstructing the current flowing between the test circuit and the measuring circuit. Moreover, closely tied co-axial probe leads experience approximately the same amount of induced voltage on their outer conductor, and when the differential amplifier works properly, it automatically removes this common-mode voltage from its output [34].

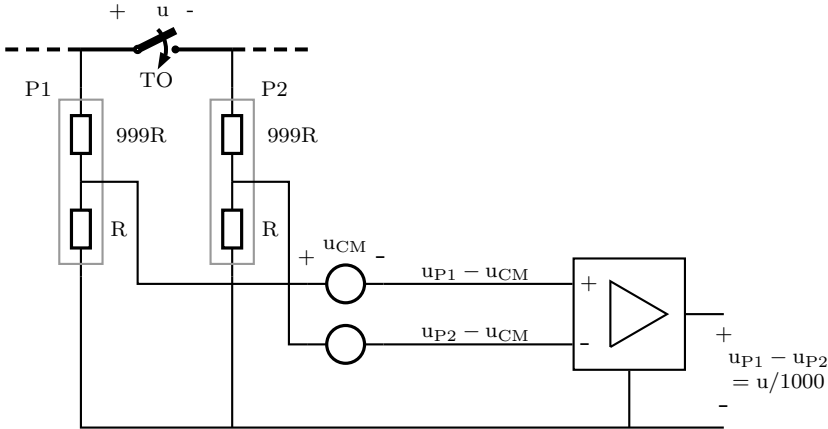


**Figure 3.21:** Voltage measuring with a differential amplifier. The voltage probes are shown as voltage dividers.  $u_{CM}$  = common-mode voltage.

A better way of eliminating ground loop interference is by using special battery-operated buffers (Front Ends) that transform the electrical signal into an optical signal, see Figure 3.22. The optical wire ensures electrical isolation between the voltage probe and the recording device. Moreover, if the optical transmitter first digitises the signal, its transmission is essentially noise free. Compared to the voltage divider system described before, the Front End system has the additional advantage that the signal can be transmitted over a long distance, without losing bandwidth, or adding noise.

The earlier version of Front Ends, used in this research, which were developed by KEMA, first store the signal at a high sampling frequency, and transmit it digitally afterwards at a slower transmission rate. This method made it easier to develop the optical transmitter-receiver system, but it also puts a limit to the maximum recording time, which is then determined by the Front End's memory.

Another type of Front End used in this research transmitted an analogue optical signal by using an FM carrier wave. This system transmits the signal directly, and as a result does not have a recording time limit. However, analogue signals are more sensitive to picking up noise, and this system's signal to noise ratio was about 60 dB. The noise level on the TRV from this signal severely distorts the current trace, when the current was compensated for the stray capacitive component.

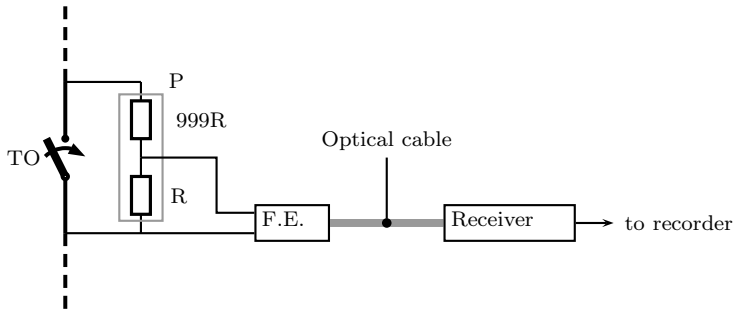


**Figure 3.22:** Voltage measuring with a Front End system.

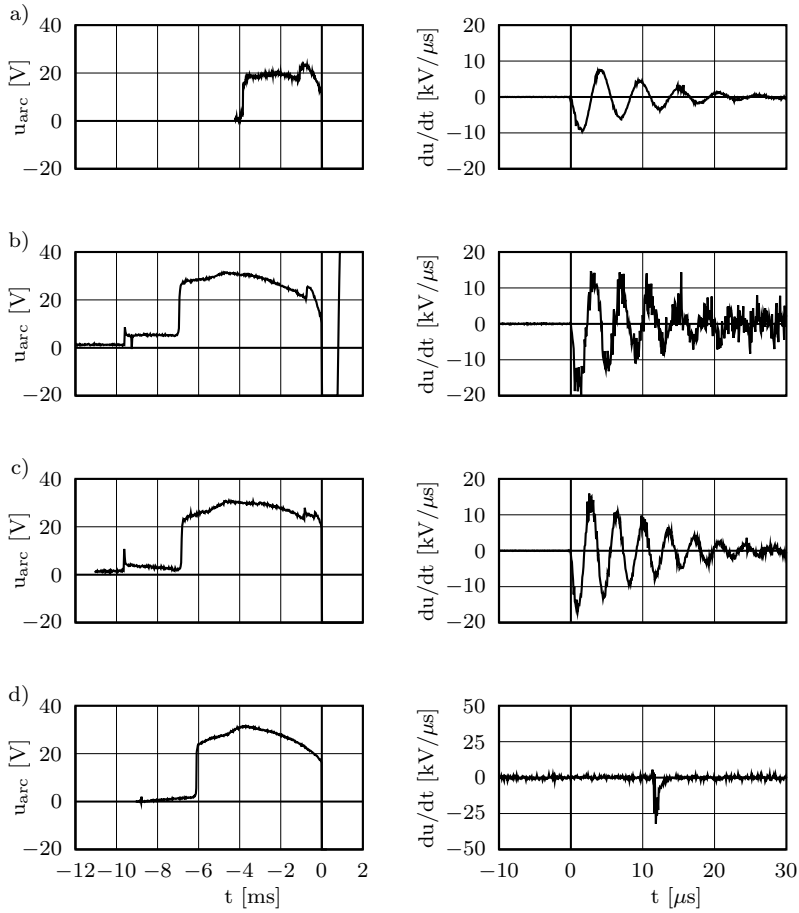
Compared to the voltage divider system, the Front End system is more complicated, and hence more expensive. Moreover, when using two Front Ends to measure the voltage at two different scales, each Front End requires its own (also expensive) voltage probe. This is because of a safety measure for the Front End's vulnerable electronics, which drops the input impedance as soon as the input voltage exceeds the pre-set voltage range. When a single high-Ohmic voltage probe is connected to two Front End systems that measure at different scales, the reduced input impedance of one Front End also disturbs the signal at the other Front End.

Figure 3.23 shows the results of the high resolution voltage measurements, performed with the different systems. These signals have not been numerically compensated for the voltage from the stray inductance.

### 3.3.3 Data acquisition with transient recorders

The Rogowski coil and the voltage measuring systems, described in the previous sections, measure the (time derivative of the) current, the arcing voltage and the TRV with high quality. A *transient recorder* records, digitises and transmits these signals to a personal computer for processing. To maintain the quality of the signals, such a transient recorder should

1. record the signals at a high sampling frequency;
2. record the signals at a high resolution;
3. record at least three signals (the arcing voltage, the TRV and the current);
4. record a minimum time-window;
5. transform the signals into digital formats, suitable for processing them on a pc.



**Figure 3.23:** The arcing voltage (left) and the time-derivative of the TRV (right) acquired with different measuring systems. a) data from the KEMA Front End system, b) data from the analogue optical Front End system, c) Data from the differential amplifier system and d) data from the digital optical Front End system.

Some of these requirements are already met by Front Ends (described in Section 3.3.2), in which case the task of a transient recorder is limited to collecting the data, and transferring it to the pc.

During the course of this research, two different principles of transient recording systems have been used, which are schematically represented in Figure 3.24. The first system used the configuration of Figure 3.24a, and has been developed by KEMA. Its Front Ends are already described in Section 3.3.2. The amount of memory in the Front End of this system determines the maximum time-window of one recording, which is not the case in the second system (Figure 3.24b). Here, the transient recorder receives analogue voltage signals, which gives the option of using a Front End - Control Unit system to transmit the signals, or connecting the probe directly to the recorder. Transferring analogue signals over a long distance decreases the signal's bandwidth, and makes it more receptive to noise, hence the signal to noise ratio of the second system is a little worse than that of the KEMA system.

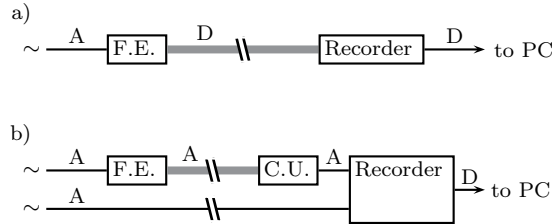


**Figure 3.24:** Schematic representation of the transient recording systems. A = analogue signal, D = digital signal and C.U. = Control Unit. The black and grey lines are electrical and optical signals, respectively.

The recorder used in the configuration of Figure 3.24b was initially an LDS-Nicolet Sigma oscilloscope, which was later replaced by an LDS-Nicolet Genesis transient recorder. This transient recorder consists of a main-frame which supports one or more receiver cards. Initially, a four-channel receiver card was used with electrical (analogue) channels, which was later replaced with a receiver card, holding four optical (digital) channels. This significantly improved the signal to noise ratio, as can be seen in Figure 3.23. However, it seems not to suppress noise as well as the KEMA system, but the reason for this is the increased sampling frequency. Because the latest transient recorder system measures at a higher sampling frequency than the KEMA system, it measures at a larger bandwidth, and as a result, it also measures a larger noise bandwidth.

Table 3.2 summarises the properties of the used transient recorder systems.



**Table 3.2:** Performance of the transient recording systems.<sup>1</sup>The maximum recording time is limited by the amount of free memory on the pc.

	KEMA	Sigma	Genesis A	Genesis D
Manufacturer	KEMA	LDS	LDS	LDS
System	CZM	Sigma Oscilloscope	Genesis Transient Recorder	Genesis Transient Recorder
Channels (#)	3	8	4	4
Resolution (bits/% of scale)	12/0.02	12/0.02	14/0.006	14/0.006
Sampling rate (MS/s)	40	100	100	100
Max. recording time (ms)	6.5	10	$\infty$	$\infty$
Input signal	Optical	Electrical	Electrical	Optical

### 3.4 Numerically processing the data

The measured data must be processed in order to find the actual arc voltage and arc current. It is not only necessary to integrate the Rogowski-coil's output in order to determine the current, but it is also necessary to take into account the non-ideal differentiating behaviour of the device. Additionally, the disturbance from the stray capacitance and inductance, represented in Figure 3.25, should be removed from the signals.

Figure 3.25 shows that the arc voltage and the arc current can be derived from the measured traces by means of the following equations

$$u = u_m - L_p \frac{di_m}{dt} \quad (3.5)$$

$$i = i_m - C_p \frac{du}{dt} = i_m - C_p \frac{du_m}{dt} + L_p C_p \frac{d^2 i_m}{dt^2} \quad (3.6)$$

Special software numerically processes the measured data. It recovers the arc voltage and arc current in the following successive steps.

*Determining the approximate value of the voltage-zero instant*

As explained in Section 3.3.1, the current-measuring device used in this research is unable to measure the absolute value of the current. It is assumed that the arc has a resistive nature, and as a result, the voltage and the current should be zero at the

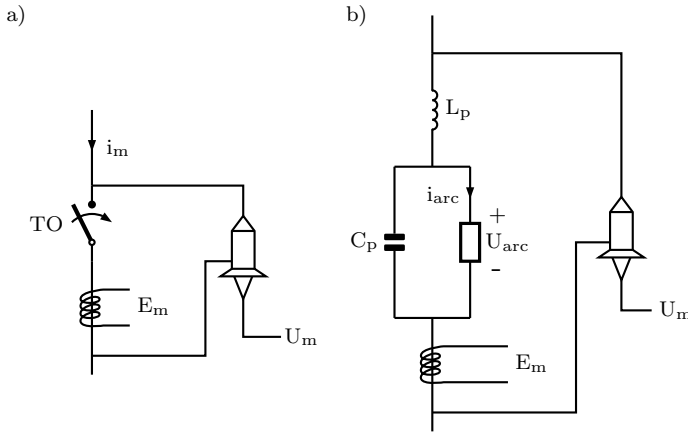


**Figure 3.25:** A circuit that incorporates the presence of stray components in the test set-up.  $E_m$  and  $U_m$  are the measured quantities.

same time. Hence, the absolute value of the current can be determined by searching for the zero in the voltage signal.

The voltage of a vacuum arc is only several tens of volts and even decreases as the current approaches zero. As a result, the voltage across a stray inductance  $L_m$  can distort the measured arc voltage quite easily. For instance, if the stray inductance is  $1 \mu\text{H}$  and the current slope  $di/dt$  is  $10 \text{ A}/\mu\text{s}$ , the induced voltage that is measured becomes  $L_m \frac{di}{dt} = 10 \text{ V}$ . This has ultimately a disturbing effect on the determination of the exact voltage-zero instant, which is therefore only an approximation.

### *Trace smoothing*

Equations (3.5) and (3.6) imply that the determination of  $u$  and  $i$  also require the time-derivative of the measured signals. As can be seen in Figure 3.23, the derivative can contain a strong level of high-frequency noise, which would eventually also distort the recovered signals. The software reduces this noise numerically by applying a low-pass filter to the measured traces.

### *Frequency correction*

The KEMA system uses Front Ends that digitise the signals at a sampling frequency of  $40 \text{ MS/s}$ . Since they all generate their own sampling frequency, a small difference in their clock frequency is inevitable. However, a small difference in their sampling frequency might cause a significant time-shift error. For example, if the current zero is at  $1.5 \text{ ms}$  after the start of the recording, and the frequency difference between the signals of two Front Ends is only  $500 \text{ Hz}$  (which is a realistic value), while they

sample at a rate of 40 MS/s, the time difference between the signals at current zero is almost one sample (25 ns). To overcome this error, the software artificially synchronises the sampling frequencies of the signals by first linearly interpolating the original signal, and sampling the result with the new sampling frequency (see Fig. 3.26).

Determination of the difference between the sampling frequencies of the Front Ends happens before each test series, by connecting a high-frequency pulse generator simultaneously to all the Front Ends. The resulting signals should match each other.

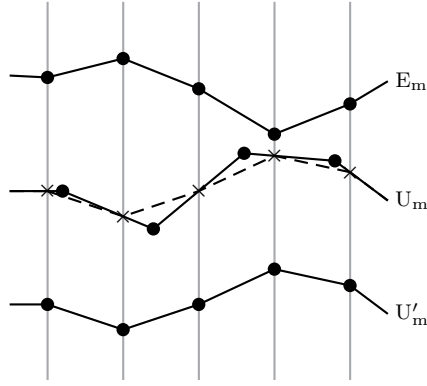


**Figure 3.26:** Re-sampling of trace  $U_m$  for synchronising it with trace  $E_m$ .  $U'_m$  is the result. The difference between the sampling frequencies of  $E_m$  and  $U_m$  in this simulated example have been greatly exaggerated to demonstrate the process.

#### *Computing integration constant $ds$*

When taking into account the inherent offset  $ds$  of a Front End that adds to the Rogowski-coil's signal  $e$ , Equation (3.4) becomes

$$M \frac{di_m}{dt} = e + T \frac{de}{dt} - ds, \quad (3.7)$$

and hence, the current is found by time-integrating Equation (3.7) as

$$i_m(t) = M^{-1} \left[ \int_{t_1}^t e(\tau) d\tau + T(e(t) - e(t_1)) + i_m(t_1) - (t - t_1)ds \right], \quad (3.8)$$

where  $t_1$  is the start of the measurement's time-frame. The offset  $ds$  can only be found automatically if a voltage zero has been detected. Using an average value of  $ds$ , e.g. obtained from an offset measurement, is not appropriate, because even the

slightest error leads eventually to a large error in the current-measurement. Moreover, the noise on the  $e$ -trace is also numerically integrated, which gives unreliable results at large time-windows. Therefore, the current is only accurate for small time windows of several  $\mu\text{s}$ .

The software assumes that 5  $\mu\text{s}$  after current zero, the post-arc current has decayed to zero, and that the current remains zero afterwards. With the instant of current zero (voltage zero) determined earlier, the software computes  $ds$  by taking the average of the  $e$  samples between 5 and 10  $\mu\text{s}$  after current zero. Like the voltage-zero instant,  $ds$  can also be determined manually if the computer was for some reason unable to determine it by itself.

### *Computing $di_m/dt$*

Equations (3.5) and (3.6) imply that solving  $i$  and  $u$  requires their time-derivatives in order to eliminate the influence of the stray components. Although the Rogowski-coil has already measured the time-derivative of the current, from Equation (3.7) it follows that  $e$  should also be differentiated to obtain  $di_m/dt$ .

For the numerical differentiation, the software makes use of the 5-point differentiation method [47, 48]. If  $dy/dt_k$  is the  $k$ -th element of the derivative of vector  $y_k$ , then  $dy/dt_k$  is calculated by

$$\frac{dy}{dt_k} = \frac{y_{k-2} - 8y_{k-1} + 8y_{k+1} - y_{k+2}}{12}. \quad (3.9)$$

### *Computing $u(t)$*

As already explained in Section 3.3.2, two channels measure the voltage at different resolution to obtain the highest possible accuracy. Each short-circuit test starts with a (relatively) low voltage, i.e. the arcing voltage, followed by a high TRV. The software searches for the point at which the signal that measures the arc voltage starts to clip, and replaces the remainder of this trace with the signal that measured the TRV.

After that, subtracting  $L_p di_m/dt$  from this result finally leads to  $u(t)$ .

### *Computing $t_0 = 0$ at Voltage Zero*

The newly obtained voltage signal allows a better estimation of its zero crossing.  $t_0 = 0$  is therefore updated before continuing the recovery of the signals.

### *Computing $i_m(t_1)$ and $i(t)$*

The only missing component for the current trace is its integration constant  $i_m(t_1)$  from Equation (3.8). Solving this equation without the integration constant automatically gives this value at time  $t = 0$ . Finally, the software recovers  $i$  by differentiating the earlier obtained  $u(t)$ , to make the subtraction of  $C_p du/dt$  in Equation (3.6) possible.

#### *Iteration to determine Voltage Zero accurately*

The program started with determining the voltage-zero of the voltage, that has not been compensated for the stray inductance component initially. As a result, the actual arc's voltage-zero might be different than the one determined here, and this error continues to disrupt the results in the following steps.

To reach an improved result, the program derives the voltage-zero again from the voltage acquired in the course of the evaluation, and uses this value to evaluate the whole scheme again. It repeats this iterative process until it reaches a pre-defined accuracy.

#### *Manual verification*

Although the software recovers the arc's current and voltage to a high level of accuracy already, the results require manual verification to improve it even further. For instance, the software assumes that the current is zero from  $5 \mu s$  after current zero and later. This assumption is used for determining the value of  $ds$ . The post-arc current in vacuum circuit breakers can easily last longer than those  $5 \mu s$ , which leads to an error in the results, which can only be corrected by manually supplying the value for  $ds$ .

Moreover, the Rogowski coil suffers from an effect that has not been taken into account yet, but also distorts the results. This effect works as follows. A metal shielding box protects the Rogowski coil from picking up stray magnetic fields. This box contains small cuts to limit the eddy currents, but nevertheless, the eddy currents impose a small additional (decaying) stray magnetic field on the Rogowski coil after current zero. This results in an error such as in Figure 3.27a. The solution to these problems is to manually determine the integration constant  $ds$ , and to analyse the current at small time-windows.

The current offset determination sometimes requires manual intervention as well. One aspect of current interruption in vacuum is that near current zero, the voltage changes slowly, and sometimes remains below the noise level for some time, which makes determination of the voltage-zero particularly difficult. In that case, the offset can also be determined by searching for the instant in time at which the post-arc current becomes zero, but this is impossible if the breaker re-ignites during a post-arc current, such as in Figure 3.27b. The best way to determine the current's offset in such a case is by comparing it with an equivalent measurement in which the post-arc current did reach zero.

The final example that demonstrates the need for careful interpretation of the results also relates to the determination of the current-offset. If the settings are such, that the Rogowski coil's output clips, i.e. becomes larger than the measuring range, a significant fraction of the signal is integrated incorrectly, which eventually leads to an offset-error. Figure 3.27c shows a measurement performed with the parallel-voltage injection circuit (see Section 3.2.2), in which the spark gap triggered about  $30\text{ }\mu\text{s}$  after current zero. This introduced high frequency, high amplitude signals on the  $e$  trace, and as a result it clipped, which eventually resulted in the correct recovery of the current signal, but one that has a different offset after the spark-gap trigger event.

### 3.5 Conclusions

This chapter described the acquisition of the voltage and current traces of short-circuit interruption with VCB's. It started with describing the test circuits in which the TO's were subjected to a short-circuit current, followed by a TRV after current-interruption. The tests were performed at different laboratories in the Netherlands, i.e. KEMA in Arnhem, a laboratory with enough short-circuit power to perform direct tests, and Eindhoven University of Technology, which has less short-circuit power. The latter laboratory uses synthetic test circuits to simulate a short-circuit current interruption, in which different circuits generate the high current part and the high voltage part. For cost and time reasons, the Eindhoven laboratory has been used most frequently for this research.

Special equipment measured the current and voltage traces in the TO's during a test with high accuracy. Measuring the low values of currents and voltages around current zero, while also coping with the high currents and high voltages at other instants of the test required special effort for shielding and isolating the measuring devices.

Transient recording systems collected and sampled the voltage and current traces, and transmitted them in digitised format to a personal computer. A program that has specifically been developed for this purpose, recovers the current and voltage of the vacuum arc from the measured signals, which are manually verified and, if necessary, corrected.

Measuring the current and voltage traces of the vacuum arc during current-interruption requires many steps. Analysing this would require probes inside the TO's. This, however, is impossible without destroying the vacuum. Instead, probes measure the current and voltage of the entire breaker, from which intelligent software deduces the vacuum arc's electrical properties. In the end, as a result of the careful design of the measuring system, it gives the arc's electrical properties with high accuracy.

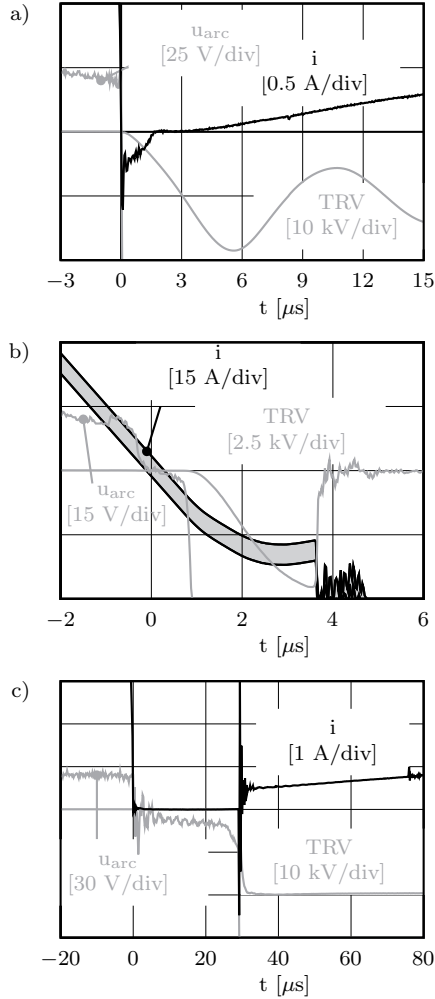


**Figure 3.27:** Common problems with the recovery of the current. a) Integration of noise on the  $e$ -trace leads to an accumulating error in the current, b) the low voltage near current zero makes it difficult to determine the current's offset and c) clipping of the  $e$ -trace, approximately 30  $\mu s$  after current zero results in different current offsets in one measurement.





# Chapter 4

## Post-arc current research

### 4.1 Introduction

The measured results are analysed for relationships between the post-arc properties, such as the peak post-arc current, and the test settings, such as the peak short-circuit current and the arcing time. Such analysis has been performed extensively in the past, as mentioned in Section 2.4. The general conclusion is that the post-arc current depends not only on the test settings, but also on uncontrollable aspects, such as the final position of the last cathode spot. As a result, the peak value of the post-arc current of one test can be twice as large as the result obtained in the previous test, even though both tests were performed under the same conditions. To still be able to observe a relationship between the arc and the post-arc conditions, a large number of tests should be performed under equal test settings, as has been done in this research.

The data obtained in this work resulted from measurements on one of the three test objects listed in Table 4.1. All breakers had contacts consisting of 75% Cu and 25% Cr, and had AMF type contacts (see Section 2.3.2). The breakers are commercially available, and their maximum contact separation (stroke), as well as their opening velocity, is determined by their driving mechanism and cannot be adjusted. The average value for the maximum gap length and the opening velocity are 10 mm and 1 m/s, respectively. In this research, the gap length of a given measurement at current zero is determined by multiplying the arcing time with the average opening velocity, i.e. we assume that the opening velocity is constant. This approximation agrees well with the results obtained from direct measurements of the gap length.

Table 4.2 lists the details of the test series that are used for analysis. In addition to this table, the following list summarises the intention of each test series, and the item numbers correspond with test series numbers:

**Table 4.1:** The types of circuit breaker used in this research.<sup>1</sup>This refers to the way in which the AMF is generated.

#	Short-circuit current rating [kA]	Voltage rating [kV]	Contact configuration <sup>1</sup>
A1	20	24	Horse-shoe
A2	25	24	Horse-shoe
B	20	12	Coil

1. SLF tests according to IEC requirements [37];
2. Post-arc current investigation with a wide range of arcing times, and short circuit currents that exceeded the breaker's rated current;
3. Current interruption capability tests in an SLF circuit, where high currents and long arcing times were used;
4. Same as in 3, but performed in a Weil-Dobke circuit;
5. Research on the relation between the rate of rise of recovery voltage (RRRV) and the post-arc current;
6. Same as in 3, but this time with more variation in the short-circuit current;
7. Reignition analysis.

This chapter starts with the analysis on various aspects of the measured post-arc current, and their relationship with the arcing conditions in Section 4.2. Section 4.3 compares the post-arc current properties with each other. One striking phenomenon that needs a detailed description is that the voltage remains nearly zero in the first tens of nanoseconds after current commutation. Section 4.4 gives a qualitative explanation for this event, and Section 4.5 summarises the conclusions of this chapter.

## 4.2 The arcing properties compared with post-arc properties

The post-arc current is the result of a residue from the vacuum arc. As such, it should contain information about the impact of the arc on the VCB, for example to what amount local melting of the anode occurred during the high-current phase. In that case, it should be possible to analyse the breaker without having to actually destroy it to look inside. Since we were not able to measure physical processes inside the breaker, such as the vapour pressure or the anode temperature, this section

**Table 4.2:** The properties of the test series discussed in this research.<sup>1</sup>Number of current-zero measurements obtained in the particular test series.<sup>2</sup>The rate of decay of the short-circuit current at current zero. For tests in the Weil-Dobke system, these values do not always correlate to  $\hat{I}_{arc}$ , because of the non-correlating settings for the main and the injection current (see also Section 3.2.2).<sup>3</sup>The rate of rise of the inherent recovery voltage.<sup>4</sup>A number of tests in this series was performed with an asymmetric short-circuit current (see Section 3.2.1).

test-series #	breaker	circuit	# <sup>1</sup>	$\hat{I}_{arc}$ [kA]	$t_{arc}$ [ms]	$di/dt^2$ [A/ $\mu$ s]	$du/dt^3$ [kV/ $\mu$ s]
1	B	KEMA SLF	24	21.6 – 27.4	0.2 – 10.0	6.7 – 10.0	3.3 – 5.6
2	A1	Weil-Dobke	77	36 – 50	1.5 – 9.6	7.4 – 9.6	7.5 – 14.0
3 <sup>4</sup>	A1	KEMA SLF	45	13.5 – 34	1.3 – 10.7	5.1 – 12.1	4.5
4	A1	Weil-Dobke	60	22.2 – 41.8	4.9 – 9.7	9.5	11.0
5	A2	Weil-Dobke	32	9.4 – 46.5	6.0 – 9.7	8.0 – 15.0	3.5 – 12.5
6	A1	KEMA SLF	21	16 – 40	1.8 – 10	5.1 – 12.2	2.7 – 7.4
7	B	Voltage- Injection	128	5 – 45	1.2 – 8.8	1.0 – 11.0	32.0
8	B	Voltage- Injection	100	5 – 45	1.0 – 10.0	1.0 – 10.0	30.0

searches only for relationships between electrical arcing and externally measurable parameters.

Other researchers have analysed the post-arc current extensively in the past, but found very little relationship between the arcing conditions and post-arc current, as has already been described in Section 2.4. The measurements performed in this research confirm this experience. Compare, for example, the two post-arc currents in Figure 4.1, which were taken from Test Series 3. The arcing time and short-circuit current of these tests were practically equal, but nevertheless, one measurement shows a post-arc current that is nearly twice as large as the other. In addition, Figure 4.2 shows the cumulative distribution of the post-arc current's peak value  $\hat{i}_{pa}$  after a series of tests with equal arcing time and short-circuit current. The scattered results demonstrate how stochastically these parameters behave.

Noting the above difficulties, the analysis is from here onwards conducted on large numbers of tests simultaneously. This should provide us with reliable information for our analysis. For this purpose, one aspect of the post-arc current is chosen as characteristic parameter for one specific test (for example its peak value, or its value at a given time after current zero). When a large enough number of tests is performed, such a characteristic parameter might eventually evolve into a distribution with a clear trend. This trend can then be compared with arcing conditions to

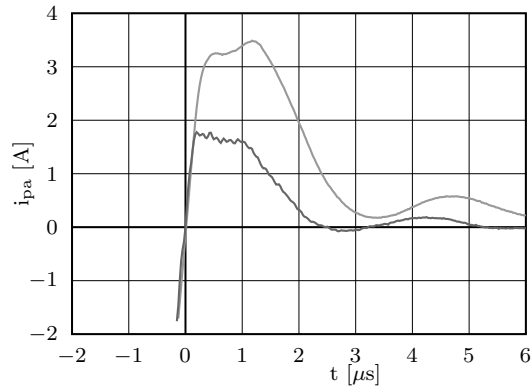


**Figure 4.1:** The post-arc currents obtained in two identical tests.

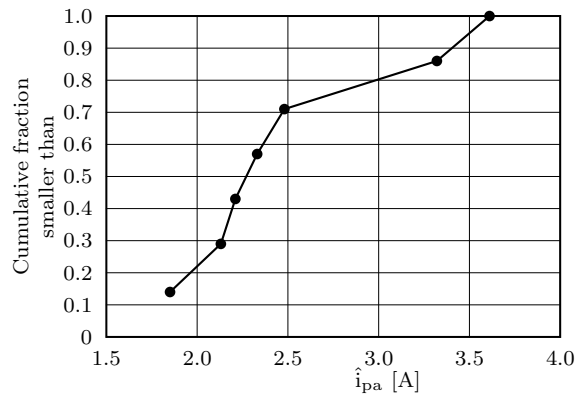


**Figure 4.2:** Cumulative distribution of the post-arc current's peak value after identical test conditions. The divergence in the results are probably from the last cathode spot's final position.

search for relationships.

In the ideal situation, the influence of one arcing condition on the post-arc current can be analysed by adjusting one test setting, while keeping all the other settings fixed. However, the control unit that controls the opening, closing and triggering of both the breakers and the spark gap in the synthetic test circuit, as well as the relays controlling the drivers of the breakers, introduced an unavoidable scatter with a standard deviation of about 0.7 ms in the arcing time. In a similar way, the short-circuit current also shows scatter of up to 10 % of its adjusted value. This makes the proposed research method quite difficult. To overcome these problems, after obtaining a series of tests, the tests with nearly equal arcing times were gathered to research the influence of the short-circuit current, and vice versa.

Figure 4.3 demonstrates the influence of the short-circuit current on the peak value of the post-arc current. These test results are from Test Series 5, where the arcing time and the rate of rise of recovery voltage are fixed at 8 ms and 12 kV/ $\mu$ s, respectively. This result is similar to those presented in [18, 49], and it clearly shows a (linear) relation.

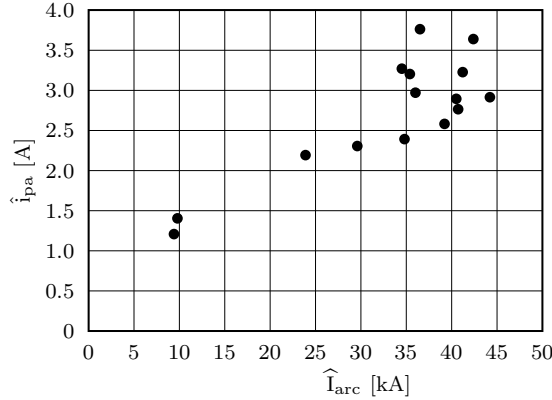


**Figure 4.3:** Post-arc current's peak value versus the short-circuit current's peak value. The data is from Test Series 5

Although the data in Figure 4.3 is insufficient for drawing explicit conclusions, extrapolation of the trend towards  $\hat{I}_{arc} = 0$  seems to result in a non-zero value for  $\hat{I}_{pa}$ . An explanation for this might be that these results are obtained with the double synthetic current-injection circuit, which has a fixed current slope  $di/dt$  at current zero that is independent of the main current. It is likely that the conditions just prior to current zero (such as  $di/dt$ ) have significant influence on the post-arc current conditions, which is indeed confirmed in the literature [50].

The next aspect of research concerns the influence of the arcing time  $t_{arc}$  on the post-arc current's peak value. Changing the arcing time has two effects on the breaker's arcing conditions. First, it changes the time for which the arc strains the

contacts, and second, due to the contact opening velocity of about 1 m/s, the arcing time changes the inter-electrode volume at current zero. With the type of tests used for this research, where the short-circuit current is not constant in time but changes sinusoidally, it is especially difficult to distinguish between the influence of those two effects separately on the post-arc current.

Despite these obstacles, a trend should be visible in the relation between the arcing time and the post-arc current peak. Both the longer arcing strain and the increased contact distance increase the residual charge at current zero, because an arc that lasts longer produces more charge, and a larger gap can contain more of it. Figure 4.4a depicts an example of such a relationship, and it shows indeed a trend, though clouded with scatter. These results are from Test Series 2, with an  $\hat{I}_{arc}$  between 36 and 38 kA.

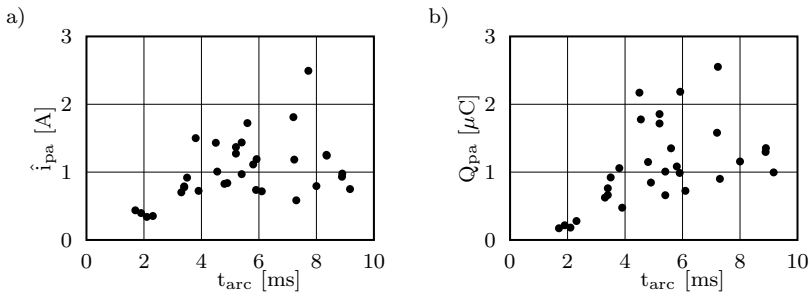


**Figure 4.4:** a) post-arc current's peak value versus the arcing time and b) the post-arc current's charge versus the arcing time. The data is from Test Series 2.

When the load increases in strength (a higher short-circuit current), the anode surface melts and leaves a vaporising pool of liquid contact material behind after current zero. As soon as this happens, the post-arc current's peak value suddenly increases much faster, as is demonstrated in Figure 4.5.

Another way of characterising the relationship between arcing and post-arc conditions is by time-integrating the post-arc current. The result of this operation is a charge that reflects the amount of charge that was present at current zero. Moreover, this method blends both the post-arc current's peak value and the duration into a single figure, thus possibly reducing the amount of data required to analyse. Figure 4.4b depicts such a relationship. It shows the post-arc charge  $Q_{pa}$  of the same measurements as used in Figure 4.4a, compared with  $t_{arc}$ . The relationship in Figure 4.4b is hardly better than that of Figure 4.4a.

So far, only the post-arc current has been analysed. Before continuing the search for trends, the following researches the time change of the post-arc conductance, which involves the TRV.

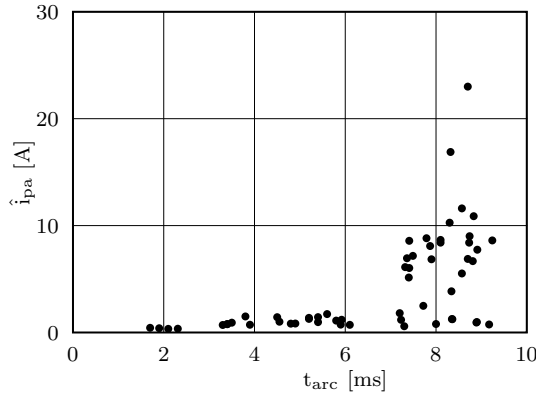


**Figure 4.5:** The same relationship as in Figure 4.4, but now including the results from tests with a particularly high short-circuit current.

The fact that a post-arc current flows after current zero implies that the breaker conducts during this time. That means that the breaker interacts with the circuit, and that the post-arc current has an influence on the shape of the TRV, as Figure 4.6 indeed clearly demonstrates. This figure shows details of two successive current zeros, measured in an asymmetrical test of Test Series 3. The breaker re-ignited shortly after the first current zero, which followed a major current-loop (see Section 3.2.1), but it cleared on the second, after a minor current-loop. The polarity of the current and voltage in Figure 4.6 has been manually altered to make the comparison between the results in this figure easier. It is clear that the high post-arc current in Figure 4.6b alters the TRV. It also shows that a large post-arc current delays the TRV, and that its derivative is smaller than in the case of a small post-arc current. Whether or not this is beneficial for current interruption is discussed in Chapter 5.

Figure 4.7 shows the breaker's post-arc conductance in time. Due to its fast transition over a large dynamic range, this conductance is plotted on a logarithmic scale. Before current zero, both tests show an equal decaying arc conductance, but soon after current zero, the conductance drops several orders of magnitude within microseconds, which explicitly demonstrates the breaker's fast transition from a good conductor to a good isolator.

Trace 1 in Figure 4.7 shows an oscillation in its decay towards zero. This indicates that  $G$  is not a pre-determined exponentially decaying function, but instead it depends on the TRV as well. In fact, it depends on the time change of the TRV as becomes clear below.

As soon as the TRV starts to rise, the electric field in front of the post-arc cathode repels electrons and attracts ions, as described in Section 2.4, and illustrated in Figure 2.6. Although the opposite is to be expected in front of the post-arc anode, this effect is negligible within the time-frame of the post-arc current processes, because

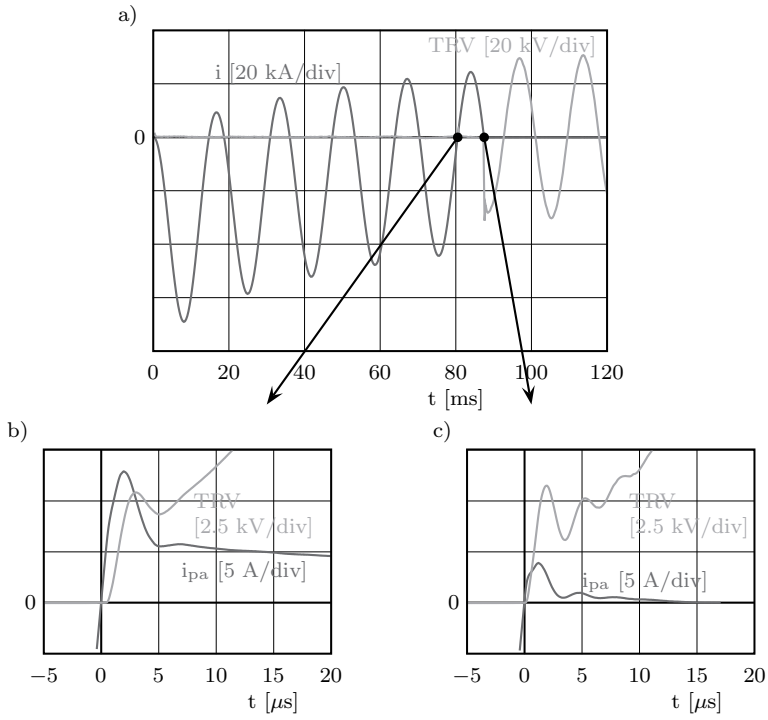


**Figure 4.6:** The influence of the post-arc current on the TRV. These results are from Test Series 3.

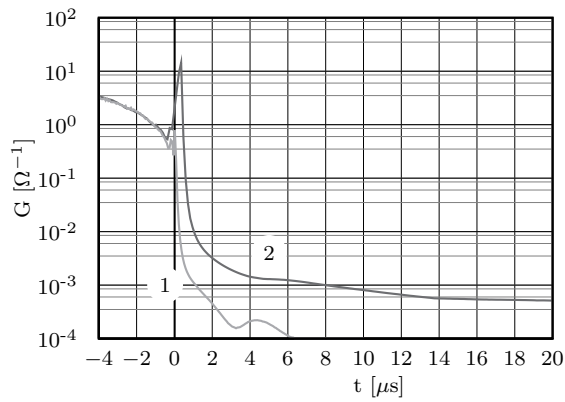


**Figure 4.7:** Post-arc conductance of the recordings of 1: Figure 4.6c and 2: Figure 4.6b.



their inertia makes ions much slower than electrons (their masses differ about five orders of magnitude). As a result of the electron movement, a positively charged ion sheath builds up in front of the post-arc cathode. The time change of the electric field inside this sheath gives a displacement current, and hence, the sheath can be considered as a capacitance.

This mechanism also implies that the post-arc current, and hence its conductance, decays more rapidly when the rate of rise of the recovery voltage (RRRV) is higher, because then the depletion of electrons in the inter-electrode gap goes faster. Figure 4.8 supports this assumption. It shows the result of three measurements from Test Series 5, and it contains the same data as in Figure 3.8. In all three measurements, the short-circuit current was 53 kA<sub>peak</sub>, and the arcing time was 8.5 ms. As predicted, the highest post-arc current in Figure 4.8 (Trace 1) ceases first, whereas the lowest post-arc current (Trace 3) ceases last.

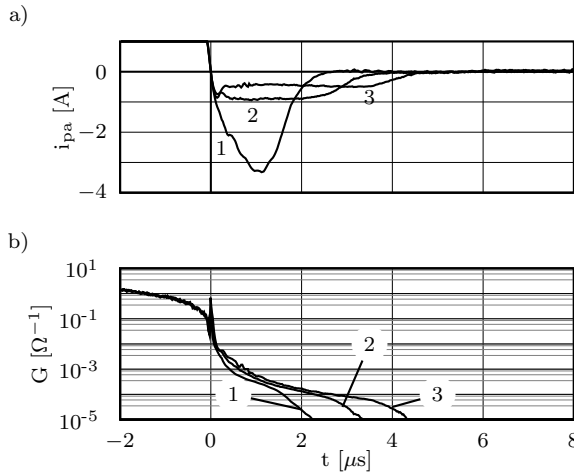


**Figure 4.8:** a) Post-arc current and b) post-arc conductance of three measurements from Test Series 5. Trace 1: RRRV=15 kV/μs, Trace 2: RRRV=6 kV/μs and Trace 3: RRRV=4 kV/μs.

As in Figure 4.7, Figure 4.8 shows again that the arc's conduction (before current zero) is the same in all three measurements, but it also shows striking similarities in the first 1.5 μs after current zero. This indicates that until this instant, the influence of the TRV on the post-arc conductance is weak. In fact, the post-arc conductance seems to be predetermined until a certain time after current zero. If this is true, it makes the analysis of measurements with different TRV's possible, not only when this difference is caused by a different electrical circuit, but also when there is interaction between the circuit and the post-arc current, such as in Figure 4.6.

As the conductance seems to depend weakly on the electrical post-arc activities, this might be a more suitable signal for researching trends than the post-arc current's

peak value. The following analysis uses  $G_t$  for a test to indicate its conductance at  $t$   $\mu$ s after current zero. In most of the tests,  $G_{0.5}$  is the instant at which the TRV has just started to rise, and its influence on the conductance is low. Moreover, since the TRV is normally several hundreds of Volts at this instant, and the post-arc current reaches its maximum value, the calculated conductance (which is  $i_{pa}/\text{TRV}$ ) is less sensitive to noise from the voltage signal.

Figure 4.9 compares the peak short-circuit current with  $G_{0.5}$  from tests from Test Series 5, the same as those used for Figure 4.3. Again, this relationship does not indicate an explicit function between the arcing and post-arc conditions.  $G_t$  rises gently with rising  $\hat{I}_{arc}$ , but extrapolating the trend towards  $\hat{I}_{arc} = 0$  yields a non-zero value for  $G_t$ . A possible explanation for this is equivalent to the conclusion for Figure 4.3, i.e. the tests were obtained in a synthetic circuit, of which  $di/dt$  at current zero is independent from the main short-circuit current. However, another explanation involves the non-linearity of  $G_t$ . More on this is described in Section 4.3.

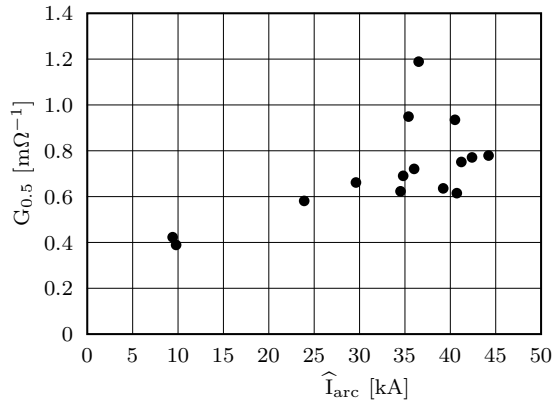
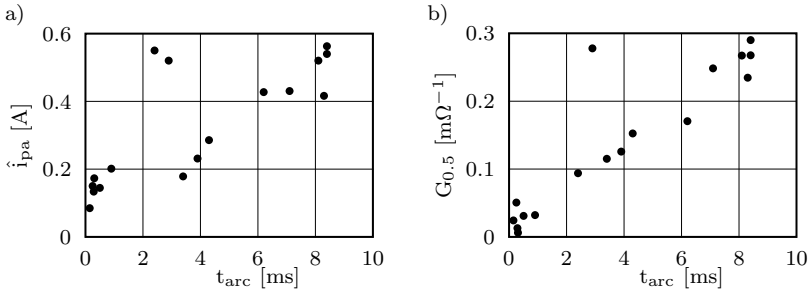


**Figure 4.9:** The post-arc conductance at 0.5  $\mu$ s after current zero versus the peak short-circuit current. The data is from Test Series 5.

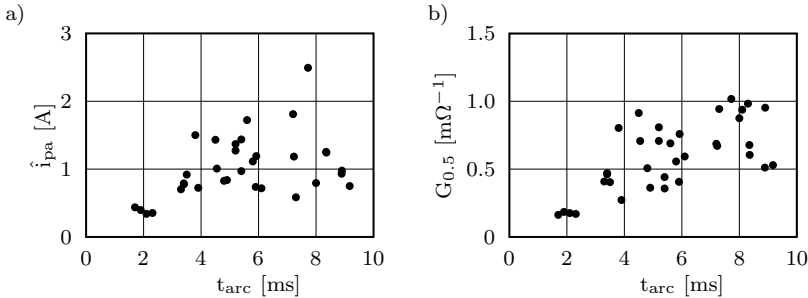
Most of the measurements in this research were performed with a fixed, high short-circuit current, whereas the arcing time was varied, with the intention to search for the breaker's interruption limit. As a result, this research lacks sufficient data for drawing reliable conclusions from graphs like Figures 4.3 and 4.9. Substantially more data was obtained from the tests with different arcing time and a fixed short-circuit current, and therefore, the research continues with analysing the post-arc conditions in relation to  $t_{arc}$ .

Figure 4.10 shows a significant improvement of the relationship between post-arc conditions and arcing conditions. The relationship between  $G_t$  and  $t_{arc}$ , Figure 4.10b, shows a much more distinctive trend than the relationship between  $\hat{i}_{pa}$  and  $t_{arc}$ , Figure 4.10a. The data in this figure is from Test Series 1, with  $\hat{I}_{arc}$  fixed at 20 kA.

Figure 4.11 shows the same relationships as 4.10, but these results are from Test Series 2. This figure shows improvement in the trend between arcing and post-arc conditions as well, however, it is less spectacular than the improvement shown in Figure 4.10.



**Figure 4.10:** a) The post-arc current's peak value and b) the post-arc's conductance  $0.5 \mu s$  after current zero, plotted against the arcing time. The data is from Test Series 1.



**Figure 4.11:** a) The post-arc current's peak value and b) the post-arc's conductance  $0.5 \mu s$  after current zero, plotted against the arcing time. The data is from Test Series 2.

Since it takes time for the arc to expand in the inter-electrode gap, the amount of plasma that is distributed across the gap at current zero increases with increasing arcing time. Moreover, when the arc lasts longer (longer  $t_{arc}$ ), it can produce more charge. These processes increase the conductivity, as Figures 4.10 and 4.11 demonstrate.

However, the post-arc research should not only be focussed at the post-arc conductance. The sheath growth that results in the post-arc current, as described in

Section 2.4, implies that the breaker's post-arc electrical behaviour is capacitive as well. Analysis of the post-arc capacitance requires the determination of the TRV's time-derivative, which is a problem when the TRV has been measured with a low signal to noise ratio. For example, the equipment that measured the signals in Figure 3.23b is unsuitable for such research. Test Series 1 and 2 have been recorded by the equipment that measured the signals in Figure 3.23a. This figure shows a smooth  $d\text{TRV}/dt$ , and therefore, these series are suitable in this case.

Figure 4.12 shows  $C_{0.5}$ , which is the post-arc capacitance at  $0.5 \mu\text{s}$  after current zero (calculated with  $i_{pa}/(d\text{TRV}/dt)$ ), plotted against the arcing time. Only Test Series 2 (Figure 4.12b) shows an improvement in the arc - post-arc relation compared to other research performed on this series, whereas Figure 4.12a shows more scatter in its trend, compared to, e.g. Figure 4.10a. Note that these results have been obtained from data from which the influence of the physical capacitance of the breaker has been numerically removed with the process described in Section 3.4.

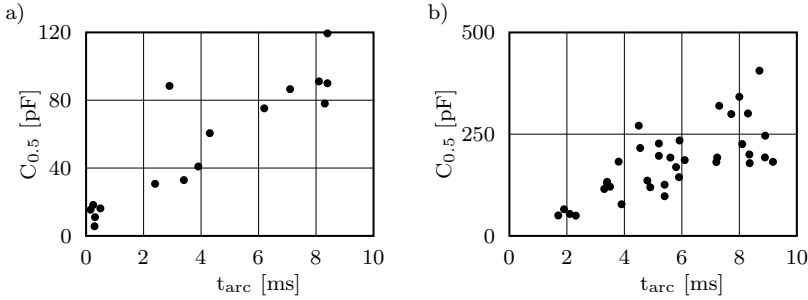


**Figure 4.12:** The post-arc capacitance at  $0.5 \mu\text{s}$  after current zero versus the arcing time. a) Data from Test Series 1, b) data from Test Series 2.

So far, the TO's post-arc properties have been compared at a fixed time after current zero, but it is also interesting to observe the instant in which a specific parameter value has been reached. This is, for example, the instant when the post-arc current ceases, or when the post-arc conductance drops below a given value.

Figure 4.13 shows the time at which the post-arc conductance drops below  $0.1 \text{ m}\Omega^{-1}$  (denoted as  $t_{0.1}$ ), plotted against the arcing time. Again, the relationship seems to be quite explicit, however, both graphs show a more complicated relationship compared to  $G_t$  versus  $t_{arc}$ . This relationship follows an increasing linear trend, but seems to cross the  $t_{0.1}$  axis at a non-zero point. In fact, this relationship is not linear at all due to the non-linear time behaviour of the post-arc conductance, as becomes clear in the following section.

Figures 4.10b and 4.11b, as well as Figures 4.12a and b and Figures 4.13a and b show equal analysis performed on different breakers. Such analysis would be suitable for analysing the different performance of breakers. For example, Figure 4.13 shows that breaker B clears the post-arc current sooner than breaker A1. By intuition, this

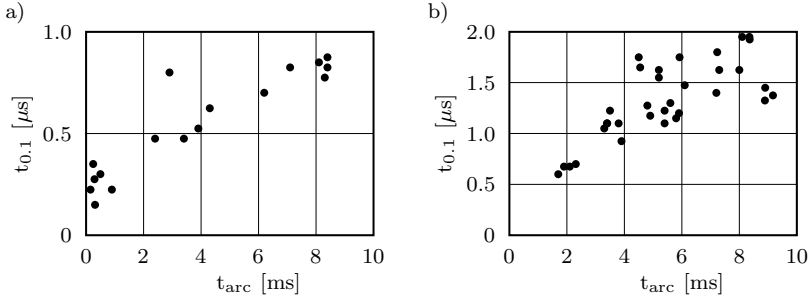


**Figure 4.13:** The time at which the post-arc conductance drops below  $0.1 \text{ m}\Omega^{-1}$  versus the arcing time. a) Data from Test Series 1, b) data from Test Series 2.

leads to the conclusion that breaker B performs better than breaker A1, because it seems to recover from the arc more quickly. However, these results are obtained from completely different test circuits, and Table 4.2 shows that in the mentioned example, A1 has been subjected to much higher currents and RRRVs. The following section and Chapter 5 elaborate further on the difficulty of comparing the different test series.

### 4.3 Post-arc properties compared with each other

So far, the analysis has focussed on finding a relationship between arcing and post-arc conditions. It showed that  $G_t$  holds the most distinctive relationship with  $t_{arc}$ , but it still contains a significant scatter. The analysis with  $C_t$  also leads to good results, but this requires a particularly low level of noise on the measured TRV, which is not always accomplished. The following analysis aims at finding relationships between the different aspects in the post-arc phase only (e.g.  $G_t$  and  $Q_{pa}$ ).

Figure 4.8 in Section 4.2 shows that in equivalent tests, the electrical post-arc events are equal in the first few microseconds after current zero. Equivalent tests in this context imply that the conditions inside the breaker are equal, i.e. not only the distance between the contacts, but also the plasma properties, the temperature of the contacts and other properties. The weak relationship between arcing and post-arc conditions, as observed in Section 4.2 indicates that such similar tests cannot be reproduced intentionally by presetting the arcing time and the short-circuit current, but they can only be discovered after a series of tests.

By simply looking at the shape of the post-arc-current in different tests, and by illustrating the plasma's behaviour after current zero, it can indeed be expected that the electrical behaviour acts in a pre-determined way. In the absence of a TRV (in other words, in the absence of a post-arc current), the charged particles between the contacts diffuse out of the inter-electrode gap, into the vacuum and they recombine

either with each other, or at the walls of the vacuum chamber. The TRV accelerates the rate of charge decay, since it attracts charge to the contacts. As a result, the rate of charge decay can be partly controlled by adjusting the TRV, as Figure 4.14 demonstrates.

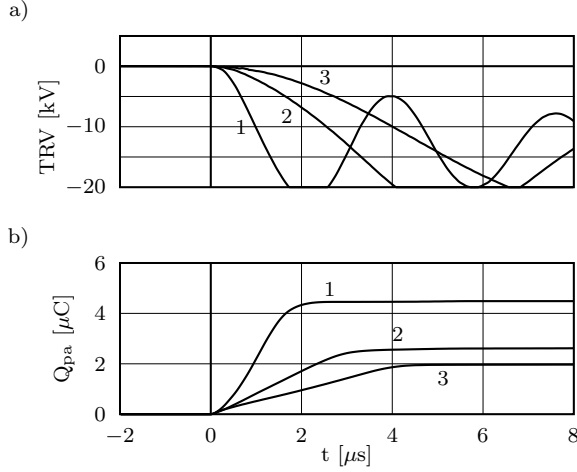


**Figure 4.14:** a) the TRV and b) the cumulative post-arc charge of three measurements from Test Series 5. These are the same results as those used in Figure 4.8

Figure 4.14b shows the time integrated post-arc current traces of Figure 4.8a. This figure shows that a higher RRRV attracts more charge from the inter-electrode gap before it recombines, hence the charge collected by the circuit reaches a higher value than it does in the case of a lower RRRV. Moreover, since the inter-electrode charge at current zero is limited, a high RRRV depletes the gap from charge earlier than a low RRRV. Figure 4.14 exhibits both effects.

The charge in Figure 4.14 reflects the amount of collected electrons, but not the amount of collected ions. Section 2.4 explained that as soon as the TRV starts to rise, a space charge sheath develops in front of the cathode. Consequently, the current through the cathode consists of an ion current and a displacement current, resulting from the time-change of the electric field inside this sheath. The plasma in front of the anode remains practically neutral during the post-arc current, therefore, only electrons carry the current through it. Since the circuit requires that the current through the cathode is equal to the current flowing through the anode, the ion current should be *smaller* than the electron current, since

$$i_e = i_i + C_s \frac{du}{dt}, \quad (4.1)$$

where  $i_e$  and  $i_i$  are the electron and ion current, respectively, and  $C_s$  is the sheath's capacitance.

If the breaker's conductance after current zero is small, little charge can flow through the breaker, whereas the opposite is true for a high post-arc conductance. As a result, the post-arc charge is proportional to the post-arc conductance, which the results in Figure 4.15 clearly demonstrate. Although the results in this figure are from measurement with different arcing times, they closely follow a distinctive trend.

Figure 4.14 already showed that the amount of collected charge increases with an increasing RRRV, whereas Figure 4.8 showed that  $G_t$  in the first microsecond after current zero remains unaffected by it. As a result, the coefficient of  $G_t$  versus  $Q_{pa}$  also depends on the RRRV, as is demonstrated in Figure 4.16.

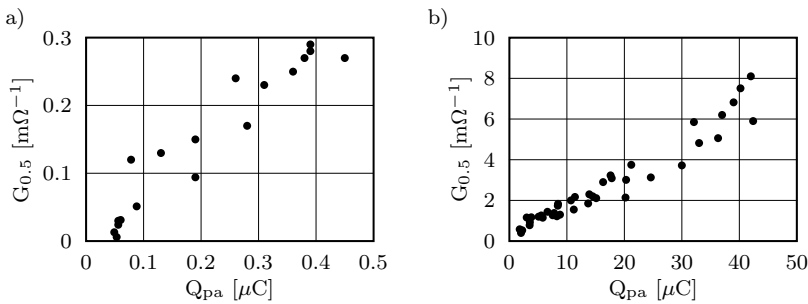


**Figure 4.15:** The conductance at 0.5  $\mu\text{s}$  after current zero versus the post-arc charge. a) Data from Test Series 1 and b) data from Test Series 4.

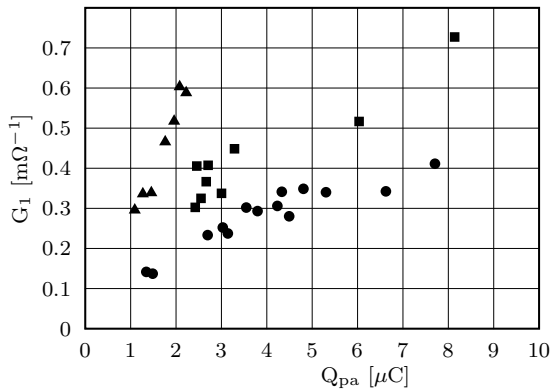


**Figure 4.16:** The conductance at 1  $\mu\text{s}$  after current zero versus the post-arc charge. The data is from Test Series 5. Triangle:  $du/dt = 4 \text{ kV}/\mu\text{s}$ , square:  $du/dt = 6 \text{ kV}/\mu\text{s}$ , circle:  $du/dt = 15 \text{ kV}/\mu\text{s}$ .

Despite the non-linear behaviour of the post-arc conductance, the trends in Figures 4.15 and 4.16 are remarkably straight and coherent. This is quite different when the time at which the conductance becomes less than  $0.1 \text{ m}\Omega^{-1}$  is compared with  $Q_{pa}$  (see Figure 4.17). These trends are also straight, but they suggest that when  $Q_{pa}$  approaches zero, the conductance still requires some time to decay. However, if the breaker conducts, it carries a current, which is contradictory to the observation that the total amount of charge is zero.

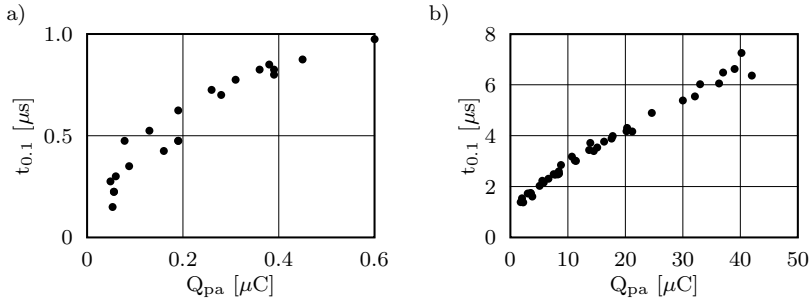


**Figure 4.17:** The time at which the post-arc conductance drops below  $0.1 \text{ m}\Omega^{-1}$  versus the post-arc charge. a) Data from Test Series 1, b) data from Test Series 4.

In fact, the trends in Figure 4.17 do not follow a straight line, but they obey a function that does cross zero. This is clarified with a simplified approximation to the conductance, given in Appendix C, together with a simplified approximation to the TRV, described in the same appendix. Despite the simplicity of this model, its results match the measured data quite well, as Figure 4.18 demonstrates.

These results are of course particularly useful for the development of a post-arc model in Chapter 6.

## 4.4 Voltage-zero period during current commutation

The post-arc conductance measured in, e.g. Figures 4.7 and 4.8, frequently shows a peak immediately after current zero before decreasing towards zero. The real conductance during this peak is difficult to determine from this data, since the voltage in this period has values close to the measuring system's thermal noise. This *voltage-zero* phenomenon has been mentioned earlier in Section 3.4, Figure 3.27b, where it leads to difficulties in determining the current's offset in the case of a re-ignition. It has also been measured before [51], but so far it has never been properly explained.

Other phenomena of the post-arc current can be explained with the model described in Section 2.4, but the voltage-zero in the first phase remains a problem. If



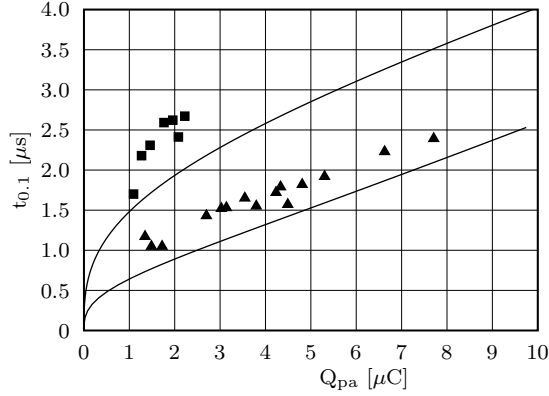


**Figure 4.18:** The time at which the post-arc conductance drops below  $0.1 \text{ m}\Omega^{-1}$  versus the post-arc charge. The data is from Tests Series 5. Triangle:  $du/dt = 15 \text{ kV}/\mu\text{s}$ , square:  $du/dt = 4 \text{ kV}/\mu\text{s}$ . The lines are the result of simulations with the model from Appendix C.

ions and electrons are indeed moving towards the post-arc cathode in this phase, they leave an empty gap behind between the plasma and the new anode. By definition of the model, charge sources are absent after current zero, hence no charge leaves the post-arc anode to fill up this gap. This implies breaking the electrical connection between the plasma and the anode, and hence, a voltage should rise across this gap. However, measurements such as the one in Figure 4.19 clearly shows a voltage-zero phase immediately following current zero. This is why the model should be complemented with an additional theory.

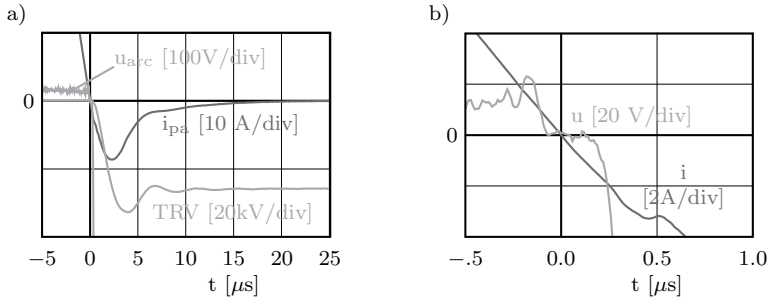


**Figure 4.19:** A typical example of the voltage-zero period.

An explanation for the voltage-zero period is found when the thermal velocity of the particles is taken into account. In that case, the pressure of electrons and ions causes the plasma to remain neutral in the voltage-zero phase. The breaker's electrical behaviour then resembles that of a double Langmuir probe, the relationship

of which between the current and voltage is known [52, 53, 54]. This facilitates the description for the voltage-zero period. For the application of this theory to the VCB, we start with a series of assumptions, some of which do not immediately apply to the actual situation.

First, consider the configuration of Figure 4.20. The electrodes are large, and placed closely together, so we assume that the inter-electrode properties only change in the direction perpendicular to them. This limits the problem to one dimension. We assume further that the plasma is stationary and equally distributed along the gap, and that all particles reaching an electrode are absorbed by it. The electron temperature is higher than the ion temperature, no collisions take place between particles in either the plasma or the sheaths and finally, no new plasma is generated. The process of events following current zero is illustrated in Figure 4.21.

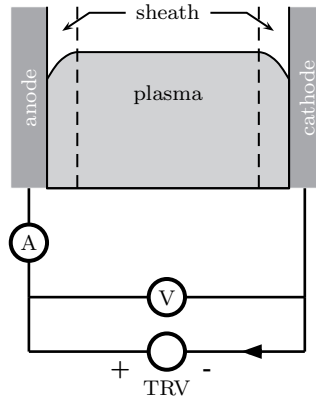


**Figure 4.20:** Configuration of the post-arc current model.

At  $t = 0$ , both the voltage across the gap and the current through the circuit are zero. Since their thermal energy is higher and their mass is lower, electrons have a higher thermal velocity than ions. Because of this, the flux of electrons at an electrode would be larger than the flux of ions, which would result in an electrical current. However, since both electrodes experience the same flux in opposite direction, the current remains zero. An electric field in front of the electrodes repels the surplus of electrons to ensure that the net charge flux through the contacts remains zero. This means that there is a potential difference between the plasma and the electrodes, which is mainly distributed across a small ionic space-charge sheath in front of the electrodes (see Figure 4.21a).

When the TRV starts to rise, the electric field in front of the cathode increases and repels more electrons. However, due to their temperature, a large amount of electrons can cross the electric field to reach the cathode. The change of the flux of charged particles at the contacts makes an electrical current possible, but

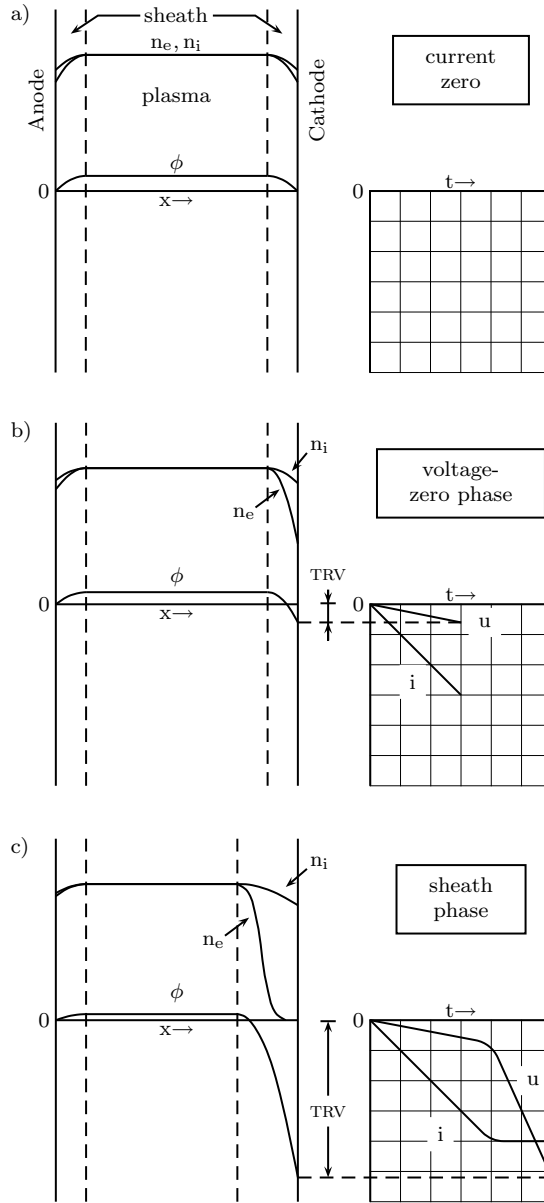


**Figure 4.21:** An illustrative example of the events following current zero.  $n_i$ ,  $n_e$  are the ion density and the electron density, respectively and  $\phi$  is the potential inside the gap. a) the situation at  $t = 0$ , b) the situation during the voltage-zero period and c) the situation after ion-current saturation.

because an abundance of electrons is still present in the cathodic sheath, the gap is still quasi-neutral, and as a result of its high conductance, the voltage across the gap remains low (Figure 4.21b). Here, the relationship between the voltage and the current is mainly determined by the plasma's conductivity. In the post-arc current measurements, the voltage in this phase remains below the noise level of the measuring equipment.

As the TRV continues to increase, the electric field in front of the cathode repels more electrons, until eventually, it becomes too strong for any electron to reach the cathode. At this point, the current is limited to the flux of ions reaching the cathode (Figure 4.21c), and an increase in voltage would only lead to an increase of the cathodic sheath width in front of the cathode, whereas the *ion saturation current* remains constant. As a result, the relation between the current and voltage now resemble a current-source.

The rise of the recovery voltage entails a fast time-change in the electric field inside the ionic space-charge sheath in front of the cathode. This entails a displacement current, which has to be added to the ion saturation current. Chapter 6 further elaborates on this, with the aid of a numerical model.

## 4.5 Conclusions

This chapter analysed the results obtained with the measuring techniques described in Chapter 3. It analyses the individual measurements, as well as various relationships such as those between the pre-zero parameters and post-arc current properties. Moreover, it formulates a theory for explaining the observed 'voltage-zero' period that immediately follows current zero, which is best observed in measurements with a high post-arc current. This theory is based on the theory of Langmuir probes, which incorporates the thermal behaviour of charged particles in a plasma, and their interaction with a conducting wall.

Although the post-arc current is the most distinctive electrical feature of current quenching with vacuum circuit breakers, it lacks a prominent relationship with the arcing conditions. Various mechanisms cause the scatter in this relationship, one of which is elaborated on in Section 2.4. Despite the large amount of scatter in the results, the following trends can be observed in the relationship between pre-zero and post-zero properties:

1. The post-arc current's peak value  $\hat{i}_{pa}$  is proportional to the arcing time  $t_{arc}$  (Figures 4.3a and 4.4a).

The arcing time has two effects on the post-arc parameters: first, the inter-electrode space increases with the arcing time, allowing it to contain more charge. Second, the arc burns longer, and due to the sinusoidal wave-shape of the current, more intensely at longer arcing time, thereby generating more charge. Both effects result in a higher post-arc current.

2. The post-arc charge  $Q_{pa}$  is proportional to  $t_{arc}$  (Figures 4.3b and 4.4b).  $Q_{pa}$  is the time-integrated post-arc current, and as such, it is proportional to it. Therefore, the explanation of conclusion 1. applies to this relationship as well.

3. The post-arc current decreases the rate of rise of recovery voltage, the RRRV (Figure 4.6 and Section 4.4).

Both the nature of a plasma, and the post-arc - circuit interaction cause this effect. Whether or not this is beneficial for the interruption process is discussed in Chapter 5.

4. Up to a given time  $t$  after current zero, the post-arc conductance  $G(t)$  is independent of the RRRV (Figure 4.8).

This observation can partly be explained with the theory from Section 4.4, i.e. it is inherent to the plasma properties, and the post-arc - circuit interaction.

5. The post-arc conductance at a given time  $t$ ,  $G_t$  is proportional to  $t_{arc}$  (Figures 4.10b and 4.11b).

This observation can be explained with Observations 2 and 8.

6. The time at which the post-arc conductance reaches a given value  $G$ ,  $t_G$  is proportional to  $t_{arc}$  (Figure 4.13).

This observation can be explained with Observations 2 and 10.

Contrary to the weak relationship between the test settings (arcing conditions) and the post-arc current, the relationship between various parameters of the post-arc current itself are quite distinctive. Based on the analysis in this chapter, the following conclusions can be drawn about the post-arc parameters:

7.  $Q_{pa}$  is proportional to the RRRV, and the duration of the post-arc current is inversely proportional to the RRRV (Figure 4.14).

The primary post-arc charge decay processes are diffusion and recombination. A high RRRV extracts much charge from the gap, but this process also adds to the depletion of charge. As such, it reduces the duration of the post-arc current. A low RRRV extracts less charge from the gap, thereby reducing its decay and allowing the post-arc current to flow for a longer time. However, in this case, more charge decays as the result of diffusion and recombination, which results in a lower measured  $Q_{pa}$ .

8.  $G_t$  is proportional to  $Q_{pa}$  (Figure 4.15).

More charge in the inter-electrode space allows more current to flow through it, which results in a higher conductance.

9. The coefficient in the relationship  $G_t = f(Q_{pa})$  is inversely proportional to the RRRV (Figure 4.16).

This is to be expected from earlier Observations 4 and 7, which state that  $G_t$  is independent of the RRRV for small a  $t$ , but  $Q_{pa}$  is proportional to the RRRV.

10.  $t_G$  is proportional to  $Q_{pa}$  (Figure 4.18).

This means that it takes time to remove charge from the gap.

A number of results presented in this chapter show equal analysis performed on different breakers. For example, Figure 4.13 shows the relationship between  $tG$  and  $t_{arc}$ . From this figure, it is tempting to assume that Test Object B performs better than Test Object A1, because the first clears the post-arc current earlier. However, from Table 4.2 and the details of these test series explained in Section 4.1, it is clear that these breakers have been tested under completely different conditions. This is also true for the other test series, which makes them unsuitable for comparing and ranking the test objects.

# Chapter 5

## Reignition analysis

### 5.1 Introduction

Section 2.5 summarised the physics on dielectric and thermal reignition in vacuum known today. This theory resulted from investigation on test objects that were specially prepared, so that they could observe the breakdown process directly, e.g. with optical investigation on the inter-electrode region, or with devices that measure the test object's internal vapour pressure (or the particle density and energy).

It would greatly benefit this investigation, if such information could be obtained from electrical signals only, because then it would be possible to investigate commercially available breakers, which are sealed for life, for all relevant characteristics. This chapter continues the analysis on the measured data from Chapter 4, but focusses on the reignitions.

Section 5.2 analyses thermal reignitions, which, according to our definition of it described in Section 2.5, occur during the post-arc current. Section 5.3 analyses the reignitions that we classify as dielectric. The conclusions from these two sections are extrapolated to standardised SLF tests in Section 5.5, with the aim to validate the relevance of Amendment 2 of IEC standard 62271-100. Section 5.6 summarises the conclusions from this chapter.

## 5.2 Thermal reignitions

If a reignition is Townsend-like, i.e. it results from an electron avalanche in a gas, the breakdown voltage  $U_{BD}$  can in principle be determined from the vapour pressure  $p$  between the contacts, and the contact separation  $d$ . When  $U_{BD}$  is plotted against  $pd$ , it should follow the trace depicted in the second region of Figure 2.10. The breakdown voltage has been measured directly in this research. The contact separation is a careful approximation, based on the arcing time, but the vapour pressure is more difficult to estimate. The following theory describes a way to estimate it from the measured electrical signals.

All the material in the gap exist primarily from cathode spot activity. Vapour particles are either generated directly by a cathode spot, or indirectly by vaporisation from the anode, heated by incident particles from the cathode. If after current zero, the amount of vapour relates to the amount of charge, then the post-arc charge  $Q_{pa}$ , which is the time-integral of the post-arc current, might be an indicator for the amount of neutral vapour at current zero. However, it is impossible to determine  $Q_{pa}$  when a reignition takes place during the post-arc current, since the determination of  $Q_{pa}$  requires the entire post-arc current.

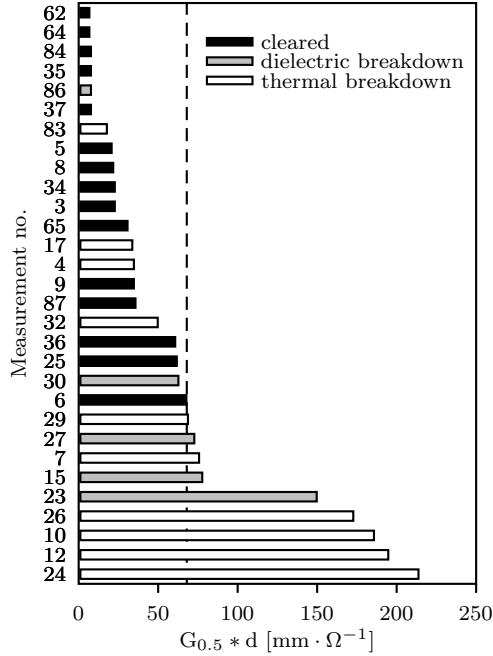
Section 4.3 showed that  $Q_{pa}$  relates rather linear to  $G_t$ , the conductance at  $t$  microseconds after current zero, and that its coefficient changes only due to the TRV settings (see Figures 4.15 and 4.16). In the first microsecond after current zero, the TRV is normally still low, and probably for this reason, the gap hardly ever reignites during this time. As a result, it is always possible to measure  $G_t$  within the first microsecond, and with the fixed coefficient, it is possible to determine  $Q_{pa}$ , even if the gap reignited during a post-arc current. Therefore, instead of using  $pd$  to investigate its relationship with  $U_{BD}$ , the following analysis uses  $G_t d$ , where  $d$  is determined by multiplying the arcing time with a contact opening velocity of 1 m/s.

Figure 5.1 shows  $G_{0.5}d$  of 30 measurements from Test Series 2 with equal TRV settings. It shows a smooth transition from values of  $G_{0.5}d$  for which thermal reignition is rare to values for which thermal reignition occurs more frequently. Beyond  $G_{0.5}d \approx 70 \text{ mm} \cdot \Omega^{-1}$  (indicated in Figure 5.1 with the dashed line) the test object always fails.

If it is true that  $G_{0.5}$  relates to the pressure  $p$ , and that the thermal failures in the measurements of Figure 5.1 are caused by Townsend breakdown, then plotting  $U_{BD}$  against  $G_{0.5}d$  should result in a Paschen-like curve. This is done in Figure 5.2a, from which it is obvious that it does not look like a Paschen curve, nor does the relation between  $G_{0.5}d$  and the time after current zero at which the breakdown happened show a trend, as Figure 5.2b demonstrates. The latter figure could also be an indicator for Townsend type breakdown, since the breakdown delay time decreases with increasing pressure [55].

Based on the observations described above, it is unlikely that the reignitions occurred as the result of a Townsend mechanism. Moreover, Paschen curves are





**Figure 5.1:** The conductivity at  $0.5 \mu s$  after current zero multiplied by the contact separation of 30 measurements. The results are ordered in increasing values to facilitate the search for a breakdown trend.

measured from stationary gasses and steady voltages. This is in great contrast with the post-arc conditions in a VCB, where the plasma and vapour are non-uniformly distributed in the gap, and the voltage shows high-frequency oscillations. This sometimes leads to the odd situation that the breakdown occurs at a voltage that is lower than just an instant earlier, see for example Figure 5.3.

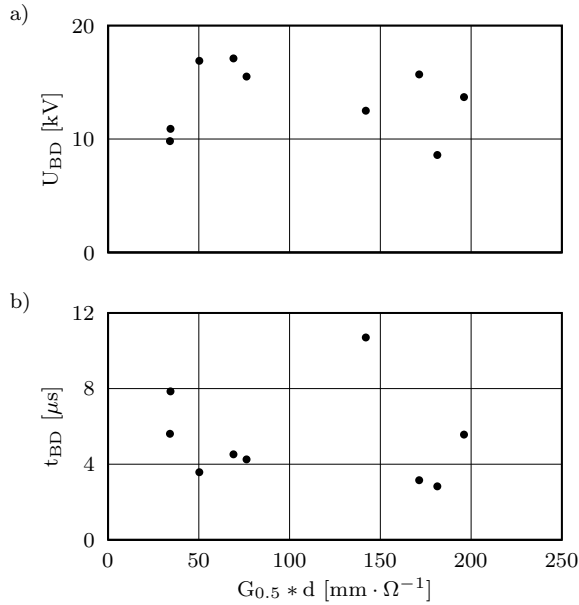


**Figure 5.2:** a) the reignition voltage and b) the reignition delay time after current zero versus the conductance at 0.5 μs after current zero, multiplied by the contact separation.

The lack of transparency in the observations does not immediately lead to the conclusion that the breakdown is not Townsend-like. The following analysis tries to find an answer to the question why Figure 5.1 does not show a threshold for  $G_t d$  below which the breakers always clears, and beyond which the breaker always fails.

First of all, as a consequence of its nature, the vacuum arc erodes the contacts of the breaker to provide itself with the required material to burn. After many arcing operations, the progressive erosion of the contact material causes the arc to reach the material on which the original contact material is mounted. When this happens, the vacuum conditions drop quite drastically and the breaker's current quenching ability suddenly decays. At that moment, the breaker has reached its technical end of life. This was probably the case for Measurements 83 and 86, which are near the top of Figure 5.1, in which the breaker failed even though  $G_t d$  was relatively low.

On the other hand, Measurement 87 (about halfway up in Figure 5.1) was also performed near the end of the test series, and it does have an increased  $G_{0.5} d$ , but it cleared nonetheless. The post-arc current of this measurement, shown in Figure 5.4b shows that it did struggle to hold the voltage, as it has small peaks on it, which are probably small non-sustained discharges. Measurement 36, depicted in Figure 5.4c, has an even higher  $G_{0.5} d$ , and it shows a more pronounced partial discharge. This result raises the question whether the reignition failed to complete

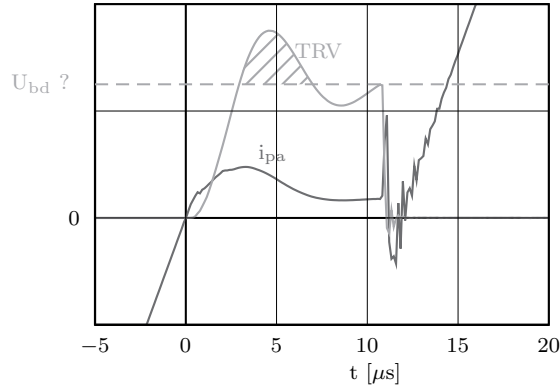


**Figure 5.3:** A reignition that takes place after the TRV reached its peak value. The TRV is 12.5 kV/div and  $i_{pa}$  is 25 A/div. Note that the current has an incorrect offset after the reignition due to clipping of the Rogowski output at the moment of reignition (see also Figure 3.27c).

due to the properties inside the breaker, or due to the circuit, since the increased current leads to a drop in the voltage. Figure 5.4c shows Measurement 34, which has a relatively low  $G_{0.5}d$  in Figure 5.1, but it nevertheless shows similar spikes in the post-arc current. It hardly influences the voltage, hence the non-sustainability of such spikes results probably from the conditions inside the breaker.

Similar events such as those in Figure 5.4 happened in Measurements 9, 25 and 6, which are depicted in Figures 5.5a, b and c respectively. According to Figure 5.1, their  $G_{0.5}d$  is in increasing order. Although it has not been observed for spikes, these measurements show a slowly increasing current in addition to the post-arc current, which eventually decays back to zero. In Figure 5.5a, this event starts even after the post-arc current has vanished, which is something that has not been observed for the spikes.

The breaker performs better when the TRV settings are relieved. See for example Figure 5.6, which compares Measurement 17 from Figure 5.1 with a test from Test series 3. These tests were performed on the same type of breaker, and it should be expected that they both perform in the same way. The  $G_{0.5}d$  of Measurement 17 is relatively low compared to the one in Figure 5.6b ( $38 \text{ mm} \cdot \Omega^{-1}$  and  $96 \text{ mm} \cdot \Omega^{-1}$ , respectively), however Measurement 17 reignites, and the measurement in Figure 5.6b does not. Therefore, the results from Test Series 3 cannot be added to the results of Figure 5.1.

So far, the analysis discussed the existence of an upper limit for  $G_t d$  as an indicator for the breaker's performance. A lower limit should also be expected, since a

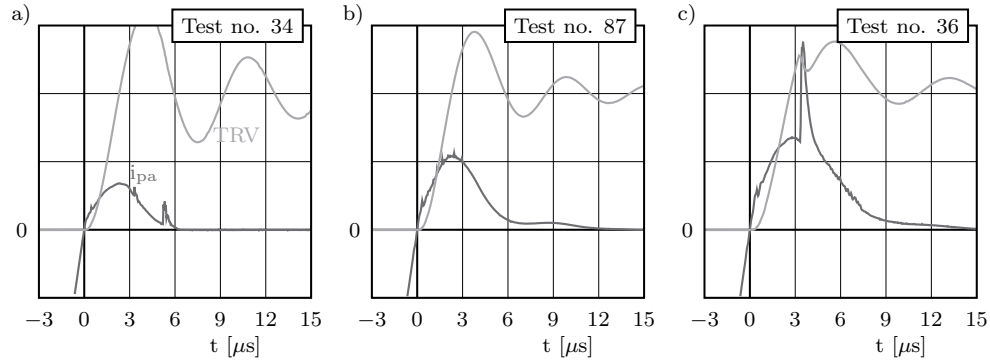


**Figure 5.4:** Fast non-sustained discharges in the post-arc current. The TRV is 6 kV/div,  $i_{pa}$  is 6 A/div and the test numbers refer to the tests in Figure 5.1.

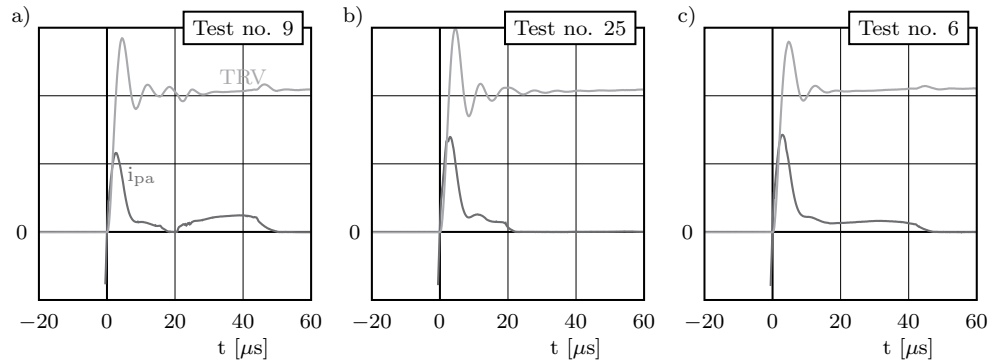


**Figure 5.5:** Slow non-sustained discharges during and after the post-arc current. The TRV is 6 kV/div,  $i_{pa}$  is 6 A/div and the test numbers refer to the tests in Figure 5.1.

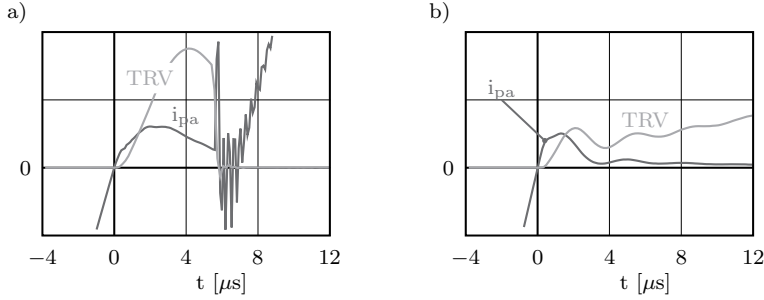


**Figure 5.6:** The TRV's influence on the reignition behaviour of the breaker.  $G_{0.5}d$  in a) is  $38 \text{ mm} \cdot \Omega^{-1}$  and in b) it is  $96 \text{ mm} \cdot \Omega^{-1}$ . In both figures, the TRV is  $10 \text{ kV/div}$  and  $i_{pa}$  is  $5 \text{ A/div}$ .

reignition is more likely to occur at a small contact distance  $d$ . This is indeed demonstrated in Figure 5.7, where  $G_{0.5}d$  is plotted on a logarithmic scale to conveniently display its large dynamic range. These results are from Test Series 6, which were measured in KEMA's SLF simulation circuit. Section 4.2 demonstrated that  $G_t$  is in general proportional to the short-circuit current. Contrary to the current-injection circuit of the Eindhoven laboratory, the TRV in this circuit increases proportionally to the short-circuit current (see Section 3.2.1). As a result, increasing the short-circuit current in this circuit does not only aggravate the reignition conditions by increasing  $G_t$ , but also by increasing the TRV.

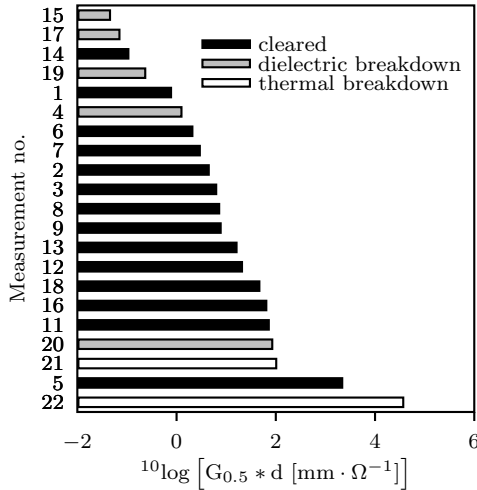


**Figure 5.7:** The conductance at  $0.5 \mu\text{s}$  after current zero multiplied by the contact separation of 30 measurements. The results are from Test Series 6.

### 5.3 Dielectric reignitions

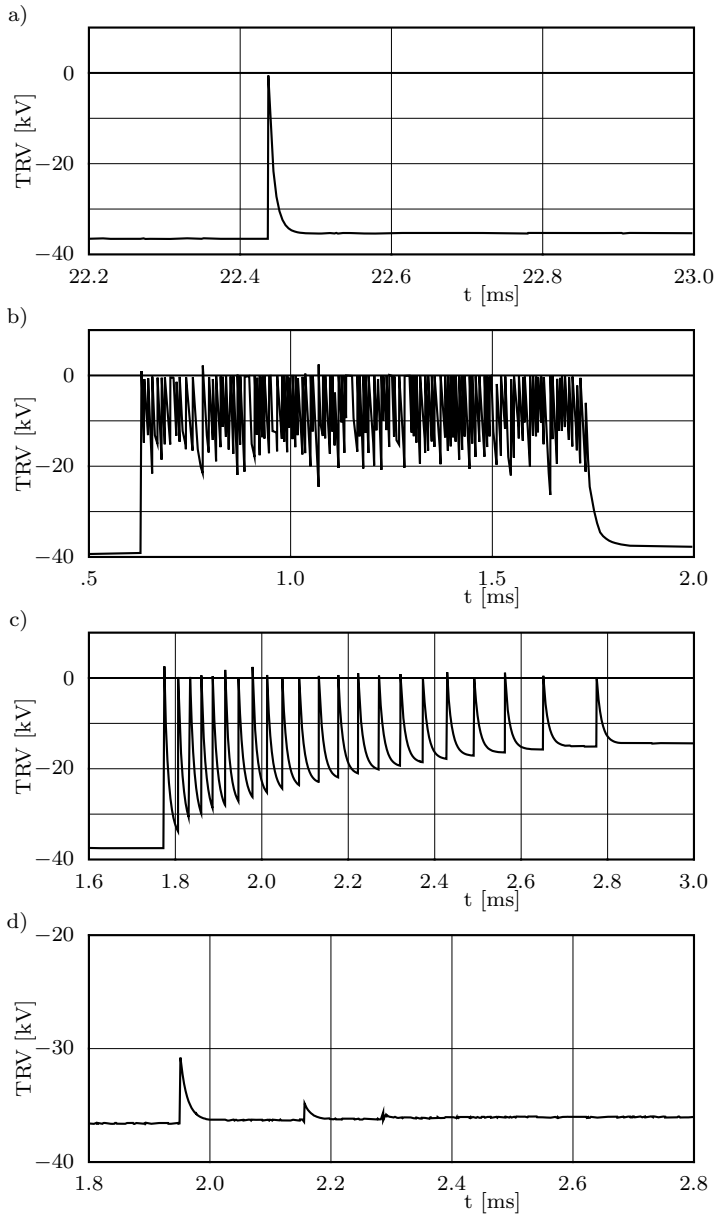
The voltage injection circuit described in Section 3.2.2, has been designed with the aim to generate current and voltage waves as illustrated in Figure 3.14. This circuit uses a much higher recovery voltage than the current injection circuit, and due to the nature of its high voltage, it might be possible to measure the theoretical 'warm recovery curve' (i.e. the increase of the breaker's breakdown voltage after arcing) of a vacuum circuit breaker. However, what really has been measured is shown in Figure 5.8. This figure shows four typical results from this circuit, and it demonstrates that the results are quite different from the expected results, such as Figure 3.14.

All the examples in Figure 5.8 (and all the other observed reignitions in Test Series 7 and 8) show that the breaker holds the recovery voltage for hundreds of microseconds to several milliseconds after current zero, before it collapses. It is known from Chapter 4 that the post-arc current decays within microseconds, which means that the reignitions observed in this circuit took place well outside 'thermal reignition' zone, and according to our definition of it, these results show dielectric breakdown. Section 2.5.1 gives more information on this.

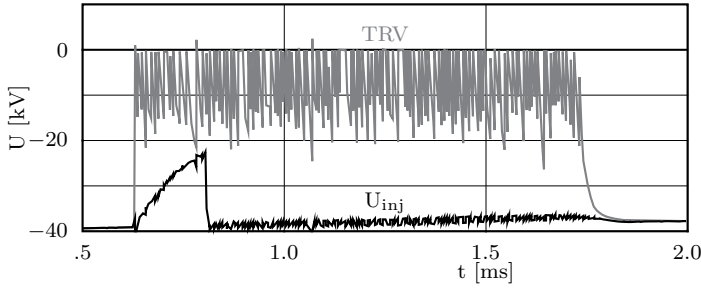
The maximum stationary current that the TRV section of the voltage injection circuit can supply is about 0.4 A (not taking into account possible high-frequency currents flowing through parasitic capacitances). This current is too small to maintain a stable vacuum arc, and as a result, the breaker interrupts any discharge almost immediately. The first example, Figure 5.8a, shows that after the reignition, the breaker fully recovers to withstand the (new) TRV. Because of this, it is difficult to say whether or not this discharge might have evolved into a vacuum arc, if the circuit had been able to sustain one.

Figure 5.8a also shows that after the reignition, the recovery voltage eventually reaches a lower value than before the reignition due to the loss of charge in capacitor  $C_{inj}$ . Contrary to this, the TRV in Figure 5.8b returns almost to its original value, despite the many discharges. Figure 5.9 displays the voltage across  $C_{inj}$  of this particular example, and it shows that at  $t \approx 0.8$  ms,  $C_{inj}$  suddenly charges to -40 kV again. This is caused by a breakdown of the triggered spark gap (SG), which reconnects  $C_{HV}$  to the circuit (see Figure B.1). In this way, the system is able to sustain the discharge in the TO much longer.

Figure 5.8c demonstrates that the VCB's breakdown voltage decreases after each reignition. The small amount of charge that is released after each breakdown apparently deteriorates the breaker's withstand voltage. Figure 5.10 shows the breakdown voltage and the supply voltage of this and three other measurements. In this figure, the breakdown-voltage-functions have been constructed by drawing straight lines between the measured breakdown voltages. Figures 5.10a-c illustrate that immediately after the first reignition, the breakdown voltage drops faster than the voltage drop of the supply voltage  $U_{inj}$  (which is the voltage across  $C_{inj}$ ). However, after many discharges, the supply voltage eventually drops below the breaker's breakdown



**Figure 5.8:** Examples of breakdown behaviour of VCB's in the voltage injection circuit. In all the examples, current zero is at  $t = 0$ .



**Figure 5.9:** Reignition of the spark gap at  $t = 0.8$  ms recharges capacitor  $C_{inj}$ .

voltage, and the circuit is unable to ignite the breaker any more.

The exponential shape of the breakdown-voltage-functions in Figure 5.10 can be explained as follows. The first reignition releases charge into the inter-electrode space of the VCB, which decreases the breakdown voltage. Had the circuit been able to do it, it might have sustained a new vacuum arc. However, the circuit is not, and the breaker interrupts the reignition almost immediately after it starts. Due to the decreased breakdown voltage, the next discharge takes place at a lower voltage, and as a result, this discharge releases less charge and vapour into the gap than the previous one. Together with the vapour from the previous reignition, the breakdown voltage decreases further. Because of the reduced supply voltage, the TRV rises slower after each reignition, which gives the gap more time to recover until eventually, the breaker stops reigniting at all.

The measurement of Figure 5.10d has been performed only four minutes after the previous one. Therefore, the breaker did not fully recover from the previous tests (i.e. the contacts were still hot), which possibly explains the capricious behaviour of the breakdown voltage function of this test.

The final example that is frequently observed in the tests involves the voltage behaviour, depicted in Figure 5.8d. Although the voltage shows discharges, the breaker recovers before the voltage has fully dropped to zero. Figure 5.11 shows the instant of the first non-sustained breakdown of Figure 5.8d in more detail. The most likely explanation for this event is that it has been caused by a discharge between the breaker's vapour shield and a contact. This involves the transfer of charge from the shield to the contacts (which leads to a current), and the release of secondary charge due to the impact of metal particles on the contacts. The limited amount of conducting material between the contacts of the breaker, and the reduced voltage across them prevents the breakdown to carry on.



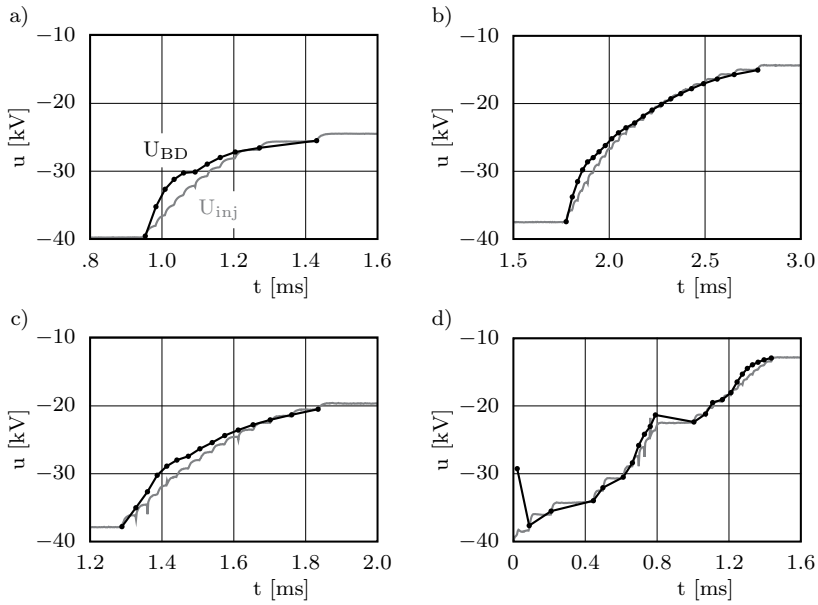


**Figure 5.10:** The VCB's breakdown voltage ( $U_{BD}$ ) and the supply voltage ( $U_{inj}$ ) of four measurements.

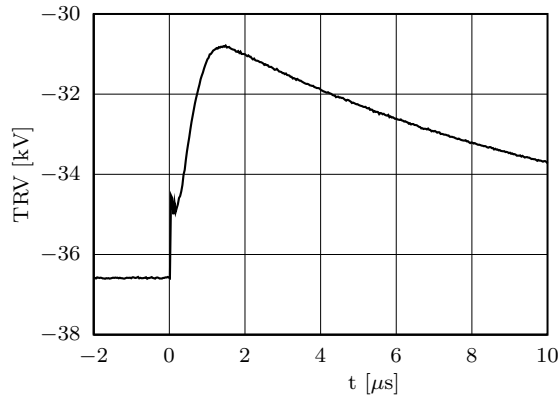


**Figure 5.11:** The instant of the first reignition in Figure 5.8d. First, the discharge develops with a steepness that is equivalent to other discharges, but as soon as the voltage reaches  $-35$  kV, the breakdown process slows down, until eventually, the breaker recovers.

## 5.4 Continuing post-arc current

When the test object in the voltage-injection circuit re-strikes, the high-ohmic resistor  $R_{inj}$  limits the current that flows through it to several tens of ampères. Since this current is too low for a stable vacuum arc, the breaker interrupts it almost instantly, which leads to the results that have been described in Section 5.3. The high Ohmic resistor  $R_{inj}$  adds value to the research in another way as well. The current through it, called  $i_{inj}$ , can easily be derived from the voltage across it, which makes it possible to measure tenths of milli ampères. Part of this current flows through the stray capacitance near the test object, and through the voltage probe that measures the TRV, but the remaining part flows through the test object. As long as the TRV changes slowly enough in time, the current through the stray capacitance becomes too small to measure, and  $i_{inj}$  then represents only the current through the test object and the voltage probe.

See, for example, Figure 5.12, which shows the results of two measurements from Test Series 8. The TRV in this test series was set to a maximum of 20 kV, and the Trace 1 of Figure 5.12 shows what happens to the TRV and  $i_{inj}$ , in the case that the test object was subjected to a lower current than its rated value. After its stabilisation, the TRV drops slowly back to zero, because the circuit's capacitances lose charge through the high Ohmic voltage probe that measures the TRV. This is also seen in  $i_{inj}$  of this trace, which has a non-zero value after current zero.

Trace 2 of this figure is from a measurement with a peak short-circuit current of 32 kA, which is higher than the test object's rated value (20 kA<sub>RMS</sub>). It shows great similarity with the results reported in [56]. The breaker's post-arc conductance does not allow the TRV to reach its maximum value, and it also decays faster than Trace 1 because of this reason (it also shows re-strikes in the first millisecond after current zero). Although the decay rate of the TRV of Trace 2 is faster than that of Trace 1, the rate is too slow to measure the current through the stray capacitance near the test object (which has a value of several tens of pF). Therefore, this is an example in which it is likely that  $i_{inj}$  observed here, also flew through the breaker. (Note that the dynamic range with which the current has been measured in a single test now exceeds more than seven orders of magnitude, i.e. from tens of kA to tenths of mA).

The post-arc currents described previously all flew through residual plasma. Since this plasma decays within microseconds, the post-arc current described in this section has to result from another principle, which depends on both the high temperature of the cathode, and the strong electric field.

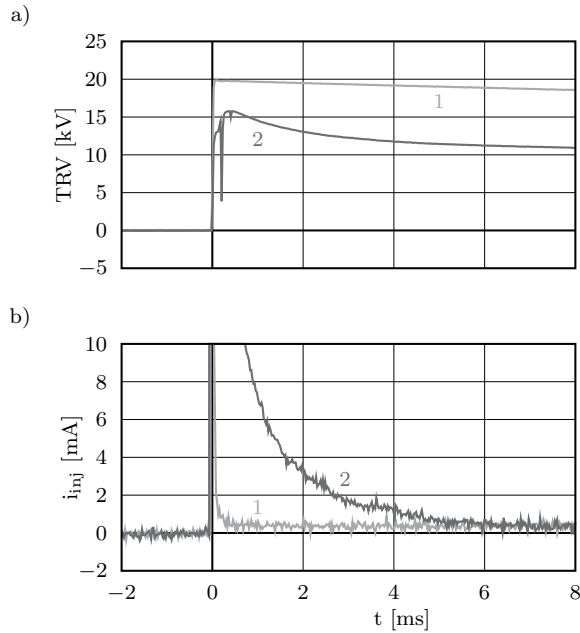


**Figure 5.12:** a) the TRV and b) the current  $i_{inj}$  of two measurements of Test Series 8. Trace 1 and 2 are measurements with a peak short-circuit current of 11 and 32 kA, respectively.

## 5.5 Amendment 2 of the IEC standard 62271-100

Since the approval of Amendment 2 of the IEC Standard 62271-100 [38], manufacturers are obliged to subject circuit breakers with a voltage rating of 15 kV and above, and a short-circuit current rating of 12.5 kA to Short-Line Fault (SLF) tests if the breakers are connected to an overhead line. Until then, this type of test was limited to switchgear with a voltage rating of 52 kV and above. This amendment predominantly applies to vacuum switchgear, since this is the most widely used switchgear in the voltage range of 15 kV to 52 kV.

As already described in Section 3.2.1, SLF tests are considered to be one of the most severe tests for gas circuit breakers. This is due to the steep rise of recovery voltage immediately after current zero, which puts a lot of strain on the cooling gas. The principle mechanism of vacuum arc extinction differs quite a lot from gas arc extinction, and this raises the question whether SLF tests are just as severe for VCB's as for gas circuit breakers.

Three test series in this research have been performed at KEMA in an SLF simulation circuit (Test Series 1, 3 and 6). The total number of tests in these series is small, and contain only a limited number of reignitions. Without further elaborating

on them, it can be concluded that these reignitions happened due to small arcing times, or excessively large short-circuit currents (including asymmetrical currents). Therefore, the next analysis focusses only on the tests performed in the synthetic circuits in Eindhoven.

The main difficulty for breakers to interrupt an SLF fault is to cope with the steep rise of recovery voltage. Although the synthetic circuits (both current-injection and voltage-injection) were not developed to simulate SLFs, their TRV steepness did exceed the requirements for SLF TRV's. Figure 5.13 shows the TRV requirements for terminal fault (TF) and SLF fault testing for a 20 kA, 24 kV breaker, according to the IEC standard. Also shown in this figure is one TRV measured in the current-injection circuit in which a 20 kA, 24 kV breaker has been researched (Breaker A1 in Test Series 4). Although the generated TRV does not reach the required maximum value (Figure 5.13a), it exceeds it in the first, critical microseconds after current zero (Figure 5.13b). This makes it plausible to assume that the measurements performed in this circuit can also be considered as SLF tests.

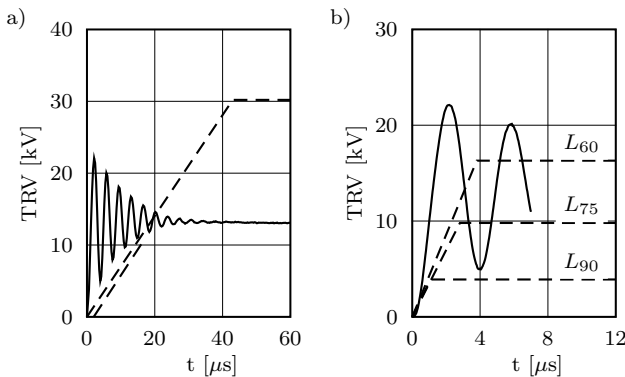


**Figure 5.13:** a) Solid line: TRV used in Test Series 4. Dashed line: Source side TRV requirements for an SLF test on a 24 kV breaker. b) Solid line: same as in a), dashed lines: Line-side TRV requirements according to the IEC amendment.

An SLF fault is expressed as a percentage, indicating the reduction of the short-circuit current, caused by the reactance of the overhead line (see Section 3.2.1). For example, according to the standard, a 75% line fault test on a 20 kA gives a short-circuit current of 15 kA. Many tests in Test Series 4 have been performed with a higher short-circuit current. Figure 5.14 shows the cumulative distribution of the short-circuit currents used in this series, rated to the required short-line fault current. It demonstrates that for SLF test requirements, the majority of the tests in Test Series 4 has been performed with a (much) higher short-circuit current. Nevertheless, all the 69 measurements shown in this figure cleared the current. When the analysis above is applied to other test series with this breaker, it leads to the same conclusions. Apparently, this type of breaker is well capable of managing the

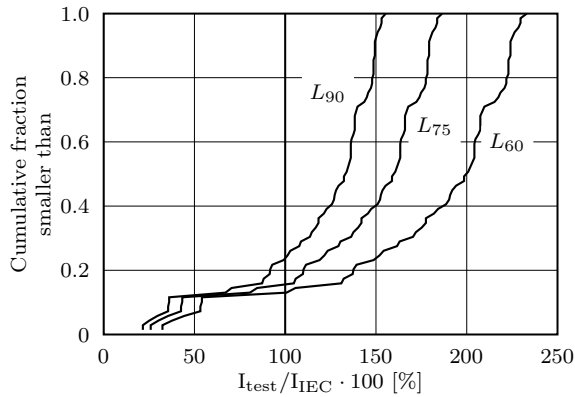


**Figure 5.14:** The short-circuit currents used in Test Series 4 compared with the required short-circuit currents for IEC SLF tests.

SLF TRV of SLF tests.

In this research, the Voltage Injection circuit has been used to analyse only Test Object B. This breaker has a voltage rating of 12 kV, and according to the amendment, it is not required to subject it to SLF testing. Nevertheless, the results from these measurements are still useful for analysing the performance of VCB's under SLF test conditions, since they were subjected to the steepest TRV's of this research, the results of which were presented in Section 5.3 (Dielectric reignitions). This particular section started with the observation that practically all reignitions occurred tens of microseconds after current zero, well after the voltage reaches its stationary value. Apparently, this breaker does not suffer at all from a steep rise of recovery voltage.

In conclusion, VCB's are well capable of managing a steep rise of recovery voltage, and subjecting them to short-line fault tests seems therefore not necessary. This is in contrast with gas circuit breakers, such as SF<sub>6</sub> breakers, for which the SLF is particularly difficult to cope with.

## 5.6 Conclusions

This chapter took a close look at the various reignitions observed in the measured data, and tried to find indicators in the electrical signals that announce an imminent reignition. The reignitions have been classified into two types: thermal reignitions, which happen during the post-arc current and dielectric reignitions, which occur afterwards.

Thermal reignitions are rare, and happen almost only when the arc current well exceeds the breaker's rated current, or when the breaker reaches the end of its technical life-time. Besides that, the electrical signals lack a distinctive indicator

from which a future thermal reignition can be predicted, although the product of the post-arc conduction at a given time ( $G_t$ ) and the contact distance ( $d$ , derived from the arcing time) gives reasonable results. It has been shown that when the value of this parameter is below a certain lower value, or when it is beyond a certain upper value, the breaker is likely to reignite. These values depend on the type of breaker and the TRV used in the test. Since all the test series had different properties, determining the upper and lower boundary for  $G_t d$  for each breaker used in this research is impossible. It should be mentioned that the relationship between  $G_t d$  and a thermal reignition exhibits scatter, just as in the relationship between the arcing properties and the post-arc properties, analysed in Chapter 4.

Dielectric reignition was more frequently observed, especially in the results from the voltage injection circuit, despite its intention to investigate thermal reignitions. This circuit generated a higher TRV with a steeper slope than the current injection circuit, and it ultimately demonstrated that the analysed VCBs did not suffer from the TRV steepness at all.

One of the intentions of this research was to apply thermal reignition indicator analysis, which has been done with success on SF<sub>6</sub> breakers in the past [36], to VCBs. This chapter concludes that thermal reignitions in VCBs are rare in the first place, which makes the intended purpose of this research unnecessary. Even if breakers are subjected to tests in which the values of the short-circuit current and recovery voltage exceed the breaker's rated values, and also to a much steeper rise of recovery voltage after current zero than required by the IEC standard, reignition occurs only rarely in the period immediately following current zero.

The recently approved Amendment 2 of IEC Standard 62271-100 [38] decreased the voltage rating for breakers that are obliged to be subjected to SLF tests, from 52 kV to 15 kV. Since VCBs are the most widely used breakers within this voltage range, this amendment mainly applies to these. From this chapter's conclusion that VCBs are well capable of managing a steep rise of recovery voltage (which is the main severity in SLF tests), it can be implicitly concluded that a VCB will pass SLF tests without any problem. Therefore, Amendment 2 of IEC Standard 62271-100 adds little value to prove the reliability of VCBs.

## Chapter 6

# Post-zero arc plasma decay modelling

### 6.1 Introduction

The ultimate goal of this research is to find performance indicators from short-circuit tests on VCBs that predicts their behaviour in different electrical networks. If such indicators exist, they will provide VCB manufacturers with additional information about the performance of their products from expensive and time-consuming short-circuit tests, which might help improving them. So far, the emphasis of this work laid on the analysis of the results from high quality current and voltage measurements at short-circuit tests. This analysis was in particular focussed on the post-arc current phase, since this is the most distinctive electric signal of the short-circuit test. This effort resulted in a better understanding of the current-quenching mechanism in vacuum.

Another way to investigate the performance of VCBs is by simulating their behaviour. This has been successfully done in the past with SF<sub>6</sub> breakers [57, 58, 59]. Compared to the complicated manner by which an SF<sub>6</sub> arc is extinguished, the models that simulate its interaction with the electrical circuit are relatively simple and easy to apply, and their results are sometimes surprisingly good.

This chapter describes the development of a model that simulates the interaction of a vacuum arc with an electrical circuit, in particular the post-arc current. Since the post-arc current flows through plasma, left behind by the vacuum arc, the model needs to simulate the evolution of residual plasma during arcing as well. This is described in detail in Section 6.2. Models that simulate the post-arc current are described and discussed in Section 6.3. Attempts to simulate the VCB's post-arc behaviour with the aid of fluid equations, applied on plasmas have also been reported in the literature. Section 6.4 gives a summary of results obtained with such

models. Finally, Section 6.5 discusses the results from this chapter, and summarises its conclusions.

## 6.2 Residual plasma estimation

The theory in Chapter 2 explained that the post-arc conductance is the result of plasma, left behind by the vacuum arc. Therefore, it is necessary to simulate the development of plasma between the breaker's contacts during arcing. Since part of the plasma originates from vaporised anode material, which is heated by the arc, the anode's temperature has to be simulated as well. This is done in Section 6.2.1, and Section 6.2.2 describes the model that simulates the production and decay of plasma and vapour.

### 6.2.1 Anode temperature

Figure 6.1 depicts the configuration of the anode for which the temperature is evaluated. For simplicity, it is assumed that the heat source is uniformly distributed across the surface of interest, and that the temperature changes only in the direction perpendicular to this surface. This differs from the real situation, in which the load is higher near the centre of the anode than at its edge, especially during arc constriction (anode spot formation). The simplification limits the problem to one dimension. Initially, the anode's body is entirely solid, but depending on the source's strength, the surface starts to melt as time progresses. In the literature, the two-phase Stefan problem [60] is used to model this phenomenon.

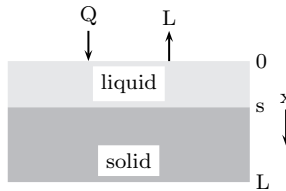


**Figure 6.1:** Configuration of the anode temperature model.

The temperature inside the anode is expressed by the equation of heat conduction:

$$\frac{\partial T(x, t)}{\partial t} = \alpha_i \frac{\partial^2 T(x, t)}{\partial x^2}, \quad (6.1)$$

where  $\alpha_i$  is the diffusivity of the material, which is expressed as

$$\alpha_i = \frac{\lambda_i}{\rho_i c_{p,i}}, \quad (6.2)$$



where  $\lambda_i$  is the thermal conductivity,  $\rho_i$  is the mass density and  $c_{p,i}$  is the specific heat capacity. The subscript  $i$  is either  $s$  or  $l$ , to denote whether the equations are valid for the solid or liquid material, respectively. The initial condition and the boundary conditions are:

$$T(x, 0) = T_0, \quad (6.3)$$

$$\frac{\partial T}{\partial x} \Big|_{x=0} = \lambda_i^{-1}(Q(t) - L_{ev}(t)) \quad (6.4)$$

$$T(L, t) = T_0, \quad (6.5)$$

where  $Q(t)$  is the heat source in  $\text{W/m}^2$ , and  $L_{ev}(t)$  is the cooling process. It has been investigated by others that heat loss due to radiation is negligible compared to evaporation [60], and therefore, this model takes only evaporation into account. From [10], the cooling process by evaporation is represented as:

$$L_{ev}(t) = \frac{\epsilon}{4} \frac{p_{ev}(T)}{(mkT/3)^{1/2}}, \quad (6.6)$$

where  $\epsilon$  is the evaporation energy per atom,  $p_{ev}$  is the saturated vapour pressure at the surface,  $m$  is the mass of a single atom of the anode's material and  $k$  is Boltzmann's constant. The relation between the saturated vapour pressure and the temperature of any material has been found as [61]

$$\log(p(t)) = \log(1.333 \cdot 10^2)(-A_i/T + B_i + C_i \log(T) + D_i T), \quad (6.7)$$

where  $A_i$ ,  $B_i$ ,  $C_i$  and  $D_i$  are material (and state) dependent parameters. The velocity with which the boundary between the solid and the liquid layer moves, is derived with

$$\frac{ds}{dt} = \frac{\lambda_l}{\rho_l H} \frac{\partial T}{\partial x} \Big|_{s-} - \frac{\lambda_s}{\rho_s H} \frac{\partial T}{\partial x} \Big|_{s+}, \quad (6.8)$$

where  $H$  is the latent heat of melting. As soon as the surface temperature increases beyond the melting temperature, the evaporation process causes the position of the surface to change. Instead of actually replacing the location of the heat source, the model accounts for the surface displacement by shifting the anode such that its surface is always at  $x = 0$ . To do this, Equation 6.1 is rewritten as

$$\frac{\partial T(x, t)}{\partial t} = \alpha_i \frac{\partial^2 T(x, t)}{\partial x^2} + v_{sur} \frac{\partial T}{\partial x}, \quad (6.9)$$

with  $v_{sur}$  as the velocity of the surface displacement, derived as

$$v_{sur} = \max \left( 0, \frac{F_{ev} m}{N_A \rho_l} \right), \quad (6.10)$$

where  $F_{ev}$  is the flux of evaporating particles and  $N_A$  is Avogadro's constant.  $F_{ev}$  is found as

$$F_{ev} = \frac{1}{4}nv = \frac{p_{ev}(T)}{4(mkT/3)^{1/2}}, \quad (6.11)$$

where  $n$  is the vapour particle density.

Simulation of the anode temperature now requires an expression for the power density  $Q$  in Equation (6.4). Assume, for a first approximation, that this power density can be derived by

$$Q = \frac{i_{arc}u}{A} \quad (6.12)$$

where  $u$  is a voltage that represents the heating by ion bombardment, and  $A$  is the discharge area. To simplify matters, it is assumed that the energy which the ions gain in the cathode area is transmitted to the anode, i.e. they do not lose their energy during their travel towards the anode. Since the arc constricts as the current reaches high values, the discharge area  $A$  is smaller than the anode area. However, for simplicity, it is assumed in the next example that  $A$  is constantly small during the entire simulation.

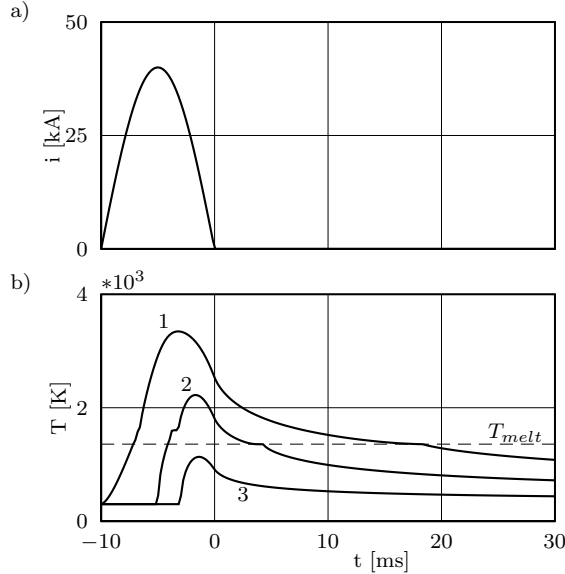


**Figure 6.2:** a) The short-circuit current, b) the simulated anode surface temperature for 1:  $t_{arc} = 10$  ms, 2:  $t_{arc} = 5$  ms and 3:  $t_{arc} = 3$  ms.  $T_{melt}$  is the melting temperature of copper.

The following analysis calculates the temperature of a copper anode, loaded by a vacuum arc that results from a sinusoidal current with a peak value of 40 kA. The arc voltage is assumed to be 15 V, and the diameter of the discharge area is 2.5 cm. The layer thickness  $L$  of which the temperature distribution is calculated is 5 mm. Appendix D gives more details both on the solution for the model, as well as the values for the parameters.

Figure 6.2 shows the simulated anode temperature for three different arcing times. In general, the results agree well with simulated and measured results in the literature, e.g. such as in [62]. However, as soon as the surface temperature increases beyond the melting temperature, the results show some distortion, which is particularly clear in the simulation with  $t_{arc} = 5$  ms. Here, the temperature remains practically on the same level for some time, but continues to increase afterwards.

The choice for the layer thickness is such, that at the instant of interest (current zero), the propagation of the heat has not reached the far end of the layer. Since the temperature at the far end is fixed, it acts as a perfect sink for heat, but this does not represent the reality. Figure 6.3 shows the temperature distribution at four different instants of the simulation with  $t_{arc} = 10$  ms. It demonstrates that the layer is sufficiently thick for the simulation until current zero, but that eventually, the heat reaches the layer's far end (the temperature gradient at  $x = 5$  mm is non-zero), which makes the model invalid.

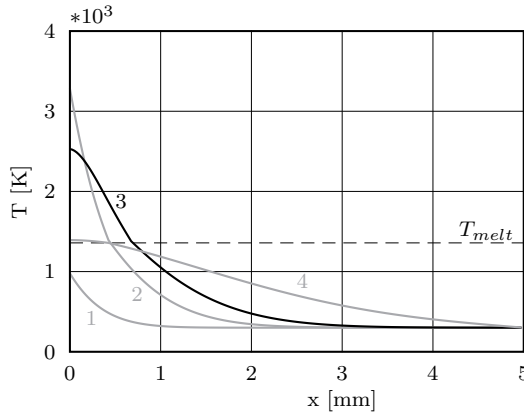


**Figure 6.3:** The anode temperature distribution at 1:  $t = -8$  ms, 2:  $t = -4$  ms, 3:  $t = 0$  ms (current zero) and 4:  $t = 15$  ms.  $T_{melt}$  is the melting temperature of copper.

### 6.2.2 Plasma development

One way to simulate the production and loss of charge and vapour during the arcing phase, without being too complicated is presented in [63]. The following model is predominantly based on the model described in this publication.

In this model, the cathode and the anode are the primary source of ions and neutral particles, respectively. While neutrals are assumed to leave the anode region with their thermal velocity, ions leave the cathode region much faster, as explained in Section 2.2.2. As time progresses, ions and neutrals might collide with each other, and exchange their charge. This process results in fast neutrals and slow ions. Therefore, the model simulates the density and velocity of four species: fast ions, slow neutrals, slow ions and fast neutrals.

The production of fast ions  $N_i^f$  is described by

$$\frac{\partial N_i^f}{\partial t} = \frac{0.1 \cdot I}{q_i d \cdot A} - \frac{N_i^f \cdot v_i^f}{l_{typ}} - N_{ex}, \quad (6.13)$$

where  $I$ ,  $q_i$ ,  $d$ ,  $v_i^f$  and  $l_{typ}$  are the arc current, the ion charge, the contact distance, the convection velocity of fast ions and the typical scaling length of diffusion, respectively. The first term on the right hand side of Equation (6.13) represents the production of ions. About 10 % of the arc's current is ion current, hence the factor 0.1 in this term. The second term of the right hand side of Equation (6.13) describes the loss of fast ions due to diffusion.  $N_{ex}$  describes the loss due to charge exchange, and is derived with

$$N_{ex} = \left( N_i^f \cdot N_n^s - N_i^s \cdot N_n^f \right) \cdot \Omega \cdot v_{rel} \quad (6.14)$$

where  $N_n^s$ ,  $N_i^s$ ,  $N_n^f$ , are the density of slow neutrals, slow ions and fast neutrals, respectively,  $\Omega$  is the charge exchange cross section and  $v_{rel}$  is the relative velocity between the interacting species involved. The density of slow neutrals is calculated with

$$\frac{\partial N_n^s}{\partial t} = \frac{N_{anode} \cdot v_{anode}}{d} - \frac{N_n^s \cdot v_n^s}{l_{typ}} - N_{ex}, \quad (6.15)$$

where  $N_{anode}$  is the particle density evaporated from the surface, derived from Equation 6.11. The density of slow ions and fast neutrals is calculated with

$$\frac{\partial N_i^s}{\partial t} = -\frac{N_i^s \cdot v_i^s}{l_{typ}} + N_{ex}, \quad (6.16)$$

$$\frac{\partial N_n^f}{\partial t} = -\frac{N_n^f \cdot v_n^f}{l_{typ}} + N_{ex}, \quad (6.17)$$

The fraction of particles having a thermal velocity is calculated with

$$\eta = 1 - \exp[-d \cdot (N_n^s + N_n^f) \cdot \Omega] \quad (6.18)$$

The typical distance after which particles leave the gap, and the particle velocities are calculated with

$$l_{typ} = \eta \cdot R + (1 - \eta) \cdot d, \quad (6.19)$$

$$v_i^f = \eta \cdot v_{thermal} + (1 - \eta) \cdot v_{cathode}, \quad (6.20)$$

$$v_i^s = \eta \cdot v_{thermal} + (1 - \eta) \cdot v_{anode}, \quad (6.21)$$

$$v_n^f = \eta \cdot v_{thermal} + (1 - \eta) \cdot v_{anode}, \quad (6.22)$$

$$v_n^s = \eta \cdot v_{thermal} + (1 - \eta) \cdot v_{cathode}, \quad (6.23)$$

$$v_{rel} = \eta \cdot v_{thermal} + (1 - \eta) \cdot v_{cathode}, \quad (6.24)$$

where  $v_{thermal}$  is the velocity for particles with the same temperature as the anode, calculated with Equation (6.10), and  $v_{cathode}$  and  $v_{anode}$  is the average drift velocity with which particles leave the cathode and anode region, respectively.

This model has been implemented in the existing model that simulates the anode temperature. To verify its correct implementation, Figure 6.4 shows its results after using an identical current source as the one reported in [63].

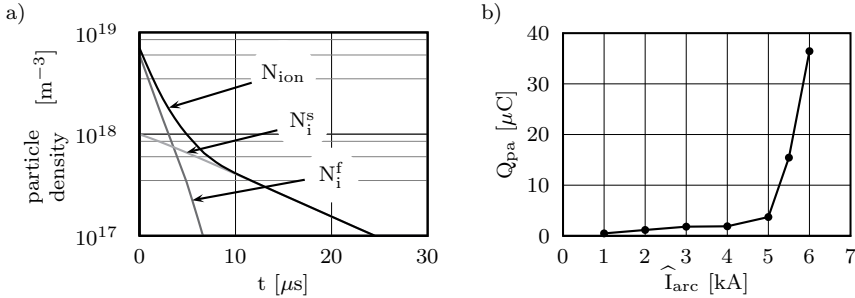


**Figure 6.4:** Simulation ion density decay after current zero. a) Ion density decay after a trapezoidal arc current of 5 kA peak, b) the residual charge after trapezoidal arc currents as a function of the peak current value.

Figure 6.4b shows a sudden increase in the post-arc charge after a short-circuit current of 5 kA. Beyond this current, the anode melts and suddenly produces large amounts of vapour and charge. The shape of this trace corresponds to the results shown in Figure 4.5 (page 59), and results from the literature like [16, 63], however, the value for the short-circuit current at which anode melting occurs is quite low. This indicates, for example, that the assumed size of the discharge area was too small.

## 6.3 Black-box modelling

For many years, the post-arc current in VCB's has been modelled with the aid of Child's law, which was later modified by Andrews and Varey. These models simulate the growth of the cathodic space-charge sheath towards the post-arc anode, as described in Section 2.4. Since it has been used so many times in the past, Section 6.3.1 elaborates on these models, and discusses their results.

One of the disadvantages of the models of Child and Andrews and Varey, is that they lack a proper theory for the voltage-zero phase. Section 4.4 gave details on how this phenomenon can be explained when the thermal velocity of particles is taken into account. The simplicity of the equations of this model makes it possible to implement them in a VCB model for network applications. Section 6.3 describes how this is done, and discusses its results.

### 6.3.1 Sheath model

The models in this section take only the kinetic motion of charged particles into account, and not their thermal. As a result, the direction in which the charged particles move is controlled by the electric field, which implies that during the sheath growth, only ions arrive at the cathode, and the electrical current  $i$  can be written as

$$i = q_i v_i n_i A, \quad (6.25)$$

where  $q_i$  is the average ion charge,  $v_i$  is the velocity of ions just before they arrive at the cathode,  $n_i$  is the ion density at the cathode surface, and  $A$  is the discharge area. Solving this equation requires an estimation for  $v_i$  and  $n_i$ , which is particularly difficult, because the velocity and density of ions are influenced by natural decay and a variable electric field in the sheath.

Since the model assumes that the sheath is completely free of electrons, Equation 6.25 holds for any location inside the sheath. The electric field at the plasma-sheath edge is zero, which makes this position the most convenient one to derive this equation. However, since the sheath grows into the plasma, 'stationary' ions inside the plasma move through the sheath edge. As a result, from its perspective, an additional ion current flows through the sheath, and the current at the sheath edge is derived as

$$i = q_i \left( v_i + \frac{ds}{dt} \right) n_i A, \quad (6.26)$$

where  $v_i$  and  $n_i$  are now the ion velocity and density at the sheath edge, and  $ds/dt$  is the velocity of the sheath edge. The relation between the voltage  $u$ , current  $i$  and thickness of a space charge layer  $s$  has been derived by Child [64], and is given as

$$i = \frac{4\varepsilon_0 A}{9} \sqrt{\frac{q_i}{m_i}} \frac{u^{3/2}}{s^2}, \quad (6.27)$$

where  $\varepsilon_0$  is the permittivity of vacuum and  $m_i$  is the ion mass. One of the assumptions made for Child's model is that ions start at rest. However, as long as the sheath moves, Equation (6.26) implies that ions in this model always have an initial velocity, and that as a result, Child's model cannot be used in this case.

Andrews and Varey found a way to include the initial velocity of ions [65] into Child's model, and their result is

$$s^2 = \frac{4\varepsilon_0 U_0}{9q_i n_i} \left[ \left( 1 + \frac{u}{U_0} \right)^{3/2} + 3 \frac{u}{U_0} - 1 \right], \quad (6.28)$$

$$U_0 = \frac{m_i}{2q_i} \left[ v_i + \frac{ds}{dt} \right]^2, \quad (6.29)$$

where  $U_0$  is the ion potential at the sheath edge.

Equation (6.28) is only valid in the second phase of the post-arc current (see Section 2.4, Figure 2.5). In the first phase, the voltage is assumed to be zero (perfect conduction). In the third phase, when the sheath thickness  $s$  has grown as large as the contact distance  $d$ , the current is assumed to have reached zero (perfect insulation). The transition from the first to the second phase has completed as soon as the current reaches  $q_i v_i n_i A$ .

The model now requires values for  $q_i$ ,  $v_i$ ,  $n_i$ ,  $d$  and  $A$ .  $q_i$  is usually taken as 1.8 times the elementary charge ( $1.6 \cdot 10^{-19}$  C), which is the average charge value of copper ions that has been measured in vacuum arcs [66, 67]. During the evaluation of the model, the values for  $v_i$ ,  $d$  and  $A$  are generally constant, where  $v_i$  (the velocity of ions leaving the cathode spot region) is taken between  $10^3$  and  $10^5$  m/s [65, 68, 69],  $d$  is the measured contact distance, and  $A$  a fraction of the anode area, which represents the possible constriction of the arc.

In line with the observations on the ion density measured after current zero, an exponential decay is usually taken to model  $n_i$ . As a result,  $n_i$  requires at least one additional parameter that represents the decay time constant  $\tau$ . This value is usually taken between  $0.5 \mu\text{s}$  and  $84 \mu\text{s}$  [14, 19, 20]. Section 6.2.2 already simulated the ion density decay after current zero, and these results can also be used in the post-arc current model. To make the results of this model fit the measurements better, alternatives have also been suggested [49, 66, 68, 70, 71, 72, 73].

The model has been implemented as a system block in Matlab's SimPowerSystems, which makes it easy to apply it in different electrical circuits. Figure 6.5 shows results of it when applied in an SLF test circuit, along with measured data.

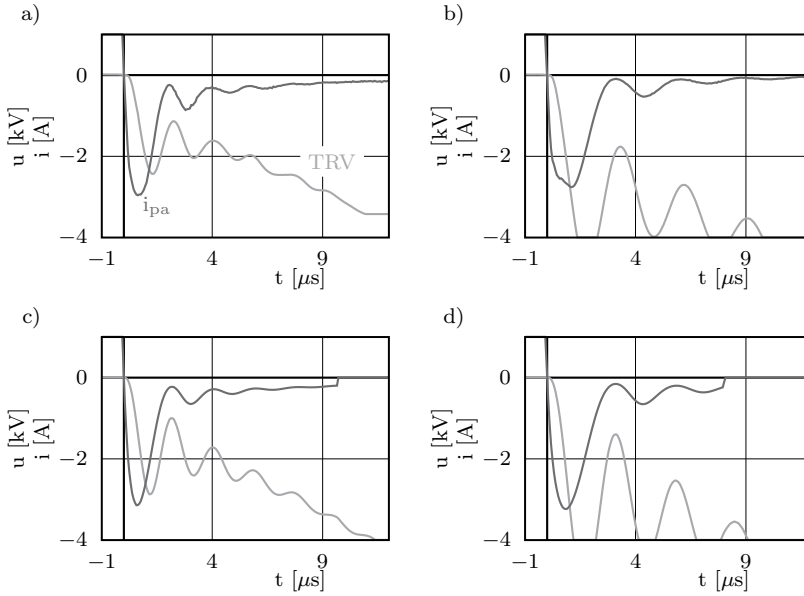


**Figure 6.5:** Results from the Sheath model of Andrews and Varey, compared with measured data from Short-Line Fault tests. a) Data from 1 with  $L_{\%} = 105 \mu\text{H}$  (see Figure 3.4), b) data from 1 with  $L_{\%} = 225 \mu\text{H}$ . c) and d) are the simulated results of the measurements in a) and b), respectively.

### 6.3.2 Langmuir probe model

As already mentioned in Section 4.4, the vacuum interrupter can be regarded as a Langmuir probe. To find a relation between the current and the voltage for the interrupter in the voltage-zero period, the interaction between the plasma and one contact needs a closer look.

For the stability of the sheath, the electric field in front of a contact partly penetrates the quasi-neutral plasma. This field not only starts the deceleration of electrons, but it also accelerates ions into the direction of the sheath to velocities exceeding their thermal velocity. As a result, ions enter the sheath with *Bohm velocity*  $v_B$ . Without further elaborating on how  $v_B$  is derived, its expression is given as [52, 53, 54]

$$v_B = \left( \frac{2kT_e}{m_i} \right)^{1/2}, \quad (6.30)$$

where  $k$  is Boltzmann's constant,  $T_e$  is the electron temperature and  $m_i$  is the ion mass. By setting  $v_i = v_B$  in Equation (6.25), the ion saturation current can be written as



$$i_{i,sat} = q_i v_B n_i A, \quad (6.31)$$

where  $q_i$  is the average ion charge,  $n_i$  is the ion density at the plasma-sheath boundary and  $A$  is the contact's surface area.

When a Maxwellian distribution function is assumed for electrons at the plasma-sheath boundary, the electron current  $i_e$  is found as

$$i_e = J_{e,sat} A \exp\left(\frac{q_e V_p}{k T_e}\right), \quad (6.32)$$

where  $J_{e,sat}$  is the electron saturation current density,  $q_e$  is the elementary charge and  $V_p$  is the voltage drop across the sheath. Equation 6.32 effectively implies that electrons at the plasma-sheath boundary require an initial velocity  $v_e$  such that  $\frac{1}{2} m_e v_e^2 \geq q_e |V_p|$ . Similar to the ion saturation current, the electron saturation current is reached when a contact's potential reaches a high positive value with respect the plasma potential. In absolute values, the electron saturation current is much higher than the ion saturation current.

In the configuration of Figure 4.20, the current  $i$  through the loop is equal at both contacts, hence

$$i = i_e^a - i_{i,sat}^a = i_{i,sat}^c - i_e^c, \quad (6.33)$$

where the superscripts  $a$  and  $c$  refer to the anode and cathode, respectively. Combining Equations (6.32) and (6.33), and using  $V = V_p^a - V_p^c$  for the voltage across the gap gives

$$\frac{i + i_{i,sat}^a}{i_{i,sat}^c - i} = \frac{A^a}{A^c} \exp\left(\frac{q_e V}{k T_e}\right). \quad (6.34)$$

Since it is assumed that the contacts have equal size, Equation (6.34) can be simplified to

$$i = i_{i,sat} \tanh\left(\frac{q_e V}{2 k T_e}\right). \quad (6.35)$$

Equation (6.35) indicates that the total current is restricted to the ion saturation current at either one of the contacts. As a result, neither contact will experience the much higher electron saturation current in this model.

Next, the model is compared with the measurement of Figure 4.19. In this particular example, the test-object was subjected to a short-circuit current that largely exceeded the breaker's rated value. As such, the amount of residual charge at current zero is relatively large, making it easier to observe the low-voltage phase. The model is evaluated in a circuit that is similar to the one from which the measurement has been obtained.

The quantities  $T_e$ ,  $m_i$  and  $n_i(0)$  (the initial ion density), cannot be measured with the measuring equipment used in this research, and their value has to be estimated, or taken from the literature.  $kT_e$  is usually in the order of 2-10 eV [74, 75, 76, 77], and the model supposes that only copper ions are present inside the gap, so  $m_i = 1.06 \cdot 10^{-25}$  kg. The calculation of the ion density is arranged by the model described in Section 6.2.2.

The results from measurements on the initial ion density, and its decay, have also been reported frequently in the literature, with values for  $n_i(0)$  in the range of  $10^{17} - 10^{19} \text{ m}^{-3}$ , and values for  $\tau$  ranging from  $0.5 \text{ } \mu\text{s}$  to  $84 \text{ } \mu\text{s}$  [69, 14, 78, 20, 19]. The values for the parameters in this model are within these ranges to match the model's results with the measured data.

The contact diameter of the VCB that was used in this analysis is 4 cm, thus  $A$  is  $12.5 \text{ cm}^2$ .  $kT_e$ ,  $q_i$  and  $n_i(0)$  are taken 3 eV,  $1.8 \cdot 1.6 \cdot 10^{-19} \text{ C}$  and  $2.8 \cdot 10^{18} \text{ m}^{-3}$ , respectively, and the time constant  $\tau$  for the ion decay is  $20 \text{ } \mu\text{s}$ .

Figure 6.6 presents the results, which shows indeed a voltage-zero period in the simulation that resembles the one in the measurement.

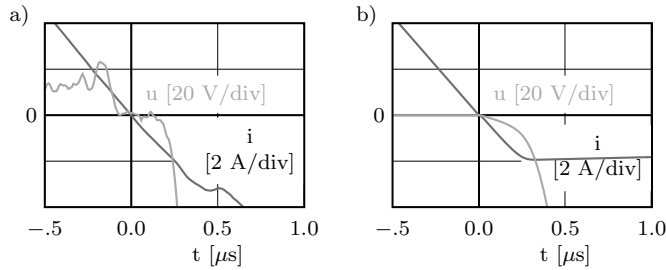


**Figure 6.6:** Simulation of the low-voltage period following current zero; a) measured data, b) simulation results.

The rise of the recovery voltage entails a fast time-change in the electric field inside the ionic space-charge sheath in front of the cathode. This yields a displacement current, which has not yet been taken into account in the model so far. Hence, in the model, the current remains equal to the saturation current, whereas the measured current continues to increase for some time. A way to model this event is described below.

For simplicity, it is assumed that the effective cathode area increases linearly with the voltage, thus

$$A_{eff}(t) = A + c_1 V, \quad (6.36)$$

where  $c_1 [\text{m}^2/\text{V}]$  is a parameter that has yet to be determined.

The model assumes a twofold decay of ion density after current zero. The first is a natural decay, assumed exponential, and the second is from the post-arc current. Based on this, the ion density is defined as

$$\frac{dn_i}{dt} = -\frac{n_i}{\tau} - \frac{i_{pa}}{q_i c_2}, \quad (6.37)$$

where  $\tau$  is the time constant for the natural decay and  $c_2$  [m<sup>3</sup>] is a parameter.  $i_{pa}$  is considered to be positive only in Equation (6.37), to ensure an ion density decay.

A sheath capacitance is used for modelling the displacement current that results from the time-change of the electric field inside the sheath. The expression for the sheath capacitance is

$$C_{sh} = \frac{K}{V^{3/4}}. \quad (6.38)$$

Appendix F describes how  $K$  in Equation (6.38) is elaborated.

By combining Equations (6.31), (6.35), (6.36) and (6.38), the expression for the post-arc current can be written as

$$i_{pa} = q_i n_i v_B A_{eff} \tanh\left(\frac{q_e V}{2kT_e}\right) + C_{sh} \frac{dV}{dt}, \quad (6.39)$$

When  $m_i$  (from  $v_B$ , Equation (6.30)),  $q_i$ ,  $T_e$  and  $A$  are considered constant, the model requires four parameters:  $n_i(0)$ ,  $\tau$ ,  $c_1$  and  $c_2$ .

This model has been added to the models of Section 6.2, which is implemented as a function block in Matlab's SimPowerSystems. For the simulation of the breaker in an electrical circuit, the `ode23tb` solver has been used with an absolute and relative error of  $1 \cdot 10^{-5}$ . Figure 6.7 shows the result of the simulation of the measurement in Figure 4.19. This simulation uses the same values for the parameters as were used in the simulation of Figure 6.6, and in addition,  $c_1$  and  $c_2$  are  $0.5 \cdot 10^{-6}$  m<sup>2</sup>/V and  $56 \cdot 10^{-6}$  m<sup>3</sup>, respectively.

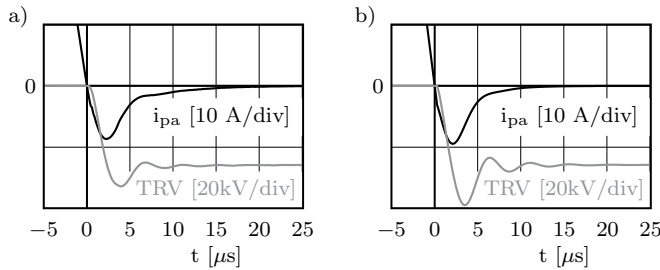


**Figure 6.7:** Simulation of the post-arc current; a) measured data, b) simulation results.

In the final example, the model simulates three measurements, that were performed with equal test settings (same arcing time and same peak short-circuit current), but with different TRV's. Figure 6.8 shows the results.

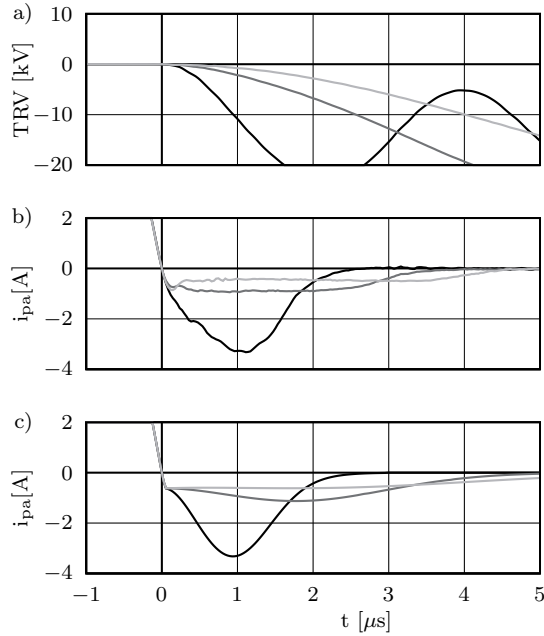


**Figure 6.8:** The simulation of three measurements, performed with equal conditions but different TRV. a) the measured TRV, b) the measured post-arc current and c) the simulated post-arc current.

Because the three measurements were performed with equal settings, it should be expected that the plasma conditions at  $t = 0$  were equal as well. Consequently, the model's parameters should be the same in all three simulations. The parameters  $n_i(0)$ ,  $\tau$  and  $c_2$  were indeed equal ( $7 \cdot 10^{17} \text{ m}^{-3}$ ,  $5 \mu\text{s}$  and  $33 \cdot 10^{-6} \text{ m}^3$  respectively), but only  $c_1$  had to be adjusted. This value was  $2 \cdot 10^{-6} \text{ m}^2/\text{V}$  for the measurement with the steepest TRV rise,  $1 \cdot 10^{-6} \text{ m}^2/\text{V}$  for the middle and  $0.5 \cdot 10^{-6} \text{ m}^2/\text{V}$  for the slowest TRV rise. Since this parameter is used in Equation (6.36) to relate the effective cathode area to the voltage, this assumed relation appears to be inadequate.

## 6.4 Alternative post-arc current models

Although Andrews and Varey developed a model that is most widely used to simulate the post-arc current in VCBs, other models have been suggested in the past as well. Most of these alternatives elaborate on the equations for particle motion between the contacts. Such equations are an extension of the fluid dynamic equations with which the motion of particles in gasses are modelled. In a plasma, the fluid dynamic equations are extended with the Poisson equation to account for the force that an

electric field exhibits on the charged particles. In a simplified, one dimensional model, these equations are [79, 80]

$$\frac{\partial n_k}{\partial t} + \frac{\partial n_k v_k}{\partial x} = 0 \quad (6.40)$$

$$m_k n_k \left( \frac{\partial v_k}{\partial t} + v_k \frac{\partial v_k}{\partial x} \right) + \frac{\partial p_k}{\partial x} = -q_k n_k \frac{\partial \phi}{\partial x}, \quad (6.41)$$

$$\frac{\partial^2 \phi}{\partial x^2} = -\frac{1}{\varepsilon_0} (q_e n_e + q_i n_i), \quad (6.42)$$

where  $n_k$ ,  $v_k$ ,  $p_k$ ,  $q_k$  and  $m_k$  are the particle density, velocity, pressure, charge and mass, respectively,  $\phi$  is the potential inside the plasma and  $\varepsilon_0$  is the permittivity of vacuum. The subscript  $k$  is either  $e$  or  $i$  to distinguish the equations between electrons or ions, respectively. Equation (6.40) describes the mass conservation and Equation (6.41) the momentum transfer. Equation (6.42) is the Poisson equation. This model requires additional equations for the pressure  $p_k$  to describe thermodynamic process of the particles (e.g. isothermal electrons and adiabatic ions).

The current through the plasma is derived as

$$i = q_i n_i v_i A + q_e n_e v_e A + \varepsilon_0 A \frac{dE}{dt}, \quad (6.43)$$

where  $E$  is the electric field. Note that this equation is valid anywhere inside the plasma. The electric field  $E$  is found as

$$E = -\frac{d\phi}{dx}. \quad (6.44)$$

This post-arc current model is completed when it is supplemented with a system of equations describing the electrical circuit, which induces a potential difference across the plasma (the TRV). This potential difference is then used as the boundary condition for Equation 6.42.

Solving this system of equations requires considerable numerical effort because of several reasons, two of which are discussed in the following. First, Equation (6.41) requires knowledge of the potential distribution, while this has yet to be derived with Equation (6.42). For this reason, the system has to be solved with an iterative process, in which the voltage distribution is first estimated, and updated after each iteration step until the required accuracy has been reached. Second, the extremely large ion/electron mass ratio (about  $10^5$ ) and in addition, the high mobility of electron easily causes instability of the numerical evaluation and forces it to use very small time steps (less than  $10^{-12}$  s). Other methods have been suggested for solving  $n_e$  and  $v_e$  with Equations (6.40) and (6.41), for example by linking  $n_e$  directly to the potential via the Boltzmann law [81, 82].

Although the results of this model might support the theory postulated in Section 4.4 (with regard to the voltage-zero phenomenon), the complexity involved with

its evaluation goes well beyond the scope of this research. In addition, the one dimensional model is unrealistic in its current form, but adding more dimensions to it leads only to a higher complexity, and makes the result consequently more dependent on estimated initial conditions. For these reasons, it has not been evaluated.

## 6.5 Discussion and conclusions

It was the intention of this work to simulate the current interruption process in vacuum in a similar way as has been done with SF<sub>6</sub>. Such a model makes it possible to simulate the breaker's behaviour numerically in different electrical circuits. The SF<sub>6</sub> arc extinction process has been modelled with relative success by using the models of Cassie and Mayr [36]. These involve the balance between the internal energy of the arc and the cooling power of the surrounding gas, and link the arc's conduction to the internal energy. After current zero, the cooling power has to be stronger than the arc's internal energy to successfully extinguish the arc.

Vacuum arcs break short-circuit currents in quite a different way, as VCBs lack an extinguishing medium, and their arc's internal energy is almost completely concentrated in the cathode spots. The reignition process is also quite different, since the source of the new arc (cathode spots) arise at a different location (the new cathode) than before current zero. For this reason, post-arc vacuum modelling has been mainly focussed on simulating the anode temperature during arcing, and the behaviour of the cathodic space charge sheath after current zero, because both involve the conditions at the location of potentially new cathode spots.

This chapter showed how the time behaviour of the anode surface temperature can be modelled. It assumed that all of the arc's energy is transformed into heat that conducts into the anode. It also assumed that the heat is not equally distributed across the anode's surface, but only to a given fraction of it. Although this assumption agrees with observations made in the literature, the real size of this spot changes in time, and depends on many properties, such as the value of the current, the magnetic field and the history of the arc. Including all these processes probably lead to better results, but also to more complexity to the already elaborated model.

The anode surface temperature model is used for the simulation of the production and elimination of charge and vapour inside the gap. This model is based on [68], which simulates the density of four species, each with different properties. These are the charge (ions and neutrals) and their average velocity (referred to as 'fast' or 'slow'). It assumed that during arcing, the cathode creates fast ions, whereas the anode creates slow neutrals. Depending on the density and their average velocity, a fraction of the fast ions collide with slow neutrals, and exchange their charge in the process, thereby creating slow ions and fast neutrals. As soon as the current through the breaker reaches zero, the source of fast ions is removed, and the remaining charge and vapour inside the gap falls into decay. The residual charge from this model is what made the simulation of the post-arc current possible.

The theory of a Langmuir probe, described in Section 4.4, was used to simulate the post-arc current. This model assumes that after the current reaches a saturation value, the rise of the voltage leads to the growth of the space-charge sheath in front of the cathode while the current remains constant. However, the time change of the voltage makes a higher current possible, because this leads to a displacement current inside the sheath. To account for the displacement current, the sheath is modelled as a voltage-dependent capacitor that shows similarity with the model of Andrews and Varey, which has been used extensively in the past to simulate a VCB's post-arc current. Finally, the model was supplemented with additional mechanisms to account for geometry effects of the growing sheath, to make the simulated results correspond to the measured results.

Although modelling of the vacuum arc - circuit interaction improves the understanding of the current-quenching mechanism in vacuum, there are three main reasons why it will probably never serve as a reliable performance indicator tool for VCBs:

1. The many processes on which the model is based allow their parameters to be adjusted to make the simulated results fit the measured results. Since most of the parameters are from processes that could not be measured (such as the discharge area with which the arc loads the anode, and the average velocity of particles), such adjustments cannot be validated.
2. Despite complexity of the model, and the numerical efforts that the simulation requires, it is impossible to predict the post-arc current of a future test. This is because of the inherent scatter that the post-arc current exhibits, for example due to the final position of the last cathode spot, as explained earlier in Section 2.4.
3. The models do not predict failure ( $\text{SF}_6$  models do), let alone that clear understanding exists on reignition processes in vacuum.





## Chapter 7

# General conclusions and recommendations

### 7.1 Conclusions

The high quality of the measured data provided a firm foundation for the research on short-circuit interruption with vacuum circuit breakers. This quality was ensured by a combination of special test circuits, measuring systems and software for processing the raw data. IEC standards require vacuum circuit breakers to be subjected to specific tests, and since the High Power Laboratory at KEMA is specialised in performing such tests, their circuits are the most suitable ones for analysing the breaker's IEC compatibility. However, the High Currents Laboratory in Eindhoven proved to be a better location for more fundamentally oriented research on the current quenching mechanism in vacuum. This was because it provided accommodation for performing measurements, which was available during the entire course of the project.

A current measuring device, which has been specifically developed by KEMA for short-circuit tests, and has already been successfully used in the past, turned out to be of high value for this project as well. Although the signal from this 'Rogowski coil' had to be processed to recover the current (it actually measures the time-derivative of the current), it produces the strongest signals at the most significant instants of a measurement (i.e. the current zero). In addition, its galvanic isolation from the test circuit made it practically invulnerable to ground-loop distortion. This is quite different from the voltage measurement system. Since the voltage probes used in this research were all connected to the test circuit, they required special treatment to protect the data recording devices from the high voltage, and to suppress ground-loop interference. Both requirements were optimally satisfied by using a special data recording system. This system comprises battery operated buffers (Front Ends), which are linked to a receiving recorder through glass fibre cables. Because

of its excellent performance on shielding the measured signals from the strong electromagnetic distortion that involves a short-circuit test, most of the data in this research has been acquired using this particular system.

The vacuum arc's electrical properties were obtained from the raw data after treatment with software, that has been specifically developed for this purpose. This software has previously been used for analysing short-circuit measurements on SF<sub>6</sub> breakers at KEMA. In this research, it successfully processed the data from the different recording systems as well. As a result, over 350 current-zero measurements were collected for analysis.

### The voltage-zero period

The high level of detail in the voltage and current measurements made it possible to clearly demonstrate the plasma nature of the post-arc current. This nature revealed itself in the measurements predominantly, by a voltage-zero period that immediately follows current zero. Here, the breaker appears to delay the rise of the recovery voltage by keeping its conductance particularly high for a period lasting several tenths of microseconds. This is beneficial for the interruption process, since the delay of the TRV also extends the period in which the breaker can recover from the arc. This behaviour shows a striking similarity with that of a double Langmuir probe (of which the electrical properties are known), which is normally used for analysing a plasma on its ion density and its electron temperature.

The voltage-zero period ends as soon as the post-arc current reaches the *ion saturation current*  $i_{sat}$  (see Section 6.3.2). As such, the electrical circuit controls this duration, because it controls the current slope in this period, and the current reaches  $i_{sat}$  earlier when it has a steep slope. Although the ion saturation current can be measured in this way, the parameters that determine  $i_{sat}$  itself cannot be measured from outside the vacuum interrupter. These parameters are the electron temperature  $T_e$ , the ion mass  $m_i$ , the average ion charge  $q_i$ , and the discharge area  $A$ , which are all approximately constant in the voltage-zero period, and the time dependent ion density  $n_i$ . Values for the parameters  $T_e$ ,  $m_i$  and  $q_i$  have been frequently reported in the literature, and can be taken from there, but  $A$  and the function for  $n_i$  have to be estimated.

### The post-arc current parameters

The post-arc current flows through the conducting residue of the vacuum arc. Therefore, the post-arc properties should be a reflection of the strain that the vacuum arc imposed on the breaker. However, trends could only be observed after comparing the arcing and post-arc parameters of a large number of measurements, because such trends exhibit a strong divergence, as explained in Section 4.2. The peak value of the short-circuit current  $\hat{I}_{arc}$  and the arcing time  $t_{arc}$  were taken as the arcing parameters. The post-arc parameters were the post-arc current's peak value  $\hat{i}_{pa}$ , its

charge  $Q_{pa}$  (its time-integral), its conductance and its capacitance at a given instant  $t$ ,  $G_t$  and  $C_t$ , respectively, and finally the time at which the conductance reaches a given value  $t_G$ . All the post-arc parameters depend more or less proportionally to the arcing parameters.

The most likely hypothesis for the scatter in the trends is caused by the difference in each test of the final location of last cathode spot. Since cathode spots move randomly across the cathode's surface, eject charge away from it in the process, their final position influences the amount of charge available in the inter-electrode gap at current zero.

Contrary to the weak relationship between the arc's and the post-arc parameters, the relationship between different post-arc parameters, e.g.  $G_t$  versus  $Q_{pa}$ , shows a strong coherence, which is demonstrated in Section 4.3. Apparently, the breaker exhibits the same physical process after current zero in each test, only with different initial conditions. This might be useful for research that compares the performance of different (types of) breakers. The nature of this research rendered data which proved too diverse for such a specific analysis.

## Reignition analysis

From the observations in this research, thermal reignition (reignition that occurs during the post-arc current) is a rare failure mechanism in vacuum (Section 5.2). It happened almost exclusively when the breaker had been subjected to a current that largely exceeded the breaker's rated short-circuit current. The parameter  $G_t \cdot d$  is a fair indicator for an imminent thermal reignition, where  $d$  is the contact distance at current zero, derived from  $t_{arc}$ . Above a given upper value of this parameter, and below a given lower value, the breaker is likely to reignite. These boundary values are not fixed, but are different for each breaker, and each type of test. The rate of rise of recovery voltage (RRRV) appears to have little influence on thermal reignition in vacuum, which is in contrast to such process in gas. The recently approved Amendment 2 of IEC standard 62271-100 obliges practically all VCBs to be subjected to SLF tests, however, from the conclusion that VCBs are well capable of managing a high RRRV (which is the gravity of an SLF), this seems an unnecessary exercise.

A great deal of the dielectric reignitions observed in this research occurred after  $1/4$  of one power frequency period. Had the test circuit been more similar to a real short-circuit network, then the alternating voltage would have changed polarity by then, thereby probably giving different results. This makes the circuit less suitable for analysing the breaker's IEC compatibility. The voltage-injection circuit (Section 3.2.2) proved to be well suitable for analysing reignitions, because its recovery voltage was higher than the voltage of the current-injection circuit (40 kV and 15 kV, respectively). Another benefit of the voltage-injection circuit is that it makes the measurement of mA currents through the test object, millisecond after current zero

possible (Section 5.4). Since the plasma has already decayed by then, such currents are likely the result of thermal-field emission.

## Modelling

Existing models, supplemented with theories for observations made in this research, can simulate a measured post-arc current quite accurately. However, predicting the outcome of a measurement with the aid of such a model appears to be impossible for two reasons. First, the degree of scatter observed in the relationship between test settings, post-arc properties and reignition behaviour, already demonstrated the improbability of finding a predictive value. The second reason is that in addition to the model's large number of parameters for which the values have to be assumed, the model also requires an expression for the time behaviour of the ion density. The simulation of the time changing ion density is based on another collection of assumptions, thereby automatically reducing the reliability of the final post-arc model. Consequently, such a model is only useful for analysing a VCB's interaction with an electrical circuit.

## 7.2 Suggestions for future work

One of the observations in this work is that VCBs seem not to suffer from short-circuit tests. The test objects were perfectly capable of withstanding the steep TRV that accompanies the short-line fault. However, although the total number of measurements collected during this research is large, the number of test series, and the number of different types of interrupters that were analysed, is limited (seven and three, respectively). In addition, each test series was unique, which made comparative studies on different interrupters impossible. This leads to the first recommendation for future work:

*Create a collection of test series with equal settings, but different VCBs.*

Such work will probably be expensive, since it requires a large amount of measuring time, and a reliable test circuit.

Another observation from this work is that the breakdown voltage for the analysed interrupters is significantly higher than the current-injection circuit could generate. The voltage-injection circuit has been used to increase this voltage to 40 kV, at the expense of the TRV's IEC compatibility. Despite the drawback, this circuit proved to be well suitable for research on vacuum breakdown, and on continuing post-arc emission currents, which is particularly interesting for the research on reignition behaviour (see Section 5.4). Since there is currently much debate going on about the nature of vacuum breakdown, the next recommendation would be:

*Use (and improve) the voltage-injection circuit for research on vacuum breakdown.*

Some suggestions for improvement of this circuit are

- increase its voltage level to a value beyond the 100 kV (this also makes a steeper rise of it possible);
- increase the value of  $R_{inj}$  (see Figure 3.13, page 33) to make the measurement of micro ampères post-arc currents possible.

These suggestions are also expensive to carry out, since they require suitable circuit components, and the breaker itself needs also be suitable for withstanding such high voltages.

The interrupter's recovery phase counts many processes in its sealed interior, and trying to explain them all only by looking at its electrical behaviour is not enough, as the post-arc current analysis has already demonstrated (see Chapter 4). In experimental interrupters (not used in this research), the recovery is also often monitored with, e.g. camera's, Langmuir probes or retarding field analysers [14], but these analysis techniques are impossible to apply on permanently sealed commercially available interrupters. Instead of also using an experimental interrupter, one could also do the following:

*Develop (or search for) a sensor that measures recovery processes inside the vacuum interrupter, without penetrating it.*

The type of signals that should be monitored have yet to be determined.



# Appendix A

## Eindhoven's parallel current-injection circuit

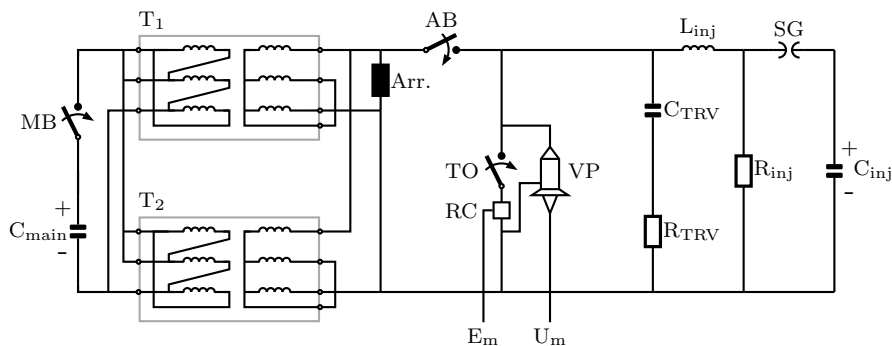


**Figure A.1:** The current-injection circuit used in the High-Currents Laboratory in Eindhoven.

**Table A.1:** Circuit component values and parameters.

Name	Value	Rating	Type (Manufacturer)	Figure
$C_{main}$	1.56 mF	15 kV		A.2
$C_{inj}$	83.4 $\mu$ F	15 kV		
$C_{TRV}$	0 – 11 nF			
$L_{inj}$	1.11 – 1.39 mH		Air coil	A.4
$R_{inj}$	250 $\Omega$		Stack of disk resistors (HVR)	
$R_{TRV}$	0 – 750 $\Omega$		Stack of disk resistors (HVR)	
$Arr.$		0.66 – 10 kA, 660 V	MVR (ABB)	
$MB$			Air circuit breaker	
$AB$		25 kA, 24 kV	Vacuum circuit breaker	
$TO$		20 – 25 kA, 10 – 24 kV	Vacuum circuit breaker	
$SG$			Triggered spark gap (TUE)	A.5
$T_1, T_2$		800 kVA, 10.5kV : 380 V	Dy5, oil transformer	A.3
$RC$	0.34 $\mu$ H mutual inductance		Rogowski coil (KEMA)	
$VP$		see Table 3.1	Voltage probe	





**Figure A.2:** Capacitor bank for  $C_{main}$ .

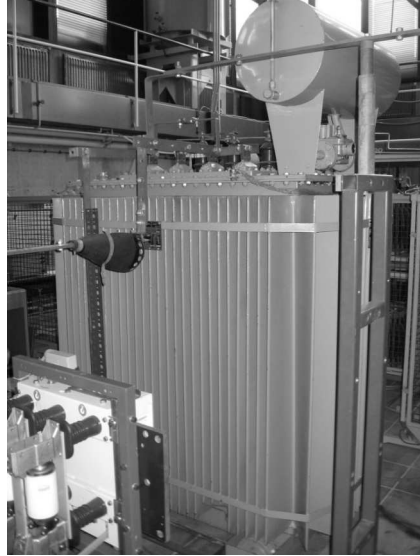


**Figure A.3:** Transformer  $T_1$ .

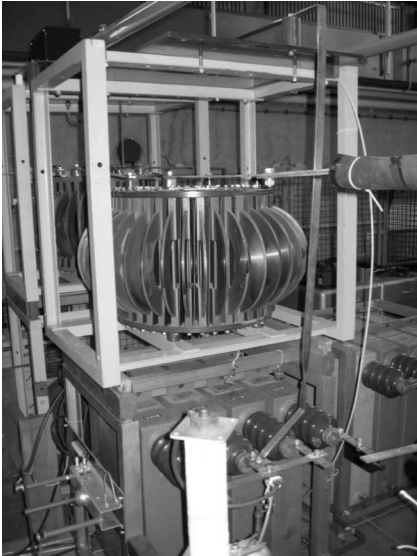


**Figure A.4:** One of the air coils used for  $L_{inj}$ .



**Figure A.5:** Heads of  $SG$



# Eindhoven's parallel voltage-injection circuit

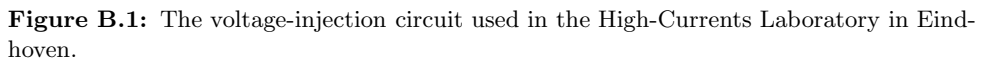


**Table B.1:** Circuit component values and parameters.

Name	Value	Rating	Type (Manufacturer)	Figure
$C_{main}$	1.56 mF	15 kV		A.2
$C_s$	2.5 nF			
$C_{a1}, C_{a2}$	330 pF			
$C_{inj}$	2.5 nF			
$C_{HV}$	125 nF	65 kV		B.2
$C_{TO}$			Parasitic capacitance	
$R_s$	160 $\Omega$		Stack of disk resistors (HVR)	
$R_{inj}$	1, 100 k $\Omega$		Stack of disk resistors (HVR)	
$R_{HV}$	70 $\Omega$		Stack of disk resistors (HVR)	
$Arr.$		0.66 – 10 kA, 660 V	MVR (ABB)	
$MB$			Air circuit breaker	
$AB_1, AB_2$		25 kA, 24 kV	Vacuum circuit breaker	
$TO$		20 – 25 kA, 10 – 24 kV	Vacuum circuit breaker	
$SG$			Triggered spark gap (TUE)	A.5
$T_1, T_2$		800 kVA, 10.5kV : 380 V	Dy5, oil transformer	A.3
$RC$	0.34 $\mu$ H mutual inductance		Rogowski coil (KEMA)	
$VP$		see Table 3.1	Voltage probe	

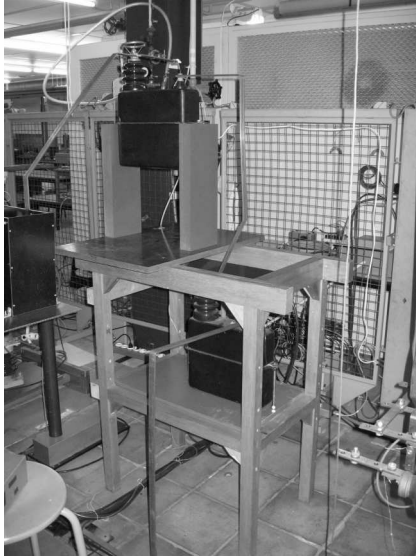


**Figure B.2:** The two series connected 250 nF capacitors, rated at 32.5 kV each, together forming  $C_{HV}$ .



## Appendix C

# A simplified post-arc conductance model

This appendix describes a first approximation to modelling the post-arc conductivity. Its sole purpose is to comprehend the trends observed in Figure 4.17, hence simplicity of the model prevails over its accuracy.

Assume that the time-dependent post-arc conductivity  $G(t)$  is given by

$$G(t) = G_0 \exp(-t/\tau), \quad (\text{C.1})$$

where  $G_0$  is the conductance at  $t = 0$ , and  $\tau$  is the conductance's decay time. A consequence of this model is that the interaction between the post-arc conductance and the TRV is absent, which is not entirely valid, considering the observations in Figures 4.7 and 4.8, but acceptable for a first approach. Assume further that the transient recovery voltage  $u$  across the breaker is

$$u(t) = U_0 (1 - \cos(2\pi f t)), \quad (\text{C.2})$$

where  $U_0$  is the system's voltage and  $f$  is the ground harmonic of the TRV. The post-arc current is then defined as

$$i_{pa} = G(t)u(t). \quad (\text{C.3})$$

The time-integral of Equation C.3 yields the post-arc charge  $Q_{pa}$ , which is

$$\begin{aligned} Q_{pa} &= \int_{t=0}^{\infty} i_{pa} dt \\ &= G_0 U_0 \frac{(2\pi f)^2 \tau^3}{1 + (2\pi f)^2 \tau^2}. \end{aligned} \quad (\text{C.4})$$

Solving  $\tau$  from Equation C.1, and using this result in Equation C.4 gives

$$Q_{pa} = G_0 U_0 \frac{(2\pi f)^2 t^3 / \ln \left( \frac{G_0}{G(t)} \right)^2}{1 + (2\pi f)^2 t^2 / \ln \left( \frac{G_0}{G(t)} \right)^3}, \quad (\text{C.5})$$

hence, the relation between  $Q_{pa}$  and  $t_G$  (the instant at which  $G(t)$  reaches a particular value) becomes

$$Q_{pa} = G_0 U_0 \frac{K_1 t_G^3}{1 + K_2 t_G^2}, \quad (\text{C.6})$$

where

$$K_1 = \frac{(2\pi f)^2}{\ln \left( \frac{G_0}{G_t} \right)^2},$$

$$K_2 = \frac{(2\pi f)^2}{\ln \left( \frac{G_0}{G_t} \right)^3}.$$

Figure 4.18 shows the results of this model, with the parameters from Table C.1. For simplicity,  $t_G$  is used as variable, instead of  $Q_{pa}$ .

**Table C.1:** Parameters used in Equation C.6 for the results in Figure 4.18.

	Trace 1	Trace 2
$G_0$	.3 m $\Omega^{-1}$	.3 m $\Omega^{-1}$
$U_0$	13 kV	13 kV
$f$	53.6 kHz	216 kHz
$G_t$	0.1 m $\Omega^{-1}$	0.1 m $\Omega^{-1}$



# Appendix D

## Anode temperature model evaluation

The model presented in Section 6.2.1 simulates the temperature of a copper anode, loaded by a vacuum arc. Since it simulates the melting of copper, it requires parameters for both solid and liquid copper. Table D.1 lists their values.

**Table D.1:** Copper parameters

	Value		Unit	Definition
	Liquid	Solid		
$\alpha$	$4.4 \cdot 10^{-5}$	$10.8 \cdot 10^{-5}$	m <sup>2</sup> /s	Diffusivity
$\lambda$	174	372	W/(Km)	Thermal conductivity
$\rho$	8000	8960	kg/m <sup>3</sup>	Mass density
$c_P$	494	384	J/(kgK)	Specific heat capacity
$A$	17650	17870	K	Parameter related to Equation (6.7)
$B$	13.39	10.63	—	—
$C$	−1.273	−0.236	1/ <sup>10</sup> log(K)	—
$D$	0	−0.16	1/K	—

Parameters used in this model that are state independent are given in Table D.2

**Table D.2:** State independent model parameters

	Value	Unit	Definition
$m_{Cu}$	$1.06 \cdot 10^{-25}$	kg	Copper atom mass
$H$	$2.05 \cdot 10^5$	J/kg	Latent heat of melting of copper
$N_A$	$6.02 \cdot 10^{23}$	mol <sup>−1</sup>	Avogadro’s constant
$k$	$1.38 \cdot 10^{-23}$	J/K	Boltzmann’s constant

The model has been solved with the aid of Matlab Simulink. It has been written as an S-function block, which makes it easy to use in different systems. An S-function is able to solve ordinary differential equations, but since Equation 6.1 is a partial differential equation, the spatial dimension is first discretised to obtain a system of ordinary differential equations. As a result, the model calculates the temperature at  $N$  points that are equally spaced. The linearity of the grid allows the solution of the system of  $N$  equation as

$$\frac{\partial T_0}{\partial t} = \alpha_S \frac{Q - L_{ev}}{\lambda_S \Delta x} + \alpha_S \frac{T_1 - T_0}{\Delta x^2} + v_{sur} \frac{T_1 - T_0}{\Delta x}, \quad (\text{D.1})$$

$$\begin{aligned} \frac{\partial T_k}{\partial t} &= \alpha_S \frac{T_{k+1} - 2T_k + T_{k-1}}{\Delta x^2} \\ &\quad + v_{sur} \frac{T_{k+1} - T_k}{\Delta x} \quad k = 2 \dots N-2, \end{aligned} \quad (\text{D.2})$$

$$\frac{\partial T_{N-1}}{\partial t} = \alpha_S \frac{T_A - 2T_{N-1} + T_{N-2}}{\Delta x^2} + v_{sur} \frac{T_A - T_{N-1}}{\Delta x}, \quad (\text{D.3})$$

where  $T_0$  is the anode surface temperature and  $T_A$  is the (fixed) ambient temperature at the far end of the anode. The last term in the left-hand side of Equations (D.1) and (D.2) accounts for the movement of the anode surface due to its vaporisation.  $v_{sur}$  is calculated with Equation (6.10).

As soon as  $T_0$  increases beyond the melting temperature, the melting depth is evaluated by solving Equation 6.8. At this point, the temperature is fixed, which makes it possible to divide the system of equations into a solid and a liquid part. The liquid part has a heat source at one end (the anode surface) and the fixed melting temperature at the other end, whereas the solid part has the melting temperature at one end, and the ambient temperature at the other end.

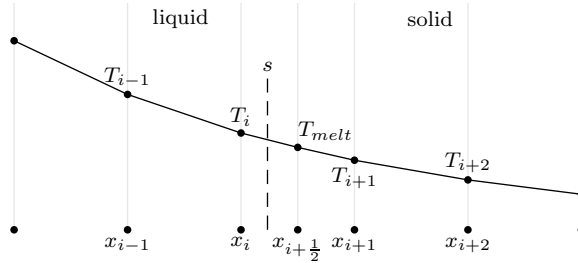


**Figure D.1:** Discretisation of the solid-liquid boundary location.  $s$  is the location of the boundary calculated with Equation (6.8), but  $x_{i+\frac{1}{2}}$  is used in the model evaluation.

Instead of re-defining the grid at each time-step to accurately model the progression of the liquid-solid boundary into the anode, the actual boundary is chosen

as the point right between two existing grid points (see Figure D.1). This makes it possible to replace Equation (D.3) by the following system of equations

$$\begin{aligned} \frac{\partial T_k}{\partial t} = & \alpha_L \frac{T_{k+1} - 2T_k + T_{k-1}}{\Delta x^2} \\ & + v_{sur} \frac{T_{k+1} - T_k}{\Delta x} \quad k = 2 \dots i-1, \end{aligned} \quad (D.4)$$

$$\frac{\partial T_i}{\partial t} = \alpha_L \frac{2T_{melt} - 3T_i + T_{i-1}}{\Delta x^2} + v_{sur} \frac{T_{melt} - T_i}{\frac{1}{2}\Delta x}, \quad (D.5)$$

$$\frac{\partial T_{i+1}}{\partial t} = \alpha_S \frac{T_{i+2} - 3T_{i+1} + 2T_{melt}}{\Delta x^2} + v_{sur} \frac{T_{i+2} - T_{i+1}}{\Delta x}, \quad (D.6)$$

$$\begin{aligned} \frac{\partial T_m}{\partial t} = & \alpha_S \frac{T_{m+1} - 2T_k + T_{m-1}}{\Delta x^2} \\ & + v_{sur} \frac{T_{m+1} - T_m}{\Delta x} \quad k = m+2 \dots N-2, \end{aligned} \quad (D.7)$$

for  $3 \leq i \leq N-3$ .  $\alpha_S$  and  $\lambda_S$  in Equation (D.1) are replaced with  $\alpha_L$  and  $\lambda_L$ . The model also takes into account the case that  $i = 2$ , which affects Equation (D.1), but when  $i$  becomes larger than  $N-3$ , the model has already lost its validity, and the solver returns an error.

The model has been solved with a `ode15s` solver, with a relative and absolute tolerance of  $10^{-3}$ . Since some of the parameters required for this cannot be measured with the available means in this research, this model is unable to exactly simulate the events of a measurement. Therefore, an approximation suffices, and one of the consequences is that the optimal spatial grid size  $\Delta x$  has been determined experimentally. The smaller  $\Delta x$ , the more accurate the result becomes, but at the cost of increased computation time. It has been experimentally determined that  $N = 200$  and  $\Delta x = 2.5\mu\text{m}$  give a reasonable compromise between accuracy and speed of the solution.

Figure D.2 shows the movement of the solid-liquid boundary, and the movement of the surface due to vaporisation of the simulation of trace 1 in Figure 6.2b. As a result of the discretisation of the solid-liquid boundary location, its trace shows shivery.

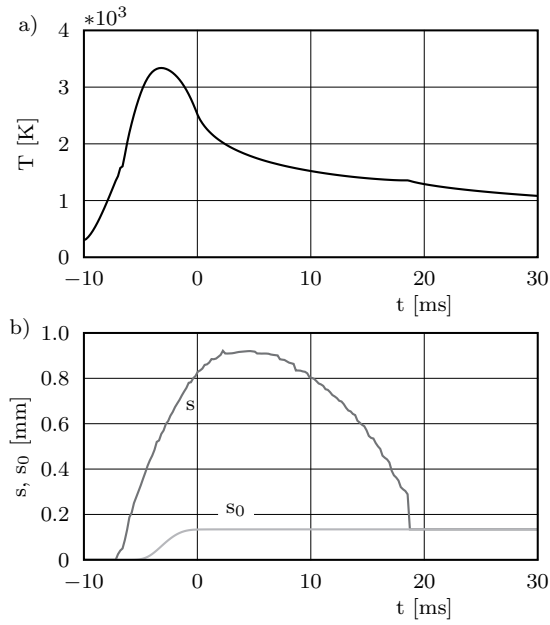


**Figure D.2:** a) Surface temperature, b) the solid-liquid boundary location ( $s$ ) and the location of the surface ( $s_0$ ) with respect to their starting position.

## Appendix E

# Implementation of the post-arc current model

Figure E.1 depicts the system block with which the models described in Chapter 6 have been implemented in Matlab's SimPowerSystems [83, 36]. The block has three connections, one for the open/close control of the breaker, and two electrical connections. The voltage  $u$  across the breaker and the control  $c$  are used as input for a predefined function  $G(u, c)$ , which calculates the current  $i$ . Its output is used to drive a controlled current source.

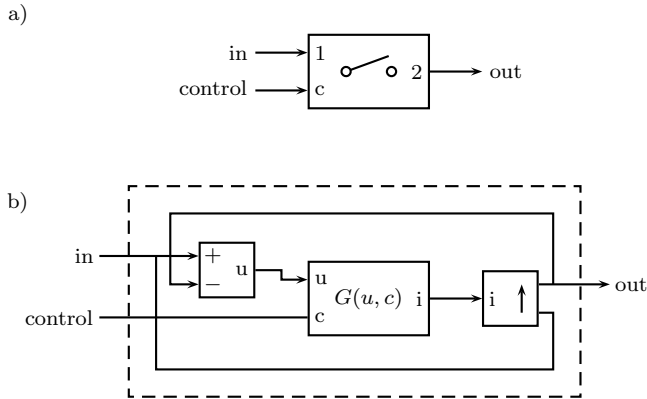


**Figure E.1:** a) SimPowerSystems block for circuit use, b) model implementation.

In closed operation, the breaker's electrical behaviour is simply given as  $G(u, c) = G_0 u$ , where  $G_0$  is a value for its conductance. During a simulation run, the model walks through a number of phases, each of which determines the breaker's con-

ductance differently. As soon as the model arrives at the sheath growth phase, its behaviour is defined by Equations (6.26), (6.28) and (6.29). This requires solving the sheath thickness and the current simultaneously, whereas they both depend on each other. It is a rather elaborate task to derive an explicit function for the conductance from these equations. The following describes how the breaker's electrical behaviour is solved in a different way.

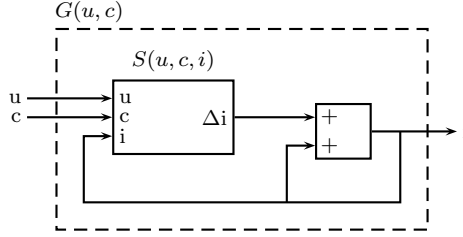


**Figure E.2:** The model implementation scheme for solving the sheath equations.

Instead of solving the conductance explicitly from these equations, which is quite difficult, the model makes use of Matlab's ability to solve an algebraic loop. Figure E.2 displays how the function  $G(u, c)$  is extended, and the idea behind this system is explained in [84]. The function block  $S(u, c, i)$  calculates the sheath thickness  $s$  by integrating the next expression:

$$\frac{ds}{dt} = \frac{i}{q_i n_i A} - v_i, \quad (\text{E.1})$$

which is Equation (6.26), written in a different way. Equation (E.1) is used in Equation (6.29) to obtain

$$U_0 = \frac{m_i}{2q_i} \left( \frac{i}{q_i n_i A} \right)^2, \quad (\text{E.2})$$

which relates  $U_0$  to one variable,  $i$ . This result is then used in Equation (6.28) that is now rewritten as

$$1 = \frac{4\varepsilon_0 U_0(i)}{9q_i n_i s^2} \left[ \left( 1 + \frac{u}{U_0(i)} \right)^{3/2} + 3 \frac{u}{U_0(i)} - 1 \right], \quad (\text{E.3})$$

$$0 = 1 - \frac{4\varepsilon_0 U_0(i)}{9q_i n_i s^2} \left[ \left( 1 + \frac{u}{U_0(i)} \right)^{3/2} + 3 \frac{u}{U_0(i)} - 1 \right], \quad (\text{E.4})$$

$$0 = F(u, i, s). \quad (\text{E.5})$$

In other words,  $u$ ,  $i$  and  $s$  have to be adjusted in such a way that  $F(u, i, s)$  remains zero. The model uses  $F(u, i, s)$  for  $\Delta i$  in Figure E.2, so that this is done automatically by Matlab.

In addition to solving the sheath equations, the model in Figure E.2 can also be used for the first example, when the breaker is closed, by writing  $\Delta i$  as

$$\Delta i = i - G_0 u. \quad (\text{E.6})$$

As explained before, the model progresses through a number of states during a simulation. Figure E.3 shows the simplified flowchart of the model, and it shows how  $\Delta i$  is calculated in each state. The time frames corresponding to the states are illustrated in Figure E.4, where the size and duration of the post-arc current have been exaggerated to improve the visibility of states 3 and 4.

The model also contains algorithms to handle a different polarity of the current and voltage, as well as an algorithm to ensure the accuracy of its results. It also allows the implementation of the anode temperature model of Section 6.2.1 and the model for the ion density  $n_i$ , as described in Section 6.2.2.

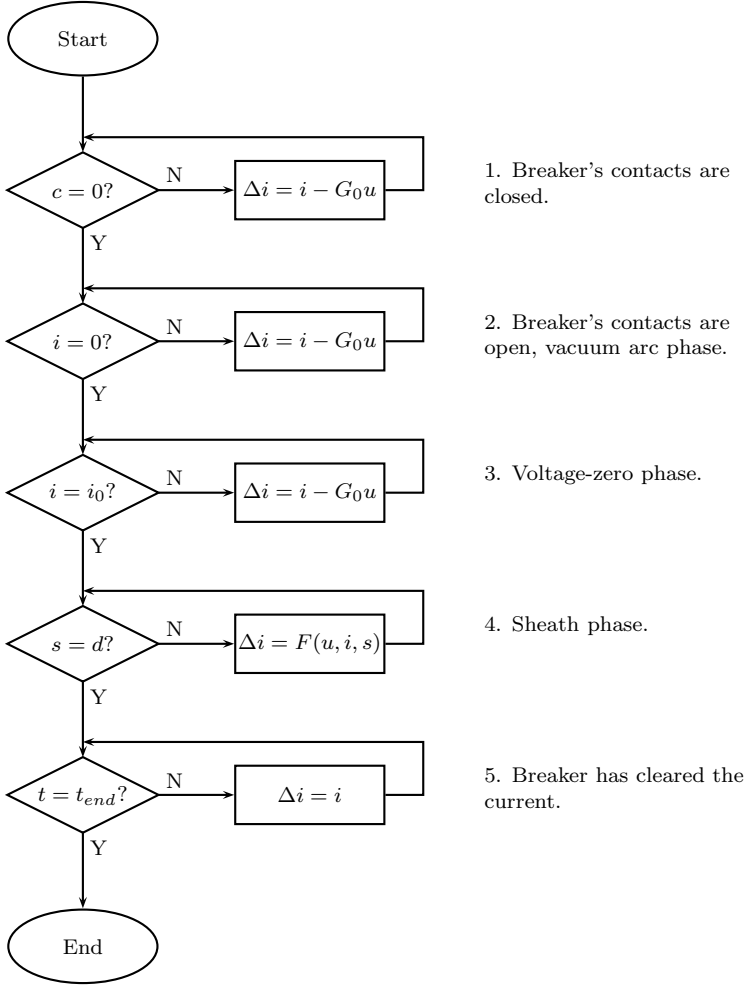


**Figure E.3:** The simplified flow-chart of the post-arc current model.



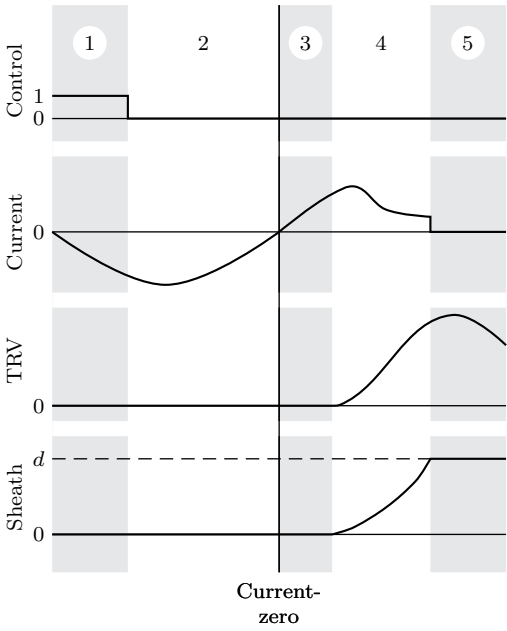


**Figure E.4:** Illustration of a simulation run. The numbers refer to the model's phases, as in Figure E.3.



# Appendix F

## Sheath capacitance model

The evaluation of the sheath capacitance is done according to the method used in [53], p.440. In the case that the ion energy at the plasma-sheath edge is small compared to the applied potential, the ion energy and flux conservation equations can be written as

$$\frac{1}{2}m_i v_i^2(x) = -q_i \phi(x), \quad (\text{F.1})$$

$$q_i n_i(x) v_i(x) = J_0, \quad (\text{F.2})$$

where  $v_i(x)$  is the ion velocity inside the sheath,  $\phi(x)$  is the potential (defined 0 at the plasma-sheath edge and  $-V$  at the cathode) and  $J_0$  is the constant ion current density. Solving Equations (F.1) and (F.2) for  $n_i(x)$  results in

$$n_i(x) = \frac{J_0}{q_i} \left( -\frac{2q_i \phi}{m_i} \right)^{-1/2}. \quad (\text{F.3})$$

Using this in Poission's equation ( $d^2\phi/dx^2 = -q_i n_i(x)/\epsilon_0$ ) gives

$$\frac{d^2\phi}{dx^2} = -\frac{J_0}{\epsilon_0} \left( -\frac{2q_i \phi}{m_i} \right)^{-1/2}, \quad (\text{F.4})$$

where  $\epsilon_0$  is the permittivity in vacuum. Multiplying Equation (F.4) with  $d\phi/dx$  and integrating from the plasma-sheath edge to the cathode gives

$$\frac{1}{2} \left( \frac{d\phi}{dx} \right)^2 = 2 \frac{J_0}{\epsilon_0} \left( \frac{2q_i}{m_i} \right)^{-1/2} (-\phi)^{1/2}, \quad (\text{F.5})$$

where it is assumed that  $d\phi/dx = -E = 0$  at the plasma-sheath boundary.

The sheath capacitance is written as

$$C_{sh} = \frac{dQ}{dV} = \epsilon_0 A_{eff} \frac{dE}{dV}, \quad (\text{F.6})$$

where  $Q$  is the charge on the cathode,  $V$  is the sheath voltage,  $A_{eff}$  is the effective cathode area, as defined in Equation (6.36), and  $E$  is the electric field at the cathode. Equation (F.5) is rewritten as

$$E = 2 \left( \frac{J_0}{\epsilon_0} \right)^{1/2} \left( \frac{m_i V}{2q_i} \right)^{1/4}, \quad (\text{F.7})$$

then differentiated with respect to  $V$  and used in Equation (F.6), to find the sheath capacitance as

$$C_{sh} = \frac{1}{2} (\epsilon_0 J_0)^{1/2} \left( \frac{m_i}{2q_i} \right)^{1/4} A_{eff} V^{-3/4}. \quad (\text{F.8})$$

The current density is equal throughout the sheath, and since ions are assumed to enter the sheath at Bohm velocity (Equation (6.30)),  $J_o$  from Equation (F.2), and Equation (F.8) can be rewritten as

$$C_{sh} = \frac{K}{V^{3/4}}, \quad (\text{F.9})$$

where

$$K \approx 0.42 (q_i n_i \epsilon_0)^{1/2} \left( \frac{kT_e}{q_i} \right)^{1/4} A_{eff}. \quad (\text{F.10})$$

# Bibliography

- [1] S. Yanabu, T. Tsutsumi, K. Yokokura, and E. Kaneko, “Recent technical developments in high-voltage and high-power vacuum circuit breakers,” in *IEEE Trans. Plasma Sci.*, vol. 17, no. 5, October 1989.
- [2] P. G. Slade, “Growth of vacuum interrupter application in distribution switchgear,” in *Trends in Distribution Switchgear*, no. 459. IEE, November 1998.
- [3] A. Greenwood, *Vacuum Switchgear*. London, UK: IEE, 1994.
- [4] J. M. Lafferty, Ed., *Vacuum Arcs Theory and Application*. John Wiley & Sons Inc., Schenectady, USA, 1980.
- [5] L. P. Harris, *Vacuum Arcs Theory and Application*. John Wiley & Sons Inc., Schenectady, USA, 1980, ch. Arc Cathode Phenomena, pp. 120–168.
- [6] B. Jüttner, “Cathode spots of electric arcs,” *J. Phys. D: Appl. Phys.*, vol. 34, pp. R103–R123, 2001.
- [7] E. Hantzsche, “Mysteries of the arc cathode spot: A retrospective glance,” *IEEE Trans. Plasma Sci.*, vol. 31, no. 5, pp. 799–808, October 2003.
- [8] G. A. Farrall, “Electrical breakdown in vacuum,” in *Vacuum Arcs, Theory and Application*, J. M. Lafferty, Ed. New York, USA: Wiley, 1980.
- [9] A. Anders, “The fractal nature of vacuum arc cathode spots,” *IEEE Trans. Plasma Sci.*, vol. 33, no. 5, pp. 1456–1464, October 2005.
- [10] G. Ecker, *Vacuum Arcs Theory and Application*. John Wiley & Sons Inc., Schenectady, USA, 1980, ch. Theoretical Aspects of the Vacuum Arc, pp. 228–320.
- [11] E. Hantzsche, “Theory of the expanding plasma of vacuum arcs,” *J. Phys. D: Appl. Phys.*, vol. 24, pp. 1339–1353, 1991.

- 
- [12] A. M. Chaly, A. A. Logatchev, and S. M. Shkol'nik, "Cathode processes in free burning and stabilized by axial magnetic field vacuum arcs," *IEEE Trans. Plasma Sci.*, vol. 27, no. 4, pp. 827–835, August 1999.
- [13] S. M. Shkol'nik, V. Afanas'ev, Y. A. Barinov, A. M. Chaly, A. A. Logatchev, S. I. Malakhovsky, I. N. Poluyanov, and K. K. Zabello, "Distribution of cathode current density and breaking capacity of medium voltage vacuum interrupters with axial magnetic field," *IEEE Trans. Plasma Sci.*, vol. 33, no. 5, pp. 1511–1518, October 2005.
- [14] G. Düning and M. Lindmayer, "Energy and density of ions in vacuum arcs between axial and radial magnetic field contacts," *IEEE Trans. Plasma Sci.*, vol. 29, no. 5, pp. 726–733, October 2001.
- [15] G. Lins, "Copper vapor density after current zero of vacuum arcs as a function of shield diameter and shield material," in *Proc. 19th ISDEIV*, Santa Fe, USA, 1990, pp. 242–245.
- [16] B. Fenski, "Verhalten von axialmagnetfeldkontakten in vakuumleistungsschaltern," Ph.D. dissertation, Technischen Universität Carolo-Wilhelmina zu Braunschweig, 1997.
- [17] M. Reece, "The vacuum switch, part 2. Extinction of an a.c. vacuum arc," *Proceedings IEE*, vol. 110, pp. 803–811, 1963.
- [18] S. Yanabu, M. Homma, E. Kaneko, and T. Tamagawa, "Post arc current of vacuum interrupters," *IEEE Trans. Power App. Syst.*, vol. PAS-104, no. 1, pp. 166–172, January 1985.
- [19] E. Düllni, E. Schade, and B. Gellert, "Dielectric recovery of vacuum arcs after strong anode spot activity," in *XIIIth ISDEIV*, Shores, Israel, 1986.
- [20] G. Lins, "Influence of electrode separation on ion density in the vacuum arc," *IEEE Trans. Plasma Sci.*, vol. 19, no. 5, pp. 718–724, October 1991.
- [21] K. Steinke, M. Lindmayer, and K.-D. Weltmann, "Post-arc currents of vacuum interrupters with axial magnetic field contacts under high current and voltage stress," in *XIXth ISDEIV*. Xi'an, China: IEEE, 2000.
- [22] R. Gebel, "Vapor shield potential in vacuum interrupters after clearing of short circuits," *IEEE Trans. Plasma Sci.*, vol. 17, no. 5, pp. 834–838, October 1989.
- [23] B. Fenski, M. Heimbach, M. Lindmayer, and W. Shang, "Characteristics of a vacuum switching contact based on bipolar axial magnetic field," *IEEE Trans. Plasma Sci.*, vol. 27, no. 4, pp. 949–953, August 1999.

- [24] E. Düllni and E. Schade, "Investigation of high-current interruption of vacuum circuit breakers," *IEEE Trans. Elect. Insulation*, vol. 4, no. 4, pp. 607–620, August 1993.
- [25] E. Schade and E. Düllni, "Recovery of breakdown strength of a vacuum interrupter after extinction of high currents," *IEEE Trans. Elect. Insulation*, vol. 9, no. 2, pp. 207–215, April 2002.
- [26] S. Anders, B. Jüttner, M. Lindmayer, C. Rusteberg, H. Pursch, and F. Unger-Weber, "Vacuum breakdown with microsecond delay time," *IEEE Trans. Elect. Insulation*, vol. 4, no. 4, pp. 461–467, August 1993.
- [27] S. Rowe, "Post arc dielectric breakdown in vacuum circuit breakers," in *High Voltage Engineering Symposium*, IEE, Ed., 1999, pp. 3.124.S22–3.127.S22.
- [28] G. Lins, I. Paulus, and F. Pohl, "Neutral copper vapor density and dielectric recovery after forced extinction of vacuum arcs," *IEEE Trans. Plasma Sci.*, vol. 17, no. 5, pp. 676–678, October 1989.
- [29] R. P. P. Smeets and Y. H. Fu, "Townsend-type breakdown as a criterion for high-frequency vacuum arc interruption at submillimeter gaps," *IEEE Trans. Plasma Sci.*, vol. 19, no. 5, pp. 767–771, October 1991.
- [30] V. V. Chulkov and A. A. Pertsev, "Investigation of the voltage of arc ignition between vacuum interrupter contacts after the arcing," in *XVIIth ISDEIV*, Berkeley, USA, 1996, pp. 21–23.
- [31] E. Schade, "Physics of high-current interruption of vacuum circuit breakers," *IEEE Trans. Plasma Sci.*, vol. 33, no. 5, pp. 1564–1575, October 2005.
- [32] K. Niayesh, "Reignitions in short vacuum gaps after interruption of high-frequency currents caused by ion bombardment," *IEEE Trans. Plasma Sci.*, vol. 29, no. 1, pp. 69–74, February 2001.
- [33] T. Fugel, "Practical solving of the emc-problems caused by switching high currents of vacuum breakers in a synthetic test circuit," in *Proc. 19th ISDEIV*, Xi'an, 2000, pp. 763–766.
- [34] A. van Deursen and J. van Waes, "Mitigation of ground loop effects in high-voltage measurements," *IEEE Trans. Instrum. Meas.*, vol. 51, pp. 480–486, 2002.
- [35] L. van der Sluis, *Transients in Power Systems*. New York, USA: Wiley, 2000.
- [36] P. Schavemaker, "Digital testing of high-voltage SF<sub>6</sub> circuit breakers," Ph.D. dissertation, Delft University of Technology, 2002.

- [37] IEC, *IEC-62271-100, High-Voltage Switchgear and Controlgear - Part 100: High-Voltage Alternating-Current Circuit-Breakers*. International Electrotechnical Commission, May 2003.
- [38] —, *IEC-62271-100, Amendment 2, High-Voltage Switchgear and Controlgear - Part 100: High-Voltage Alternating-Current Circuit-Breakers*. International Electrotechnical Commission, July 2006.
- [39] W. A. van der Linden and L. van der Sluis, "A new artificial line for testing high-voltage circuit breakers," *IEEE Trans. Power App. Syst.*, vol. PAS-102, no. 4, pp. 797–803, April 1983.
- [40] R. P. P. Smeets and W. A. van der Linden, "Current-zero measurements of vacuum circuit breakers interrupting short-line faults," *IEEE Trans. Plasma Sci.*, vol. 31, no. 5, pp. 852–858, October 2003.
- [41] T. Browne, *Circuit Interruption*. Marcel Dekker, Inc., 1984.
- [42] M. Binnendijk, W. Merck, R. Smeets, K. Watanabe, and E. Kaneko, "High-current interruption in vacuum circuit breakers," *IEEE Trans. Plasma Sci.*, vol. 4, pp. 836–840, 1997.
- [43] M. van Schendel, "Current zero phenomena in vacuum circuit breakers," Master's thesis, Eindhoven University of Technology, 2004.
- [44] A. T. Roguski, "Experimental investigation of the dielectric recovery strength between the separating contacts of vacuum circuit breakers," *IEEE Trans. Power Delivery*, vol. 4, no. 2, pp. 1063–1069, April 1989.
- [45] G. C. Damstra and V. Kertész, "Development and application of a 10 mhz digital system for current-zero measurements," *IEE Proc.-Sci. Meas. Technol.*, vol. 142, no. 2, pp. 125–132, March 1995.
- [46] R. P. P. Smeets, A. H. Eenink, and V. Kertész, "A new high-resolution high-frequency current-zero measuring system," in *Proc. ERA Conf. Measurements and Calibration in High Voltage Testing*, London, U.K., 1998, pp. 1–12.
- [47] D. Young and R. Gregory, *A Survey of Numerical Mathematics*. Reading, USA: Addison-Wesley, 1972, vol. 1.
- [48] J. N. Sharma, *Numerical Methods for Engineers and Scientists*. Alpha Science International Ltd., Pangbourne, UK, 2004.
- [49] E. F. J. Huber, K. D. Weltmann, and K. Froehlich, "Influence of interrupted current amplitude on the post-arc current and gap recovery after current zero - experiment and simulation," *IEEE Trans. Plasma Sci.*, vol. 27, no. 4, pp. 930–937, August 1999.



- 
- [50] S. E. Childs, A. N. Greenwood, and J. S. Sullivan, "Events associated with zero current passage during the rapid commutation of a vacuum arc," in *Xth ISDEIV*. Columbia, Missouri, USA: IEEE, 1982.
- [51] J. Kaumanns, "Measurements and modelling in the current zero region of vacuum circuit breakers for high current interruption," *IEEE Trans. Plasma Sci.*, vol. 25, no. 4, pp. 632–636, August 1997.
- [52] Y. P. Raizer, *Gas Discharge Physics*, J. E. Allen, Ed. Springer-Verlag, Berlin Heidelberg, 1991.
- [53] M. A. Lieberman and A. J. Lichtenberg, *Principles of Plasma Discharges and Materials Processing*. Wiley, 2005.
- [54] R. L. Boxman, D. M. Sanders, and P. J. Martin, *Handbook of vacuum arc science and technology; fundamentals and applications*. Park Ridge : Noyes, 1995.
- [55] S. W. Rowe and H. Schellekens, "Post arc breakdown in vacuum circuit breakers," in *XXth ISDEIV*. Tours, France: IEEE, 2002, pp. 9–12.
- [56] E. Düllni and E. Schade, "Recovery behavior of vacuum circuit-breakers at the current interruption limit," in *Proc. 14th ISDEIV*. Santa Fe, USA: IEEE, 1990, pp. 517–521.
- [57] L. Frost and J. T.E. browne, "Calculation of arc-circuit interaction," in *Circuit interruption*, J. T.E. Browne, Ed. New York and Basel: Marcel Dekker, Inc., 1984, ch. 6, pp. 187–240.
- [58] L. van der Sluis, W. Rutgers, and C. Koreman, "A physical arc model for the simulation of current zero behavior of high-voltage circuit breakers," *IEEE Trans. Power Delivery*, vol. 7, no. 2, pp. 1016–1022, April 1992.
- [59] R. Smeets and V. Kertész, "Evaluation of high-voltage circuit breaker performance with a validated arc model," *IEE Proc.-Gener. Transm. Distrib.*, vol. 147, no. 2, pp. 121–125, March 2000.
- [60] B. Gellert and W. Egli, "Melting of copper by an intense and pulsed heat source," *J. Phys. D: Appl. Phys.*, vol. 21, pp. 1721–1726, 1988.
- [61] S. Dushman, *Scientific Foundations of Vacuum Technique*. New York, USA: Wiley, 1949.
- [62] N. Ide, R. Sakuma, E. Kaneko, and S. Yanabu, "The electrode surface state after current interruption in vacuum circuit breakers," in *XXIth ISDEIV*. Matsue, Japan: IEEE, 2006, pp. 396–399.

- [63] R. Gilles, K.-D. Weltmann, E. Schade, and M. Claessens, "Numerical simulation of the residual charge of vacuum interrupters," *IEEE Trans. Plasma Sci.*, vol. 29, no. 5, pp. 754–758, October 2001.
- [64] C. D. Child, "Discharge from hot CaO," *Phys. Rev. (Series I)*, vol. 32, no. 5, pp. 492–511, May 1911.
- [65] J. G. Andrews and R. H. Varey, "Sheath growth in a low pressure plasma," *the Physics of Fluids*, vol. 14, no. 2, pp. 339–343, February 1971.
- [66] G. A. Farrall, "Current zero phenomena," in *Vacuum Arcs, Theory and Application*, J. M. Lafferty, Ed. New York, USA: Wiley, 1980.
- [67] I. Brown and X. Godechot, "Vacuum arc ion charge-state distributions," *IEEE Trans. Plasma Sci.*, vol. 19, no. 5, pp. 713–717, October 1991.
- [68] G. Düning and M. Lindmayer, "Plasma density decay of vacuum discharges after current zero," in *XVIIIth ISDEIV*. Eindhoven, the Netherlands: IEEE, 1998.
- [69] A. Klajn, "Experimental analysis of ion parameters during the forced vacuum arc interruption," in *Proc. 20th ISDEIV*, Tours, France, 2002, pp. 415–418.
- [70] A. von Engel, *Ionized Gases*. London, UK: Oxford University Press, 1965, p. 195.
- [71] M. Lindmayer and E.-D. Wilkening, "Breakdown of short vacuum gaps after current zero of high frequency arcs," in *XIVth ISDEIV*, Santa Fe, USA, 1990.
- [72] M. T. Glinkowski and P. Stoving, "Numerical modeling of vacuum arc interruption based on the simplified plasma equations," *IEEE Trans. Magn.*, vol. 31, no. 3, pp. 1924–1927, May 1995.
- [73] J. Kaumanns, "Measurement and modelling in the current zero region of vacuum circuit breakers for high current interruption," in *XVIIth ISDEIV*. Berkeley, USA: IEEE, 1996.
- [74] M. Galonska, R. Hollinger, I. A. Krinberg, and P. Spaedtke, "Influence of an axial magnetic field on the electron temperature in a vacuum arc plasma," *IEEE Trans. Plasma Sci.*, vol. 33, no. 5, pp. 1542–1547, 2005.
- [75] S. Nam, B. Lee, S. Park, S. Kim, and Y. Han, "Spectroscopic measurement of high current vacuum arc plasma in triggered vacuum switch," in *PPPS-2001*, vol. 2, June 2001, pp. 1790–1793.
- [76] K. Arai, S. Takahashi, O. Morimiya, and Y. Niwa, "Probe measurements of residual plasma of a magnetically confined high-current vacuum arc," *IEEE Trans. Plasma Sci.*, vol. 31, pp. 929–933, 2003.

- [77] A. Klajn, “Langmuir probes in switching vacuum arc measurements,” *IEEE Trans. Plasma Sci.*, vol. 33, no. 5, pp. 1611–1617, October 2005.
- [78] H. Pursch and B. Jüttner, “The behaviour of the ion current at the extinction of high current vacuum arcs,” in *XVIIth ISDEIV*. Berkeley, USA: IEEE, 1996.
- [79] M. Glinkowski and A. Greenwood, “Computer simulation of post-arc plasma behavior at short contact separation in vacuum,” *IEEE Trans. Plasma Sci.*, vol. 17, no. 1, pp. 45–50, February 1989.
- [80] S. Baboolal, “Boundary conditions and numerical fluid modelling of time-evolutionary plasma sheaths,” *J. Phys. D: Appl. Phys.*, vol. 35, pp. 658–664, 2002.
- [81] S. W. Rowe and J. P. Boeuf, “Simulation of plasma sheath dynamics in vacuum circuit breakers,” in *Proc. 20th ISDEIV*, 2002, pp. 162–165.
- [82] S.-B. Wang and A. E. Wendt, “Sheath thickness evaluation for collisionless or weakly collisional bounded plasmas,” *IEEE Trans. Plasma Sci.*, vol. 27, no. 5, pp. 1358–1365, October 1999.
- [83] *SimPowerSystems User’s Guide*, The Mathworks, Inc., 2004.
- [84] L. F. Shampine, M. W. Reichelt, and J. A. Kierzenka, “Solving index-i daes in matlab and simulink,” *SIAM Review*, vol. 41, no. 3, pp. 538–552, 1999.



# Acknowledgements

In the course of four years I have met many people who all contributed to my thesis to some extent. Completing a thesis is an accomplishment that simply cannot be done alone. I am much indebted to all of them. Some of them played a crucial part in this entire work, and some of them just went out of their common way to help me. These are the people I would like to acknowledge; their contribution will be remembered.

First of all, I would like to thank Lou van der Sluis for accepting me as a Ph.D. student, for being an excellent advisor, and for being a magnificent travelling partner. Another agreeable travelling companion was René Smeets, to whom I owe my finest achievements by being my severest critic. His apparent disagreement with almost everything I brought up was the way to get the very best out of me. For this, and for the time and dedication that he has spent on my work, I am infinitely grateful. Many thanks also to Marjan Popov, who has always been available to support my work as a daily supervisor. Martin Verweij contributed not only with his knowledge on simulation, but also deserves credit for inspiring me to start my academic career. The colleagues in my department I owe the pleasure which a coffee break generally affords.

This work has been funded by the Technology Foundation (STW), which supports utilisation by involving the industry with the university research. As such, the companies KEMA, Eaton-Holec, Tavrida Electric and Siemens this research possible. I would like to thank them all for supporting this work with test objects, laboratory time and know-how. In particular I mention Martin Leusenkamp for his active support during this work in the time that he was still working in the Netherlands. I sincerely regret that I haven't gotten the opportunity to see how he continued his work in China.

With much appreciation I remember the valuable collaboration that I have had with the Ukrainian company Tavrida Electric. From a distance, Irina Poluyanova has been actively participating in my work, and I treasure the enthusiasm with which she did that. Apart from our professional contact, she successfully demonstrated the truth about the beauties of the Crimean Peninsula to me. I still intend to return to Sevastopol one day.

More to the background, but of great value nonetheless, was the contribution from Alexey Chaly, founder and general manager of Tavrida Electric. As a result of our discussion during my stay at Sevastopol, he triggered the idea for my Chatterton Award winning explanation of the voltage-zero event (Sections 4.4 and 6.3.2).

In Budapest I was most hospitably received by Viktor Kertész. Not only was I allowed to use his software, but he was also generous with ideas and we had many interesting discussions.

At the start of this project, Thijs van Schendel was my reliable supplier of measurement data and gave me the opportunity to get to know the test set-up and how to handle the equipment. For him, it resulted in an excellent graduation, and for me, a meaningful contribution to my work. When Thijs left, realising all the practical work would have been impossible without the help of Rob Kerkenaar, who continued to support me even after his retirement, without requiring any favour in return. People that know how to run a laboratory are hard to find, but when Rob was not available, René van Hoppe or Arie van Staalduinen were always around to help me with my potentially dangerous work. I am much obliged to both of them.

My wife Josien has been of great value and support during the difficult times of my work. Not only as a friend and partner, but also because her linguistic skills, and her extensive knowledge of the English language have been invaluable to the readability of this thesis. As a result, she now probably knows a great deal more about vacuum circuit breakers than most electrical engineers.

I would also like to express my gratitude to the Permanent International Scientific Committee of the International Symposium on Discharges and Electrical Insulation in Vacuum for awarding my work at the symposium in Matsue, Japan. Many thanks for the ABB company for making the Chatterton Young Investigators Award possible.

# Curriculum Vitae

Ezra van Lanen was born in Eindhoven, the Netherlands, on 6 February 1975. He started his electrical engineering career in Alkmaar, where he attended secondary school 'Jan Arentsz College'; intermediate technical school 'Alkwaard College'; and technical college 'Hogeschool Alkmaar'. His interest in the theoretical foundation of electrical engineering thus triggered, he then enrolled at the Delft University of Technology, Faculty of Electrical Engineering in 1995. Here, he graduated in 2002 on the subject of propagating elastic waves in a steel plate. During these years, Ezra participated in a number of extracurricular activities, such as board member of a student organisation, and as a musician in a band. In 2003, he started his Ph.D. research on an STW (the Dutch Technology Foundation) project concerning the testing of vacuum circuit breakers. This research was twofold with a theoretical part at the Electrical Power Systems Laboratory at the Delft University of Technology and a practical part at the High Currents Laboratory at the Eindhoven University of Technology. This thesis describes its results. During this project, Ezra wrote two papers for the IEEE Transactions of Plasma Science, and five conference papers. In 2006, his contribution to the understanding of the current interruption process in vacuum was rewarded with the Chatterton Young Investigators Award, which is sponsored by ABB, at the IEEE ISDEIV conference in Matsue, Japan. In June 2007, he joined the Faculty of Science and Technology at the Twente University to work on superconductors.